Plasmonically Enhanced Infrared Radiation Detector

Khan, Mohammad Wahiduzzaman

2023

UNIVERSITY OF CALIFORNIA,
IRVINE

Plasmonically Enhanced Infrared Radiation Detector

DISSERTATION

submitted in partial satisfaction of the requirements
for the degree of

DOCTOR OF PHILOSOPHY

in Electrical and Computer Engineering

by

Mohammad Wahiduzzaman Khan

Dissertation Committee:
Professor Ozdal Boyraz, Chair
Professor Hamidreza Aghasi
Professor Rahim Esfandyar-pour

2023

DEDICATION

“In the name of Allah, The Most Gracious and The Most Merciful”
“Praise be to Allah, the Lord of the Universe”
Dedicated to my wife, Rufaida Luthfun Anagh, for her never-ending support and motivation, and to my parents, for being outstanding role models and for their invaluable support and encouragement throughout my academic pursuits.

TABLE OF CONTENTS

LIST OF FIGURES

LIST OF TABLES

ACKNOWLEDGMENTS

I express my gratitude to my PhD advisor, Professor Ozdal Boyraz, for his unwavering support and guidance during my PhD journey. I appreciate his flexibility and patience as I navigated through research. I am thankful for his insightful ideas and invaluable perspectives that greatly contributed to my progress.

My heartfelt thanks to my highly supportive colleagues at Advanced Photonic Devices and Systems Lab (APDSL, UCI) - Dr. Qiancheng Zhao, Dr. Rasul Torun Dr. Parinaz Sadri-Moshkenani, Dr. Imam Uz Zaman, Dr. Mustafa Mert Bayer, and Md Shafiqul Islam, for creating a positive and professional work environment, for mentoring me.

I would like to thank National Science Foundation (NSF), Defense Threat Reduction Agency (DTRA), and UCI Samueli School or Engineering for funding assistance. I also appreciate the support received from the the Center for Integrated Nanotechnologies (CINT), Los Alamos National Lab (LANL).

Part of this dissertation is a reprint of the materials as they appear in — Journal of the Optical Society of America B (OSA JOSAB 2020, vol. 37(3)), IEEE Journal of Quantum Electronics (IEEE JQE 2021, vol. 57(4)), and International Journal of Thermophysics (Springer Nature IJT 2023, vol. 44(1)).

VITA

Mohammad Wahiduzzaman Khan

EDUCATION

Doctor of Philosophy in Electrical and Computer Engineering **2023**
University of California - Irvine *Irvine, CA*

Master of Science in Electrical and Computer Engineering **2021**
University of California - Irvine *Irvine, CA*

Bachelor of Science in Electrical & Electronic Engineering **2014**
Bangladesh University of Engineering & Technology *Dhaka, Bangladesh*

RESEARCH EXPERIENCE

Graduate Research Assistant **2016-2023**
Advanced Photonic Devices and Systems Lab

University of California - Irvine *Irvine, CA*

TEACHING EXPERIENCE

Teaching Assistant **2018–2023**
University of California - Irvine *Irvine, CA*

INTERNSHIP EXPERIENCE

Hardware Engineer Intern **Jun 2021 - Sep 2021**
Waymo LLC *Mountain View, CA*

Engineering Intern **Jun 2020 - Dec 2020**
Qualcomm *San Diego, CA*

Network Hardware Engineer, PhD Intern **Jun 2019 - Sep 2019**
Facebook *Menlo Park, CA*

HW and Algorithm Engineering Intern **Jun 2018 - Sep 2018**
Masimo *Irvine, CA*

HW and Algorithm Engineering Intern **Jul 2017 - Sep 2017**
Masimo *Irvine, CA*

REFEREED JOURNAL PUBLICATIONS

M. W. Khan, and O. Boyraz, "Polarization-Sensitive Terahertz Bolometer Using Plasmonically-Heated Vanadium-Dioxide Beam," International Journal of Thermophysics, 44(0), pp.1-17, January 2023.

P. Sadri-Moshkenani, **M. W. Khan**, M. S. Islam, E. A. Montoya, I. Krivorotov, and O. Boyraz, "Optoelectronic Readout of STT-RAM Based on Plasmon Drag Effect," IEEE Journal of Quantum Electronics, vol. 57, pp. 1-7, September 2021.

M. W. Khan, J. M. Sullivan, J. Lee, and O. Boyraz, "High sensitivity long-wave infrared detector design based on integrated plasmonic absorber and VO_2 nanobeam," IEEE J. Quantum Electron. 57(4), 1–11, May 2021.

P. Sadri-Moshkenani, **M. W. Khan**, M. S. Islam, E. A. Montoya, I. Krivorotov, N. Bagherzadeh, and O. Boyraz, "Effect of magnesium oxide adhesion layer on resonance behavior of plasmonic nanostructures," Applied Physics Letters, vol. 116, pp. 241601, June 2020.

M. W. Khan, Q. Zhao, P. Sadri-Moshkenani, M. S. Islam, and O. Boyraz, "Graphene-incorporated plasmo-thermomechanical infrared radiation detection," JOSA B, vol. 37, pp. 774-783, March 2020.

P. Sadri-Moshkenani, **M. W. Khan**, M. S. Islam, I. Krivorotov, M. Nilsson, N. Bagherzadeh, and O. Boyraz, "Array of symmetric nanohole dimers with high sensitivity for detection of changes in an STT-RAM ultrathin dielectric layer," JOSA B, vol. 36, pp. 3090-3097, November 2019.

Q. Zhao , **M. W. Khan**, S. Farzinazar, J. Lee, and O. Boyraz, "Plasmo-thermomechanical radiation detector with on-chip optical readout," Optics express, 26(23), pp.29638-29650, November 2018.

Q. Zhao, P. Sadri-Moshkenani, **M. W. Khan**, R. Torun, and O. Boyraz, "On-chip bimetallic plasmo-thermomechanical detectors for mid-infrared radiation," IEEE Photonics Technology Letters, vol. 29, pp. 1459-1462, September 2017.

REFEREED CONFERENCE PUBLICATIONS

M. W. Khan, and O. Boyraz, "Polarization Sensitive Terahertz Bolometer," CLEO: Science and Innovations (pp. JTh3A-43). Optica Publishing Group, May 2022.

M. S. Islam, I. U. Zaman, P. Sadri-Moshkenani, **M. W. Khan**, and O. Boyraz, "Metalens wide- angle receiver for free space optical communications," SPIE Optics and Photonics Conference, San Diego, CA, August 2021.

P. Sadri-Moshkenani, **M. W. Khan**, M. S. Islam, D. Shi, E. A. Montoya, I. Krivorotov, N. Bagherzadeh, and O. Boyraz. "Optoelectronic Readout of STT-RAM Memory Cells Using

Plasmon Drag Effect," OSA Conference on Lasers and Electro-Optics (CLEO), San Jose, CA, May 2021.

M. W. Khan, P. Sadri-Moshkenani, M. S. Islam, and O. Boyraz, "Active modulation of optical leaky wave antenna by vanadium dioxide corrugations," SPIE Optics and Photonics Conference, Online, September 2020.

M. W. Khan, P. Sadri-Moshkenani, M. S. Islam, O. Boyraz, J. Sullivan, Z. Yu, and J. Lee, "Selective and efficient infrared detection by plasmonically heated vanadium-dioxide nanowire," SPIE Optics and Photonics Conference, Online, September 2020.

P. Sadri-Moshkenani, **M. W. Khan**, M. M. Bayer, M. S. Islam, E. A. Montoya, I. Krivorotov, M. Nilsson, N. Bagherzadeh, and O. Boyraz, "Effect of Tantalum and MgO adhesion layers on plasmonic nanostructures," SPIE Optics and Photonics Conference, San Diego, CA, September 2019.

M. W. Khan, P. Sadri-Moshkenani, M. S. Islam, and O. Boyraz, "Graphene-coated suspended metallic nanostructures for fast and sensitive optomechanical infrared detection," OSA Conference on Lasers and Electro-Optics (CLEO), San Jose, CA, May 2019.

P. Sadri-Moshkenani, **M. W. Khan**, M. S. Islam, I. Krivorotov, M. Nilsson, N. Bagherzadeh, and O. Boyraz, "Array of symmetric nanohole dimers for STT-RAM ultrathin layer sensing," OSA Conference on Lasers and Electro-Optics (CLEO), San Jose, CA, May 2019.

Q. Zhao, **M. W. Khan**, P. Sadri-Moshkenani, R. Regan, F. Capolino, and O. Boyraz, "Demonstration of a Plasmo-Thermomechanical Radiation Detector with Si3N4 Waveguide Optical Readout Circuit," OSA Conference on Lasers and Electro-Optics (CLEO), San Jose, CA, May 2018.

Q. Zhao, **M. W. Khan**, P. Sadri-Moshkenani, R. Torun, I. U. Zaman, and O. Boyraz, "Plasmo- thermomechanical suspended nanowire array detectors for mid-infrared spectrum," SPIE Optics and Photonics Conference, San Diego, CA, August 2017.

P. Sadri-Moshkenani, **M. W. Khan**, Q. Zhao, I. Krivorotov, M. Nilsson, N. Bagherzadeh, and O. Boyraz, "Plasmonic detection of possible defects in multilayer nanohole array consisting of essential materials in simplified STT-RAM cell," SPIE Optics and Photonics Conference, San Diego, CA, August 2017.

Q. Zhao, P. Sadri-Moshkenani, **M. W. Khan**, R. Torun, I. U. Zaman, and O. Boyraz, "Infrared detection using plasmonically enhanced thermomechanically actuated nanowire arrays," OSA Conference on Lasers and Electro-Optics (CLEO), San Jose, CA, May 2017.

P. Sadri-Moshkenani, **M. W. Khan**, Q. Zhao, I. Krivorotov, M. Nilsson, N. Bagherzadeh, and O. Boyraz, "Plasmonic detection of possible defects in multilayer nanohole array consisting of essential materials in simplified STT-RAM cell," Plasmonics: Design, Materials, Fabrication, Characterization, and Applications XV (Vol. 10346, pp. 204-209). SPIE, August 2017.

PATENT

M.W. Khan, O. Boyraz, J. M. Sullivan, J. Lee, and Z. Yu, “Plasmonically enhanced, ultra-sensitive bolometric mid-infrared detector,” U.S. Patent 11,598,672, May 2023.

ABSTRACT OF THE DISSERTATION

Plasmonically Enhanced Infrared Radiation Detector

By

Mohammad Wahiduzzaman Khan

Doctor of Philosophy in Electrical and Computer Engineering

University of California, Irvine, 2023

Professor Ozdal Boyraz, Chair

Ultra-low temperature photon detectors have been able to achieve high detection sensitivity but they remain a high-maintenance and expensive option. Thermal detectors, on the other hand, can be operated at room-temperature and can provide a more affordable and portable option, albeit with lower performance compared to its counterpart. As such, there remains a need for uncooled detectors with higher sensitivity, higher pixel density, and higher bandwidth for critical applications, such as on-chip optical readout of incident radiation, high-resolution medical imaging, autonomous driving at low-light conditions, and military applications. This dissertation presents a study on the design, fabrication, and characterization of radiation detectors with high sensitivity, specifically plasmo-thermomechanical and microbolometric types. Here, plasmonically enhanced thermo-mechanical and thermo-electrical properties of materials and device geometries are intelligently exploited to achieve uncooled electromagnetic radiation detectors with improved sensitivity and bandwidth of operation.

Many novel applications in plasmonics and integrated optics have emerged from the advances in micro and nanofabrication techniques. In particular, plasmonic structures have demonstrated their ability to focus and control light at a micro- and nano-scales, which leads to intense light-matter interactions - key to high sensitivity at reduced area. In addition to their

electromagnetic properties, micro and nanoscale plasmonic structures may open up new opportunities for novel applications based on their thermal and mechanical properties. Along with patterned metallic nanostructures, 2D materials like graphene possess extra-ordinary thermal and plasmonic properties that are key to the enablement of novel sensing devices.

The first work described in this thesis demonstrates a true full integration of plasmo thermo mechanics and integrated optical waveguides that turn efficient optical absorption into light modulation in waveguides through the use of plasmonic fishbone nanowires. By using plasmonic absorbers, specific band of radiation energy from free space is transformed into heat, causing the nanowires suspended above a waveguide to bend. The radiation is finally detected all-optically as a fluctuation of the waveguide insertion loss. The efficiency and bandwidth of such devices are further shown to be augmented by the incorporation of a graphene layer on top of the metallic nanowires due to graphene's extraordinary plasmonic and heat-spreading properties.

The second part of the dissertation presents a microbolometric detector that incorporates a vanadium dioxide (VO_2) nanobeam integrated with plasmonic absorbers to thermo-electrically detect the incident electromagnetic radiation. VO_2 is a phase-transition material (PTM) that exhibits a unique property known as semiconductor to metal transition, whereby it can switch between semiconducting and metallic states at a specific temperature called the transition temperature. As such, this transition metal oxide is highly sensitive to optical and thermal signals, making their perception precise and efficient. In particular, its sharp temperature-dependent resistivity makes it a suitable material of choice for microbolometers. The incorporation of plasmonic absorber, on the other hand, provides design flexibility and tunability to detect narrowband, broadband, or even multiband electromagnetic radiation. Presented in this study is an example design of an infrared detector that is designed to sense thermal information from a human body emitting infrared (IR) radiation peaking near 10 μm wavelength. Unlike other bolometric detectors, the proposed detector incorporates VO_2

nanobeam (instead of a VO_2 film) and is designed to operate near the VO_2 phase transition temperature to achieve enhanced responsivity.

Scaling the device geometries of plasmonic absorbers has the potential to transition the example design of bolometer to operate at far infrared spectrum or THz frequency. However, simple scaling is not sufficient to achieve such operation as the electromagnetic properties of constituent materials as well as the thermodynamic and mechanical properties of bolometers are subject to substantial changes with changes in frequency and size. To demonstrate design methodology and its scalability, an uncooled high-sensitivity bolometric terahertz detector operating near 1.7 THz is studied. The design additionally facilitates simultaneous sensing of intensity and polarization of incident radiation by utilizing polarization-dependent plasmonic field enhancement. Estimated responsivity is over 5 kV/W, noise equivalent power (NEP) is below 12 pW, and normalized detectivity over 10^8 $cm.Hz^{1/2}.W^{-1}$ which are competitive to state-of-the-art THz bolometer designs.

The final section of this work presents the fabrication steps for a proof-of-concept device that incorporates plasmonic absorbers and VO_2 beams. This includes details on the deposition techniques and lithographic patterning used for the VO_2 beams and plasmonic absorbers. Additionally, the work includes the results of x-ray diffraction test and temperature-dependent electronic probing of deposited VO_2 films and beams, and the IR spectroscopy of fabricated plasmonic absorbers demonstrating the practicality of the proposed design concept for high-resolution bolometric radiation detectors.

Chapter 1

Introduction

1.1 Background

In the last few decades, infrared (IR) detection has found extensive use in various applications such as night vision, missile tracking, material inspection, medical diagnostics, and more. To improve the performance of IR detection for these applications, researchers have focused on enhancing the detection capability, sensitivity, selectivity, and efficiency of IR detectors. The advancement in IR detectors has been largely due to the development of precise fabrication methods and growth techniques by the integrated circuit (IC) industry. However, contemporary IR photodetectors are bulky, expensive, and require low temperature to operate. An alternative method, called the photothermal way of IR detection, is compact, cost-effective, and can operate at room temperature. The concept of radiation detection is presented in Fig. 1.1.

The thermal IR detector relies on converting electromagnetic energy into temperature or thermal gradient, which can be measured by the changes in conductivity or mechanical deflection. At the nanoscale, nanoengineered structures play a vital role in enhancing the sen-

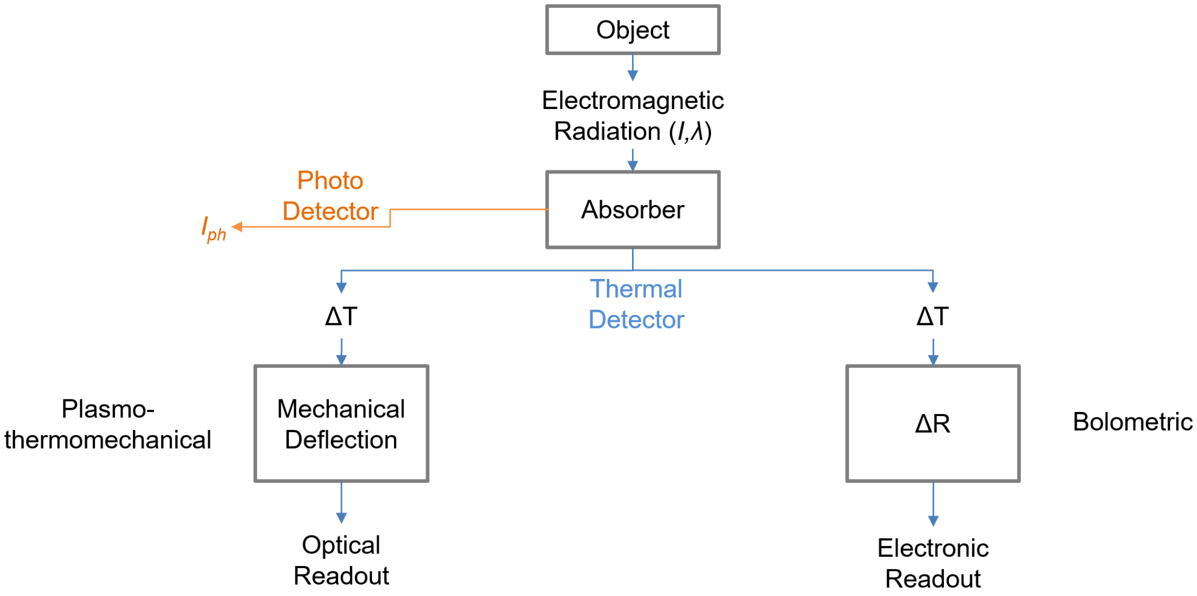

Figure 1.1: Conceptual block diagram of an electromagnetic radiation detector. Any object with finite temperature emits radiation depending on its temperature and emissivity. I and λ are the intensity and the wavelength of radiation emitted from object. I_{ph} is the photocurrent readout signal generated upon radiation incidence on photodetectors. Thermal detectors, on the other hand, reads out the temperature variation, ΔT in the detector upon radiation incidence. ΔR is the change in resistance due to temperature variation.

sitivity and coupling between different forms of energy. Plasmonic absorbers are particularly useful in selectively absorbing a specific regime of the radiation spectrum. Nano-engineered spectrally selective optical antennas in suspended metallic beams can efficiently absorb free-space radiation. The absorbed energy creates a thermal gradient, which causes the beams to deflect based on their material properties. By optically probing the mechanical deflection using a waveguide, the amount of absorbed radiation can be measured.

In this study, the authors propose coating metallic nanostructures with graphene to improve absorption and speed of operation. The incorporation of graphene in the nanostructures enhances sensitivity and bandwidth while reducing noise. The authors analyze the absorptance profile with respect to the size and shape of nanostructures and include the effect of the adhesion layer in their calculations. They also discuss the evanescent interaction and its effect on the waveguided probe signal and compare the time constants of the beam's mechanical deflection. The results indicate that integrating graphene in the nanostructure can significantly improve the performance of IR detectors.

The radiation induced thermal energy can also be read out electronically. Such detectors are called bolometers. Bolometers offer a cost-efficient solution for IR detection at room temperature. However, their performance lacks significantly compared to photodetectors which usually requires cryogenic cooling. This dissertation presents high-resolution bolometers operating at long wave infrared (LWIR) wavelength and terahertz (THz) frequencies. The high-resolution and increased sensitivity is achieved by enhancing efficiency in absorption and transduction by the detector. Absorption is enhanced by using plasmonic absorbers. Transduction efficiency is increased by using VO_2 beams near highest sensitivity temperature (transition temperature). The results indicate improvements in multiple performance parameters of the bolometer such as - responsivity, detectivity, noise equivalent power, pixel density, bandwidth, etc.

1.2 Organization of the Dissertation

The dissertation is structured as follows: Chapter 1 provides a brief overview of radiation detectors and the research objective. Chapter 2 discusses the fundamentals of plasmonics, particularly plasmonic absorbers and their potentials in optical sensing. Chapter 3 focuses on the aspects of bolometer physics and phase-transition material (PTM) especially vanadium dioxide (VO_2). Chapter 4 demonstrates a plasmo-thermomechanical radiation detector made of a Si_3N_4 waveguide and a suspended metallic fishbone nanowire array whose sensitivity and bandwidth is augmented by a graphene layer. This chapter includes mechanical and electromagnetic modeling. Chapter 5 covers high-resolution bolometer designed for 10 μm infrared wavelength radiation detection with integrated plasmonic absorbers and VO_2 nanobeam. This chapter includes comprehensive analysis of the electromagnetic modeling of plasmonic absorbers, study of material properties and geometric design parameters, their effect on the performance, scalability of the design, as well as expected system performance. Chapter 6 includes a polarization-sensitive THz detector implemented with similar design principles demonstrating the scalability and added functionality of the original design at IR band. Chapter 7 includes proof-of-concept fabrication methods and experimental characterization results including electronic and spectral analysis. Finally, the dissertation concludes with a summary of the work in Chapter 8 and a discussion of possible future research directions.

Chapter 2

Plasmonic Absorbers

2.1 Background

Plasmonics along with its incorporation in optical devices is a burgeoning field of science and technology that capitalizes on the optical properties of metallic nano-structures to confine and manipulate light at the nanoscale beyond the diffraction limit. The ability of plasmonic devices to confine and direct light within sub-wavelength structures is a highly desirable attribute, as it opens up the possibility of creating plasmonic circuits that are miniaturized and possess feature sizes that are comparable to electronic circuits. The sub-wavelength confinement of light enabled by surface plasmon polaritons (SPPs) - coupled wave of light and collective oscillation of free electrons on the metal surface has brought forth compact optical and photonic devices offering unique electromagnetic properties. Additionally, plasmonic devices have also been employed in the medical and biological realms, such as biosensing, diagnostics, and treatment. Surface-enhanced Raman spectroscopy (SERS), a technique that detects single molecules and analyzes material components, has become widespread due to the electric-field enhancement effect by metallic nanostructures. Along with metallic nanostructures, graphene and other 2D materials [1] have also been widely researched over the last two decades for their extra-ordinary plasmonic and optical properties leading to noble applications.

Plasmonic absorbers are structured materials arranged and designed to efficiently absorb and convert incident electromagnetic radiation into heat through the excitation of plasmons. Plasmons are collective oscillations of free electrons in a material that are coupled to an electromagnetic field. In a plasmonic absorber, the material or structure is designed to support the excitation of plasmons at a specific frequency range, usually in the visible or infrared region of the electromagnetic spectrum. When the incident radiation matches this frequency range, the plasmons are excited, and the energy is absorbed and converted into heat or any other form of energy. This absorption process can be very efficient, as the plasmons can strongly couple with the incident radiation. Plasmonic absorbers have a wide range of applications, including in solar energy conversion [2, 3, 4], thermal management [5, 6], and sensing [7, 8]. They can be designed to have high absorption efficiency, tunable absorption spectra, and can be integrated into various devices and systems.

2.2 Maxwell's Equation

Plasmonic devices employ the excitation of plasmons - coherent oscillations of electrons coupled with an electromagnetic wave along the boundary between a metal (such as silver or gold) and a dielectric (such as air or glass). The interaction between metals and electromagnetic fields can be described using Maxwell's equations [9]:

$$\nabla \cdot \mathbf{D} = \rho_s \qquad \text{(Gauss's Law)} \tag{2.1}$$

$$\nabla \cdot \mathbf{B} = 0 \qquad \text{(Gauss's Law for Magnetic)} \tag{2.2}$$

$$\nabla \times \mathbf{E} = -\partial \mathbf{B}/\partial t \qquad \text{(Faraday's Law)} \tag{2.3}$$

$$\nabla \times \mathbf{H} = \mathbf{J_s} + \partial \mathbf{D}/\partial t \qquad \text{(Ampere's Law)} \tag{2.4}$$

which relates macroscopic fields (electric field **E**, magnetic field **H**, electric flux density **D**, magnetic flux density **B**) to the applied current density $\mathbf{J_s}$ and charge density $\rho_\mathbf{s}$. For linear, isotropic, and non-magnetic materials, **D** and **B** are related to **E** and **H** as:

$$\mathbf{D} = \epsilon_0 \epsilon \mathbf{E}$$

$$\mathbf{B} = \mu_0 \mathbf{H}$$

where ϵ is the dielectric constant, $\epsilon_0 = 8.854 \times 10^{-12} F/m$ and $\mu_0 = 4\pi \times 10^{-7} H/m$ are the electric permittivity and magnetic permeability respectively in vacuum or air medium. The dielectric constant of material is frequency dependent and in general a complex function. It relates to the complex index of refraction as $\epsilon = \epsilon' - j\epsilon'' = \mathbf{n}^2 = (n - j\kappa)^2 = (n^2 + \kappa^2) - j2n\kappa$. The real part of the refractive index, n is responsible for the dispersion of light as it passes through the material. The imaginary part of the refractive index is represented by the extinction coefficient, κ and determines the amount of light that is absorbed by the material. The absorption of light by a material occurs when the energy of the incident photons is transferred to the material, causing its atoms or molecules to vibrate or excite. This can cause the light to be converted to heat or to be re-emitted at a lower frequency. The greater the value of κ, the more light is absorbed by the material.

Faraday's law and Ampere's law can be combined to produce three-dimensional electromagnetic wave equation in a non-magnetic conducting medium as:

$$\nabla^2\mathbf{E} - \mu_0\sigma\frac{\partial \mathbf{E}}{\partial t} - \mu_0\epsilon_0\epsilon\frac{\partial^2 \mathbf{E}}{\partial t^2} = 0 \tag{2.5}$$

where σ is the electric conductivity of the medium and $\mathbf{J} = \sigma\mathbf{E}$. For a dielectric medium, the electric conductivity can be considered negligible. The solution of the equation is of the form:

$$\mathbf{E} = \mathbf{E_0}e^{j(\omega t - \mathbf{k}.\mathbf{r})} \tag{2.6}$$

where $\mathbf{E_0}$ is a constant vector, $\mathbf{r}$ is position vector. Angular frequency, ω and wave vector, $\mathbf{k}$ are related to the wave's frequency, f and wavelength, λ by $\omega = 2\pi f$ and $|\mathbf{k}| = 2\pi/\lambda$. Substituting equation 2.6 into equation 2.5 leads to the dispersion relation:

$$-\mathbf{k}^2 - j\omega\mu_0\sigma + \omega^2\mu_0\epsilon = 0 \tag{2.7}$$

where,

$$\mathbf{k} = \vec{\alpha} - j\vec{\beta} \tag{2.8}$$

$$|\vec{\alpha}| = \omega\sqrt{\mu_0\varepsilon}\left[\frac{1}{2} + \frac{1}{2}\sqrt{1 + \frac{\sigma^2}{\omega^2\varepsilon^2}}\right]^{1/2} \tag{2.9}$$

$$|\vec{\beta}| = \frac{\omega\mu_0\sigma}{2|\vec{\alpha}|} \tag{2.10}$$

The solution of equation 2.6 is now of the form $\mathbf{E} = \mathbf{E_0} e^{j(\omega t - \vec{\alpha}.\mathbf{r})} e^{-\vec{\beta ..}\mathbf{r}}$. The first exponential factor denotes the wave-like oscillation of the electric field and the second exponential factor denotes the decay of the amplitude. Using numerical tools like finite element method (FEM) or finite difference time domain (FDTD) solver, Maxwell's equations or wave equation can be solved in a complex geometric structures in a device to obtain the electric and magnetic field distribution and extract device electromagnetic properties.

2.3 Localized Surface Plasmons

Optical properties of materials can be described using the plasma model, where the medium or material is considered like an electron gas comprised of free electrons. Bulk plasmons are collective oscillations of such free electrons in a bulk material when coupled to an electromagnetic field. In the case of bulk plasmons, the oscillations occur throughout the bulk of the material, as opposed to surface plasmons (also surface plasmon polariton or SPP) [10, 11], which propagates along the interface between a metal and a dielectric medium (such as air or water). Phase matching is required to excite SPP modes. This can be achieved by special techniques like prism or grating coupling, tightly-focused optical beams, or near-field excitation. Controlled coupling and propagation of SPPs along waveguiding structures can be achieved, for example, by using thin metal films sandwiched between two dielectric layers. Metallic wires can support guided waves propagating in one dimension forming the basis of plasmonic waveguides [12, 13].

On the other hand, dimensionally bound metal dielectric interfaces, such as metal nanoparticles or nanostructures, produce non-propagating coupled electromagnetic wave and electron oscillation. These are called localized surface plasmons (LSP) [14, 15]. Unlike, SPP modes, LSPs do not need any special techniques to be excited. Creation of such plasmonic modes leads to strong confined electric field resulting in increased sensitivity, increased thermal energy, etc. depending on application. When considering small, isolated metal particles that are approximately the same size as the depth to which an electromagnetic field can penetrate (around 20 nm for Ag in the optical range), surface and bulk plasmons becomes non-distinguishable. In these cases, an external electromagnetic field is able to penetrate into the particle's volume, causing the conduction electrons to shift in relation to the ion lattice. The electrons that have shifted in a coherent manner, along with the restoring field, make up an oscillator that is influenced by the effective electron mass, charge density, and particle geometry, which together determine its behavior. If the incident electromagnetic wave is in resonance with the oscillation, the amplitude of the induced field can get amplified by a factor known as field enhancement factor. This localized surface plasmon resonance or LSPR induced field enhancement is the basis of plasmonic absorbers.

The primary characteristic of localized surface plasmon polaritons (LSPPs) is that the energy becomes concentrated in a specific, isolated area after excitation, which is where the name comes from. The resonance is determined by the shape of the individual absorbing elements, particularly the portion that confines light, while the impact of neighboring absorbing elements interacting with each other is minimal.

2.4 Metal-Insulator-Metal Absorber

A metal-insulator-metal (MIM) absorber [16, 17] is a type of thin-film metamaterial absorber that consists of two metallic layers separated by a thin insulating layer. When light is incident on the MIM absorber, the metal layers act as antennas to absorb the incident radiation, and the insulating layer serves to confine the electromagnetic energy within the structure.

The field distribution profile of a MIM absorber is shown in Fig. 2.1. The top and bottom layers of the absorber experience induced anti-parallel oscillating fields. The electric displacement vectors in the bottom layer and the micropatches are opposite to each other, which generates a strong magnetic response. Additionally, the sides of the top layer micropatches exhibit strong electric dipole resonances. These localized magnetic and electric dipole or LSPP resonances result in substantial absorption by the metals through ohmic losses, leading to temperature development. The MIM absorber thus converts the absorbed light into ohmic loss induced thermal energy.

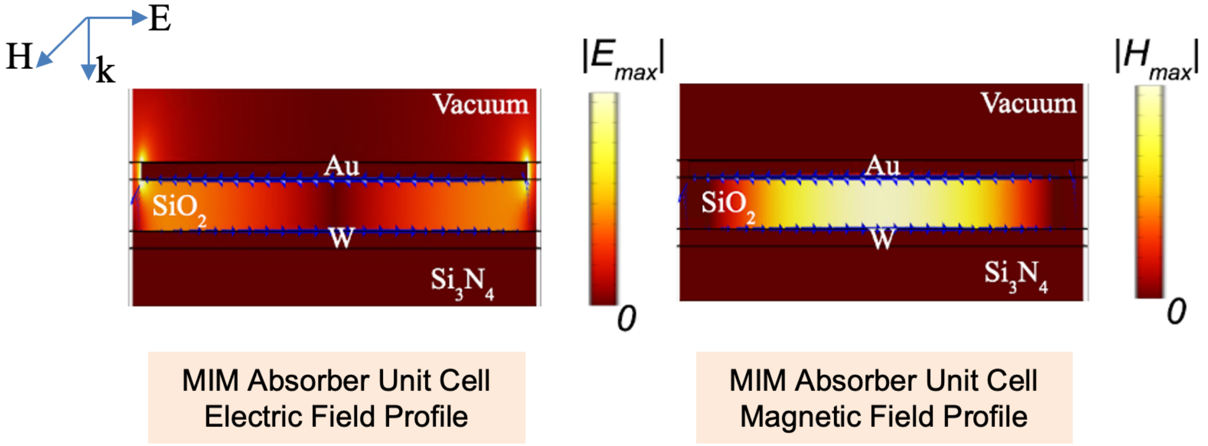

Figure 2.1: Field profile for resonant radiation incidence on a M-I-M absorber showing electric dipole resonance and magnetic resonance.

MIM absorbers are attractive as they offer several advantages over traditional absorbers - easy fabrication methods using simple and low-cost deposition techniques, they can be made very thin, and they exhibit strong light absorption in the frequency or wavelength band they are designed for - visible, infrared as well as terahertz (THz) regions of the spectrum. Additionally, MIM absorbers can be tuned to absorb specific wavelengths of light by adjusting the thicknesses or dimensions of the metal and insulating layers, which makes them potentially useful for a wide range of applications in solar cells, sensing, and radiation detectors. They offer absorption tunability and efficiency by geometric control allowing more flexibility of material choice.

MIM absorbers employ localized surface plasmon polaritons (LSPPs) to achieve high performance and design flexibility based on geometry beyond diffraction limit rather than material composition. As such, these absorbers are able to achieve sufficient performance with a small footprint and thin design for both visible and infrared wavelengths as well as THz frequencies.

Chapter 3

Bolometer Physics

3.1 Background

The two main types of infrared (IR) detectors are thermal detector and photon detector. The thermal detectors function based on the principles of temperature dependent phenomena - change in resistance, voltage generation in junction, change in polarization, thermal expansion of gas, etc. On the other hand, photon detectors functions by converting IR radiation into photo generated free carriers [18]. At present, high-performance infrared imaging technology is mainly based on epitaxially grown structures of the small-bandgap bulk alloy mercury-cadmium-telluride (MCT) [19, 20]. Quantum-well infrared photodetectors based on $InSb$, $GaAs$, $InGaAs$ and others are also available [21, 22]. However, these technologies require very low operating temperature ($<$ 240 K) increasing the bulkiness and cost of the system [18, 19].

Unlike photon detectors, thermal detectors can operate without cryogenic cooling, which is both costly and power-intensive. Although thermal detectors are typically slower and less sensitive than photon detectors, they have the ability to absorb energy over a wider range of wavelengths and to operate at or near room temperature making them a more cost-effective and power-efficient alternative to photon detectors.

The need for increased performance of the infrared detectors has driven extensive research towards the improvement in current IR detection technology as well as spurred novel techniques and sensors [23, 24, 25]. The advancement of integrated optics [26, 27] and photonic integrated circuits has brought forward both IR detection and readout capability in the same chip [28, 29, 30]. However, there is still requirement for higher sensitivity and higher pixel density detectors for critical applications and high-resolution thermal imaging and sensing for medical and military purposes.

A microbolometer is a type of thermal detector that measures changes in resistance caused by heat induced by radiation incidence. Such detectors require thermal isolation to achieve high sensitivity which is achieved by following Micro-Electromechanical Sensor (MEMS) device fabrication techniques. The device is composed of a thin dielectric membrane (usually Si_3N_4) which is suspended over a substrate and linked to it by two or more support arms. The membrane supports the transducer element can be either a metal or a semiconductor, changes its resistance upon radiation-induced temperature variation. The Temperature Coefficient of Resistivity (TCR) measures the amount by which the transducer's resistance changes with temperature. TCR is positive for metals and negative for semiconductors, and a high TCR is desirable for increased sensitivity. However, the room temperature resistivity of the transducer should be low for noise considerations. Most microbolometers [31] use high TCR films as transducer elements, such as platinum [32], titanium [33], amorphous silicon [34], and amorphous vanadium oxide (VO_x) [35]. However, in this work, transducer element is chosen to be a rectangular beam to achieve enhanced sensitivity; discussed in Chapter 5 in detail.

3.2 PTM and VO_2

Phase-changing or phase-transition materials (PCM, PTM) hold significant potential in optical and thermal sensing and switching due to their sharp temperature dependent characteristics. Vanadium dioxide (VO_2) is the most utilitarian PCM because of its close-to-room-temperature transition point and high TCR. The latter property is exploited in many reported microbolometers [31, 35, 36]. Most commonly reported value for this semiconductor-to-metal transition temperature of VO_2 films is 68°C [37]. However, the film and deposition technique can be engineered to further lower the transition even closer to the room-temperature [38, 36] with a narrower hysteresis. At the transition point, resistivity of VO_2 material undergoes over three [37] to four [39] orders of change in magnitude. VO_2-based bolometers utilize the material's large temperature coefficient of resistivity (TCR) [36, 40] to detect infrared radiation. The VO_2 film can be nanoengineered [36, 41, 42] to improve bolometer sensitivity. In addition, there has been development on MEMS-based bolometers [43] and integration of patterned coating [44] for improved performance. However, the active radiation absorption area still needs to be large enough that allows sufficient temperature buildup from incident radiation absorbed by VO_2, thus requiring large pixel dimension and degrading the spatial resolution of bolometric sensing. The fabrication process dependence and close co-existence of different oxides [45, 46, 47, 48, 49] of the deposited vanadium films pose challenges in obtaining high-TCR film thus degrading detector performance. Moreover, the absorption by the VO_2 material is not optimized for a specific frequency band in most of the applications. Nanostructured or nanobeam VO_2 has been used to compensate the degradation of TCR and achieve higher sensitivity [36, 50].

On the other hand, to achieve increased absorption for a specific band of incident radiation by reduced-size pixel, plasmonic micro and nanostructures [51, 52, 53, 54] can be designed and tuned. The VO_2 micro/nanobeam and plasmonic nanostructures thus have the potential to be incorporated together for sensitive bolometric detection. The prevalent design dilemma between the obtained thermal resolution and spatial resolution, bolometric bandwidth and performance, sensitivity and noise need to be analyzed in order to achieve an optimized detector.

3.3 Infrared Radiation

Infrared (IR) is a band of electromagnetic radiation that has a longer wavelength than visible light but shorter than radio waves. Infrared radiation is emitted by all objects with a temperature above absolute zero, and it can be detected by specialized sensors and cameras. The wavelength at which an object radiates most intensely depends on its temperature. In general, cooler objects show up more prominently at farther infrared wavelengths. The amount of emitted radiant energy depends on the object's emissivity. Thus, infrared radiation holds the temperature and associated signatures of all objects.

Infrared radiation is divided into three main bands: near-infrared (NIR), mid-infrared (MIR), and far-infrared (FIR). Each category has a specific wavelength range and is used for different applications. NIR band has a wavelength range from 780 nm to 2.5 μm and is commonly used in fiber optic communication, spectroscopy, and sensing. It is also used in the study of plant health and vegetation growth. MIR band ranges from 2.5 μm to 50 μm and has application in thermal imaging, chemical sensing such as identifying chemical compounds, and environmental monitoring such as measuring air pollution levels and tracking weather patterns. It is also used in medical applications, such as identifying tumors and diagnosing diseases. FIR band is defined from 50 μm (6 THz) to 1000 μm (0.3 THz). It is used in astronomy and some medical applications, such as detecting breast cancer and imaging the eye. It is also used in material science to study the properties of materials and in non-destructive testing to detect defects in materials. There are also sub-bands within each of these main bands, which are further divided based on specific wavelength ranges and applications.

A blackbody refers to an object that absorbs all electromagnetic energy that falls on it and, according to the law of conservation of energy, must radiate this energy perfectly if it is in a state of thermodynamic equilibrium. Although achieving a perfectly blackbody object is only theoretically possible, many objects exhibit behavior that is close to a blackbody. The sun, for instance, can be approximated as a blackbody, with its peak emission occurring at a wavelength of 0.5 μm, which is in the middle of the visible spectrum. However, the sun also functions as a source of broadband infrared radiation, which we experience as heat, and Earth's atmosphere limits the transmission of this radiation to specific wavelength ranges based on its constituent molecules. Short-wave infrared (SWIR, 1.4 - 3 μm), mid-wave infrared (MWIR, 3 - 8 μm), and long-wave infrared (LWIR, 8 - 15 μm) are commonly defined specific sub-bands of the infrared spectrum, based on the transmission windows of the Earth. Human body is not a perfect blackbody, but can be modeled as one for estimation. A person's skin temperature may be around 33-34°C (91-93°F), while their internal body temperature is around 37°C (98.6°F). Therefore, the radiation emitted by the body will vary depending on the specific location and temperature of the emitting surface.

An infrared detector is a device designed to convert infrared radiation into measurable electrical signals. By using a two-dimensional detector array, also known as a Focal Plane Array (FPA), it is possible to create infrared images that are useful for "night vision" applications based on the infrared radiation that objects emit rather than the sunlight that they reflect. This technology is particularly effective in environments where shorter optical wavelengths are obscured by Rayleigh scattering, such as fog, smoke, or dense dust, but where infrared radiation remains unaffected, particularly in the LWIR band. Infrared imagers have a broad range of applications, including defense, surveillance, security, and emergency response.

3.4 Imaging System

An infrared imaging system consists of imaging optics, focal plane array (FPA) containing array of detector pixels, electronic read out circuit or application-specific integrated circuit (ASIC) in a hermetically sealed package. A conceptual block diagram of such imaging system is shown in Fig. 3.1.

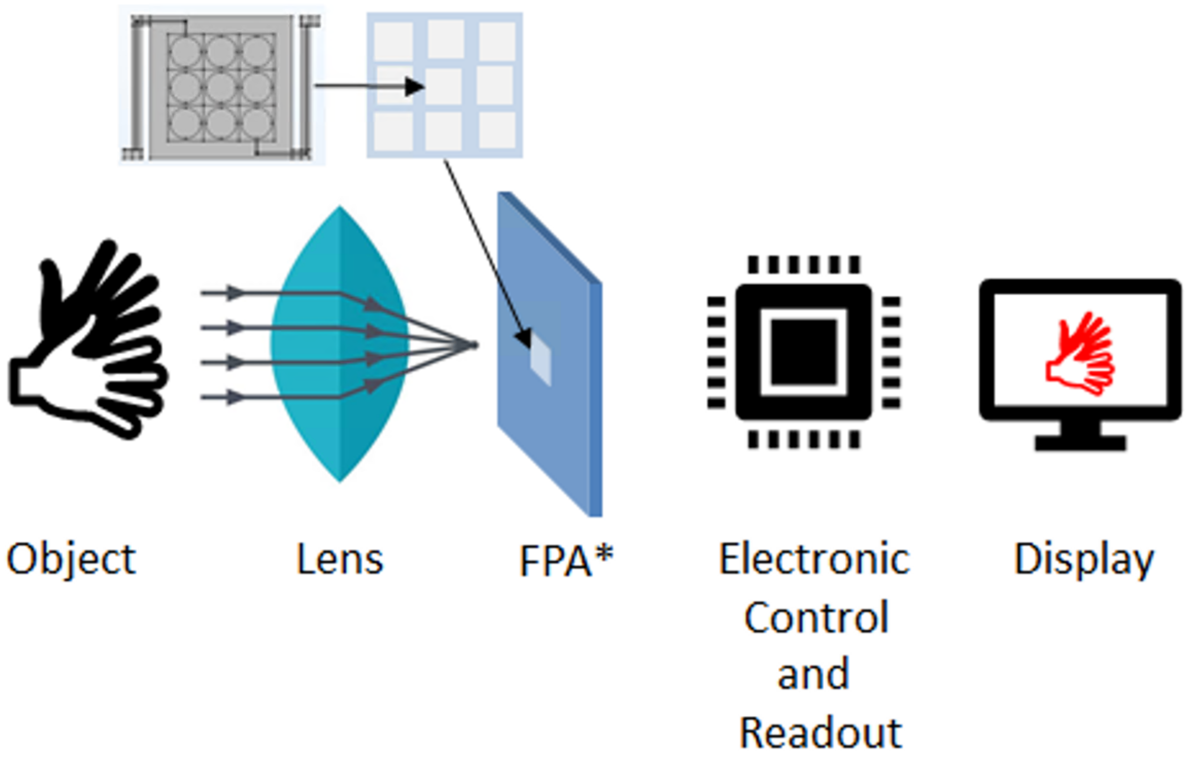

Figure 3.1: Conceptual block diagram of an imaging system. The emitted electromagnetic radiation from an object is focused by lens onto the FPA. The pixels on the FPA detects the spatial temperature profile of the object which is detected electronically and later processed to display the thermal image of the object.

The imaging optics usually consist of a combination of focusing lens that focused the emitted radiation from object on the FPA or active area of the detector. The lens material needs to be transmissive at the wavelength of operation and may be coated with filters to block other wavelengths. For LWIR, for instance, Ge or CaF_2 lens needs to be used as they are transparent at those wavelengths. Commonly used lens for visible or NIR will not be suitable here.

The FPA contains array of detector pixels. For bolometers, the pixels are usually suspended and supported by a dielectric membrane with two or more legs to create thermal isolation from the substrate. Such thermal isolation ensures sufficient temperature buildup for high sensitivity. The electronic control and readout circuitry are laid out underneath the active detector area using CMOS processes. The readout data is processed to display the thermal image or other useful information of the object. The FPA can be placed and packaged within a vacuum housing with a thermo-electric controller to actively control the detector temperature.

Detector pixels can be designed in different way. In this work, each pixel consist of multiple plasmonic absorber patches and one readout VO_2 transducer beam. The size of the pixel determines the spatial resolution or pixel density. Overall sensitivity from object's temperature to readout signal defines the thermal resolution of the detector. The number of pixels in a detector and the pixel time constant determines the electronic requirements such as power consumption and clock speed.

3.5 Human Body Radiation

Human body is not a perfect blackbody. However, it can be modeled as one for approximation. Planck's blackbody radiation theory defines the emitted energy from an object in relation to its temperature over a specific wavelength as:

$$E_\lambda = \frac{2\pi hc^2}{\lambda^5 \left[e^{\frac{hc}{\lambda kT}-1}\right]} \tag{3.1}$$

where, $h = 6.6 \times 10^{-34} Js$ is the Planck's constant, $c = 3 \times 10^8 m/s$ is the speed of light in vacuum, $k = 1.38 \times 10^{-23} J/K$ is the Boltzmann constant, T is the object temperature, λ is the wavelength of radiation, E_λ is emissive power per unit area per wavelength. Applying equation 3.1 near human body temperature yields the emitted radiation energy distribution over wavelength shown in Fig. 3.2 (a).

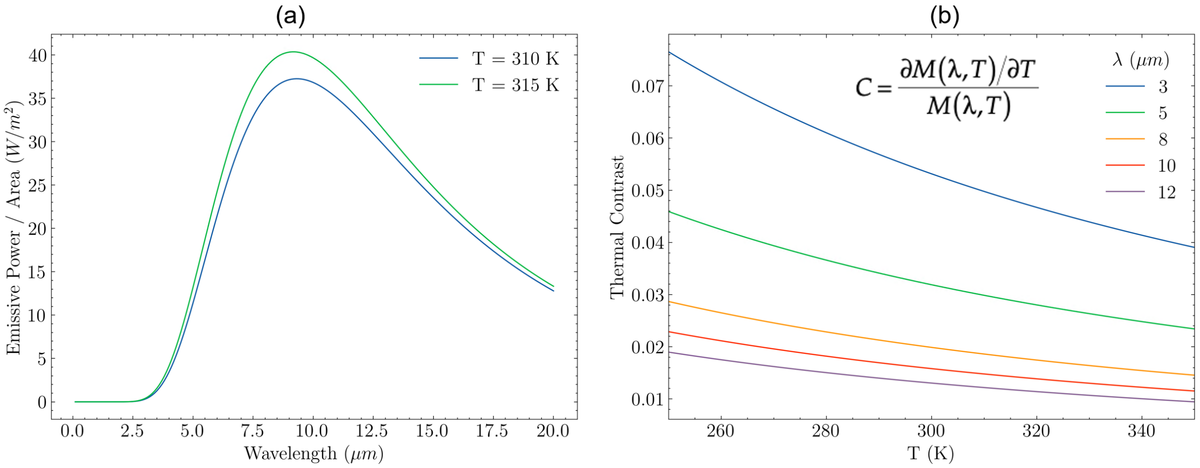

Figure 3.2: Radiation profile and thermal contrast over wavelength and temperature. (a) Blackbody radiation near human body temperature, (b) Thermal contrast for different wavelengths

For a blackbody object at 315 K and 310 K, peak power is 40.36 $W.m^{-2}.\mu m^{-1}$ at 9.2 μm and 37.26 $W.m^{-2}.\mu m^{-1}$ at 9.3 μm wavelength, respectively. The peak radiation wavelength λ_{max} can also be approximated using Wien's displacement law, $\lambda_{max} \approx \frac{2880}{T}\mu m$, where T is in Kelvin. As observed, the change in radiation profile with temperature is not very strong, and here lies the challenge to precisely detect a small range of temperature for LWIR imaging. The underlying challenge becomes more clear in Fig. 3.2 (b) which shows the thermal contrast at a few different wavelengths over a temperature range from 250 to 350 K. The thermal contrast is the ratio of the thermal derivative of the spectral radiant exitance ot the spectral radiant exitance, $M(\lambda, T)$ [55] i.e., $C = \frac{\partial M(\lambda,T)/\partial T}{M(\lambda,T)}$. At longer wavelengths, the thermal contrast degrades making it more challenging to detect small temperature difference in the object being imaged. The challenge clearly points out the necessity of high-sensitivity detection for high-resolution imaging particularly at longer wavelengths. Another important thing to consider is the ground level solar radiation power and the object radiation power.

If the solar radiation power is comparatively strong, the object radiation signature will get obscured. The ground level solar radiation power at 3-5 μm and 8-13 μm wavelength bands are 24 and 1.5 W/m^2, respectively. The emissive power from a blackbody at 290 K temperature for the respective wavelength bands are 4.1 and 127 W/m^2 [56]. As such, 8-13 μm or LWIR bands are more suitable for thermal imaging of objects near room temperature.

3.6 Bolometer Model

Figure 3.3 illustrates a standard microbolometer model and its corresponding design parameters. The two essential parameters for a bolometer are its thermal conductance, G_{th}, and its heat capacitance, C_{th}. Infrared sensitivity increases with larger thermal buildup, which is achieved by reducing heat escape mechanisms to lower thermal conductance. Consequently, the radiative limit is the optimal performance limit. To decrease heat escape through conductance, various structural modifications can be employed, such as using suspended membranes to reduce vertical heat transfer. Additionally long, thin, and narrow arms can be implemented to reduce lateral heat transfer. The thermal time constant of the detector is inversely proportional to its thermal conductance and directly proportional to its thermal resistance, which can be expressed as:

$$\tau_{th} = \frac{C_{th}}{G_{th}} = C_{th}R_{th} \tag{3.2}$$

This trade-off between the detection bandwidth and heat capacity is crucial to consider, as the time constant determines the maximum refresh rate in thermal cameras.

The temperature increase in the bolometer upon radiation incidence can be found by applying heat balance equation [55]

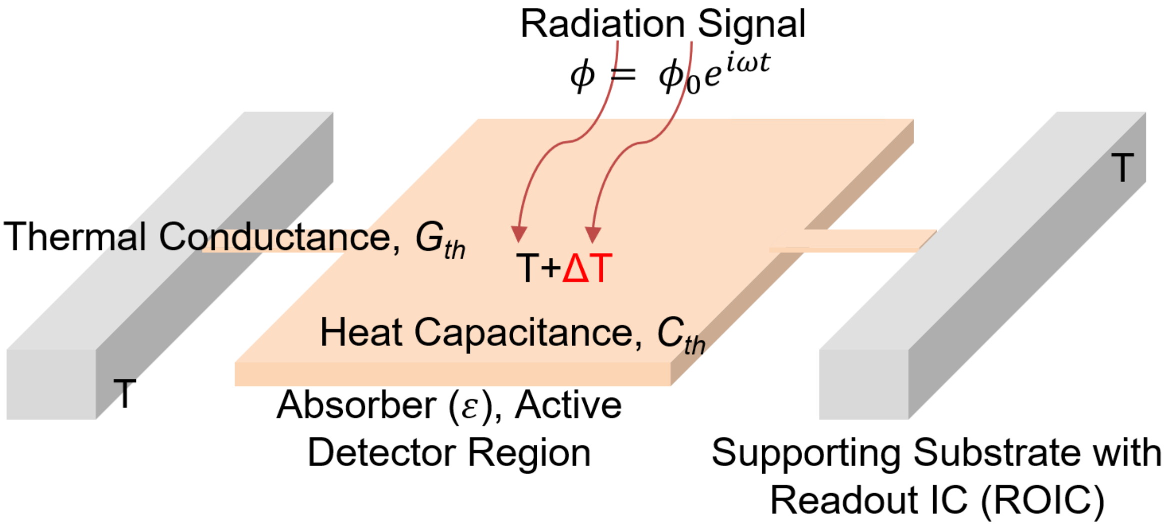

Figure 3.3: Microbolometer model showing two important parameters of a bolometer - thermal conductance and heat capacitance.

$$C_{th}\frac{d\Delta T}{dt} + G_{th}\Delta T = \varepsilon\Phi \tag{3.3}$$

where ΔT is the temperature difference created by radiation signal $\Phi = \Phi_o e^{i\omega t}$ as the incident radiation is assumed to be modulated with a frequency $f = \frac{\omega}{2\pi}$, and ε is the emissivity or absorptance of detector. The detector is usually DC-biased with a constant current source to measure the change in resistance upon radiation incidence. The bias current also contributes to Joule heating. However, choosing a very small bias current (e.g., $\leq 1\mu$A) can limit such bias current induced Joule heating to a level that can be ignored. The solution is found as:

$$\Delta T = \frac{\varepsilon\phi_0}{(G_{th}^2 + \omega^2 C_{th}^2)^{1/2}} = \frac{\varepsilon\phi_0 R_{th}}{(1 + \omega^2\tau_{th}^2)^{1/2}} \tag{3.4}$$

The readout voltage is thus:

$$\Delta V = \frac{K\varepsilon\phi_0 R_{th}}{(1+\omega^2\tau_{th}^2)^{1/2}} \tag{3.5}$$

where $K = I_{bias} \times R \times TCR$; I_{bias} being the bias current, R is the resistance across readout terminals, TCR is the temperature-coefficient of resistivity of the sensing component.

The responsivity, R_v of bolometer is defined as the voltage signal generated for a 1 W of incident power. Thus–

$$R_v = \frac{K\epsilon R_{th}}{\sqrt{(1+\omega^2\tau_{th}^2)}} \tag{3.6}$$

Another important performance metric is the noise equivalent power (NEP) that is defined as the incident power level that produces a signal-to-noise ratio (SNR) of 1. Its relation to the bolometer design parameters is presented as:

$$NEP = \frac{\Delta P_{th}}{\kappa} = \frac{\sqrt{4kT^2G_{th}}}{\sigma_s} \tag{3.7}$$

where ΔP_{th} is the thermal noise power, σ_s is Stefan's constant, k is Boltzmann's constant, T is device temperature in Kelvin.

The detectivity, D is the inverse of NEP, i.e., $D = 1/NEP$. However, a normalized detectivity, $D^* = D\sqrt{A\Delta f}$ is used more commonly [57] to easily compare similar detectors of different active areas. The normalized detectivity relates to bolometer parameters as [58]

$$D^* = K\varepsilon R_{th}\sqrt{\left[\frac{A}{(1+\omega^2\tau_{th}^2)\left(\frac{4kT^2K^2R_{th}}{1+\omega\tau_{th}^2}+4kTR_V\right)}\right]} \tag{3.8}$$

3.7 Bolometer Noises

The major sources of noise in a bolometer detector are Johnson or resistive noise (V_j), thermal fluctuation noise (V_{th}), flicker noise ($V_{\frac{1}{f}}$), and background noise (V_b). Johnson noise is a white noise and arises from the detector resistance and is proportional to the device bias temperature. It is defined as -

$$V_j = \sqrt{4kTR\Delta f} \tag{3.9}$$

where k is Boltzmann constant, T is detector temperature, R is the readout resistance, and Δf is the measurement bandwidth. The Johnson noise depends on the bandwidth, operating temperature, and the resistance of the device.

Thermal fluctuation is usually the second most dominant noise source. It arises from the temperature fluctuation of the detector and is proportional to the thermal resistance. As a result, the effort to improve the sensitivity by increasing thermal resistance also increases the thermal fluctuation noise. The temperature fluctuation noise, ΔT_n of the device causes corresponding thermal fluctuation voltage, V_{th} to appear as noise contribution and is expressed as-

$$V_{th} = \sqrt{K^2 \Delta \bar{T_n}^2} = 2KT\sqrt{\frac{k\Delta f}{(1+\omega^2\tau_{th}^2)}R_{th}} \tag{3.10}$$

Another source of noise - the background noise, V_b is the noise due to radiative heat exchange between the detector with temperature, T_D and surrounding background with a temperature T_b. It is expressed as -

$$V_b = \sqrt{\frac{8k\epsilon\sigma A\left(T_d^2 + T_b^2\right)}{\left(1+\omega^2\tau_{th}^2\right)}}KR_{th} \tag{3.11}$$

where, σ is the Stefan-Boltzmann constant.

Chapter 4

Plasmo Thermo-mechanical Radiation Detector

4.1 Device Model

The proposed optomechanical device consists of a 1.5 μm wide and 0.3 μm thick Si_3N_4 waveguide and an array of graphene-coated suspended metallic fishbone nanowires above, as illustrated in Figure 4.1. The experimental demonstration[28] consisted of bimetallic antennas without graphene-layer having 20 nm nickel and 30 nm gold for optimized maximum deflection in response to radiation. As the free-space radiation is applied on the nanowires, the plasmonic resonant absorption by the integrated antennas creates a thermal gradient along the nanowires. The temperature reaches maximum at the middle of each of the nanowires which is also the maximum deflection point as expected. The mechanical deflection causes the gap between the waveguide and suspended metallic structures to vary. The coupling between the evanescent waveguide mode to the nanowires changes depending on the gap which in turn changes the insertion loss of the waveguide. Thus, the free space

IR radiation can be measured by sensing the probe light through the waveguide. The whole system can operate at room-temperature and can be integrated on the silicon platform.

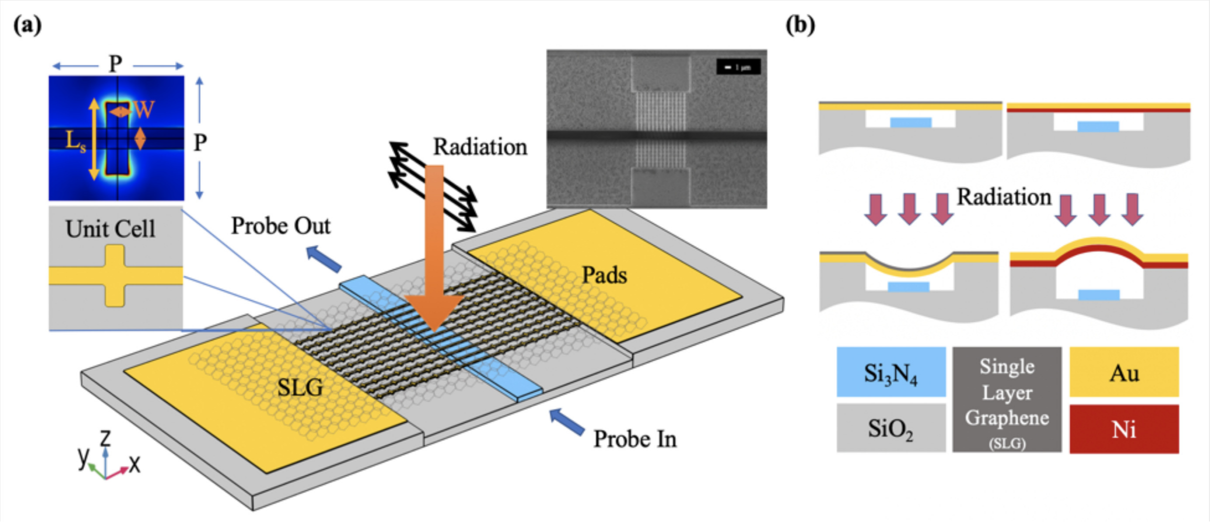

Figure 4.1: (a) Geometry of the whole system – the fishbone nanowire array with graphene is suspended above a Si_3N_4 waveguide. The plasmonic nanowires selectively absorb free-space IR radiation. The inset shows the unit cell (graphene layer not shown) and its field distribution at resonant absorption. Inset on the right shows the SEM top view image of the detector containing fishbone suspended metallic nanostructures and the waveguide. (b) Plasmonic heating causes the suspended layer to expand and mechanically deflect, modulating the gap between waveguide and plasmonic structures. The insertion loss of the waveguide thus reflects the incident radiation. The deflection magnitude and direction depend on the thermal expansion coefficients of the materials.

The sensitivity of the device is measured by the absorption efficiency of free space radiation. For an absorption coefficient of 0.338 of the designed antenna[28] at near IR, the bimetallic nanowires were estimated to deflect about 15 nm. The sensitivity of insertion loss of waveguide (S_{21}) was experimentally measured to be 4.3×10^{-3} nm^{-1} in the same work. To increase the sensitivity, we propose to incorporate graphene to the nanowires. Graphene is a two-dimensional material which is simultaneously flexible and strong, and carries extraordinary optical, thermal, and mechanical behavior. Our IR detector employs optically induced thermo-mechanical fluctuations to measure the radiation. Therefore, graphene's properties can be exploited and utilized here. The interplay between graphene and metallic nanostructures has already been proven to be beneficial. Single layer graphene absorbs radiation weakly because of its short interaction length. Even so, enhanced performance of graphene-based photodetectors[59, 60] has been achieved by introducing metallic nanostructures on the detectors to selectively enhance the absorption of radiation and thus the photocurrent. Similarly, metallic absorbers have seen increased absorption coefficient when graphene is incorporated in the system[61] facilitating high-sensitivity plasmonic detection and biosensing. Furthermore, the enhanced interaction between graphene and waveguided-light[62] has spurred significant interest in graphene-based on-chip optical communication devices. We investigate different metallic nanowire and graphene combinations. We have shown over two-fold absorption enhancement by considering a single-layer graphene sheet over the nanowires. This large enhancement is not simply the result of adding a single-layer graphene-sheet as it only absorbs 2.3% of the radiation over a broad wavelength range. We see higher enhancement for thinner metallic films. This is because thinner nanowires allow more interaction between the graphene layer on top and the generated localized surface plasmons.

The temperature created by the absorbed radiation dissipates mostly by conduction. Heat is conducted from the nanowire mid-point to the pads. The temperature at this point has been calculated to rise up over 400 K in some cases. Due to the large area of the pads supporting the suspended nanowires, they are considered to be at ambient temperature (293.15 K) for modelling purposes. The heat dissipation is important since the speed of the device operation depends on the thermo-mechanical relaxation of the nanowires. Having graphene layer on top of the nanowires again proves to be beneficial in this regard, as graphene has a very large thermal conductivity (>5000 $\mathrm{Wm^{-1}K^{-1}}$ reported[63]) that leads to faster heat spreading and accelerated thermal response of nanowires.

Strip antennas are designed and optimized for resonant radiation absorption by varying the antenna dimensions. The unit cell is shown in Figure 4.1 inset along with the field distribution at resonant plasmonic absorption. By default, we set the width of the beam and antenna equal, $W = W_b = W_a = 100$ nm, antenna length, $L = 350$ nm, and period $P = P_x = P_y = 660$ nm. We see the resonance shift by changing the period and length of the antenna. As discussed in a later section, longer antenna length and/or larger antenna period results in longer resonant wavelength. Multiple strip antennas are placed along the nanowires to augment the total absorption. The number of strip-antennas in a beam is chosen so as to keep a balance between temperature buildup and deflection. The number of nanowires is also optimized to give an optimized amount of waveguide insertion loss. The fabricated device consisted of 11 of the 12.54 μm long nanowires each holding 16 strip antennas to produce enough mechanical deflection and modulation of the S_{21} parameter.

4.2 Fabrication and Experimental Characterization

The proposed approach of free-space radiation detection has been verified by an experimental demonstration[28] that include bimetallic suspended nanowire fishbone as antennas and Si_3N_4 waveguides as readout circuit. At the beginning of fabrication, oxide, nitride, and cladding oxide layers are grown or deposited by thermal oxidation, LPCVD, and PECVD respectively. Photolithography and dry etching are done to pattern the waveguide. The bump on the PECVD oxide due to waveguide is removed by chemical-mechanical polishing (CMP) and dry etching. Then e-beam lithography is done to pattern fishbone structure on PMMA resist. After that, metal evaporation and liftoff, hydrofluoric (HF) vapor etching was done to etch the sacrificial SiO_2 layer between the nanowires and the waveguide top facet, thus creating a suspension of nanowires.

The fabricated IR detector is characterized experimentally[28] by measuring the power output of the waveguide. A continuous wave (CW) of 1550 nm (probe) passes through the waveguide with its evanescent fields modulated by the mechanical vibration of the nanowires upon the incident radiation from Laser Diode (LD) of 660 nm. We tune the LD modulation frequency and record the voltage from the lock-in amplifier connected to the power meter at waveguide output end. We calculate the 3dB bandwidth of the detection scheme as 9.6 Hz and a time constant of $\tau = \frac{1}{2\pi f_{3dB}} = 16.6$ ms. The results are shown in Figure 4.2. The voltage reading with respect to LD frequency appears in Figure 4.2(a). We show the sinusoid-like time trace of the filtered power in Figure 4.2(b) as the incident radiation is also a sinusoid.

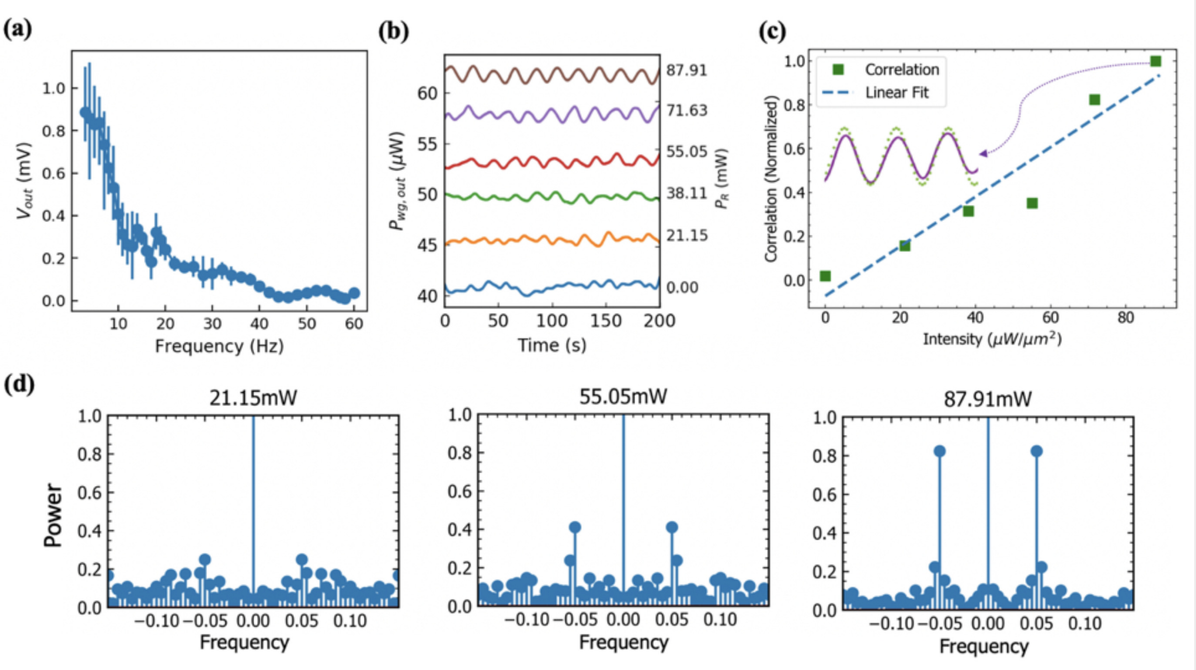

Figure 4.2: (a) The frequency response of the output voltage obtained from a lock-in amplifier which indicates the waveguide output power. (b) The digitally filtered waveguide output power $P_{wg,out}$ for different levels of radiation power, P_R. The $P_{wg,out}$ at different radiation levels have similar average power but are offset along the y-axis according to the radiation power for clarity. The right y axis indicates the incident radiation power. Radiation power is considered to be 0 in the non-illumination case. (c) The correlation between the filtered detected power variation with respect to sinusoidal incident radiation as a function of the peak intensity. Inset shows the incident sinusoidal radiation (dotted green) and detected filtered waveguide output (solid violet), which is the case for a radiation power of 87.91 mW. (d) FFT of raw detected signal for different incident radiation showing sidebands at 0.05 Hz (the modulation frequency), x axis is frequency in Hz and y axis is power in arbitrary unit. Higher incident radiation gives higher sidebands thus higher modulation index.

We also report the normalized correlation between the input sinusoid to the waveguide output signal in Figure 4.2(c). At higher incident power intensity, the correlation is better, and the modulation index is also higher. In the inset of Figure 4.2(c), we can see how well correlated the waveguide output power and LD modulation signal is. Correlation is a metric of how well the detector sensed the time-varying radiation. To illustrate the modulation strength for different radiation power – 21. 15, 55.05, and 87.91 mW, we show the fast Fourier transform. The relative power of the sideband is a measure of the modulation index or modulation strength. We can see the sideband at the modulation frequency (0.05 Hz) is prominent for higher radiation intensity, and it eventually drops below the system induced noise floor at a radiation power lower than about 20 mW.

4.3 Absorption Enhancement by Graphene

Graphene-based photodetectors are limited in terms of absorption due to infinitesimal overlap between photon waves and this monolayer 2D material. However, graphene's absorption can be further enhanced [64, 65] if it is coupled with the proposed antennas. Here, we use finite-element method (FEM) to calculate the absorption coefficient of different metallic nanostructures with and without graphene layer on them. In particular, we use the fishbone or cross geometry because they are easier to fabricate and suspend, and they also show strong plasmonic absorption. We numerically calculate the absorptance using a single unit cell with proper periodic boundary conditions along the repetitive directions, and perfectly matched layer (PML) boundary condition along the direction of propagation. Being a cross-shaped structure, the absorber unit cell contains sharp corners which may lead to electromagnetic singularity. To avoid singular electromagnetic field results, and to resemble a realistic fabricated sample, we have included rounded edges at the corners as shown in the unit cell inset of Fig. 4.1 (a). This allows more precise and realistic predictions of the device characteristics. For the numerical analysis, graphene is considered as a 2D conductive sheet where the conductivity of graphene is modeled as[66]

$$\begin{aligned}\sigma(\omega) &= \sigma^{intra}(\omega) + \sigma^{inter}(\omega)\\ &= i\tfrac{2e^2k_BT}{\pi\hbar\omega} ln[2\ cosh(\tfrac{\mu_c}{2k_BT})] + \tfrac{e^2}{4\hbar}[u(\hbar\omega - 2\mu_c) - \tfrac{i}{2\pi} ln\tfrac{(\hbar\omega+2\mu_c)^2}{(\hbar\omega-2\mu_c)^2)+(2k_BT)^2}]\end{aligned} \tag{4.1}$$

Where, σ^{intra} is intra-band conductivity and σ^{inter} is inter-band conductivity. Here, the step function u determines the inter-band electron transition, k_B is Boltzmann constant, $\hbar$ is reduced Planck's constant, e is electron charge, T is temperature, and we assume, chemical potential of graphene, $\mu_c = 0.45$ eV, a relaxation time of about 0.5 ps, Fermi velocity of 9.5×10^5 ms^{-1}, and a mobility of 9000 cm^{2}V^{-1}s^{-1}.

As evident from Figure 4.3, coating graphene on nanostructures significantly enhances the plasmonic absorption. We observe over 33% enhancement in absorptance when graphene is integrated on 20 nm-thick silver fishbone nanowires. This increased absorption of radiation causes larger temperature gradient, larger mechanical deflection, and as a result, larger modulation of probe light at the waveguide output. For bimetallic nanowires, the ratio between the thicknesses of gold and nickel is kept 1.5 to obtain maximum deflection. However, the absorption does not change much for graphene-nickel or graphene-gold-nickel fishbones. This can be attributed to broader plasmonic absorption by nickel antennas[67]. However, single metal fishbones also give comparable level of absorption with even thinner material layer. This is even more beneficial as using single metallic nanostructure reduces fabrication steps and complexity in comparison to bimetallic ones while achieving higher or same level of absorption performance with the aid of graphene coating.

Since titanium (Ti) layer of 3 nm is used as an adhesion layer during the bimetallic layer deposition for the actual fabrication of the designed IR detector, we consider the effect of this very thin layer in our numerical calculation of absorptance. This adhesion layer is indispensable for depositing metal films, particularly gold films, and almost all the time,

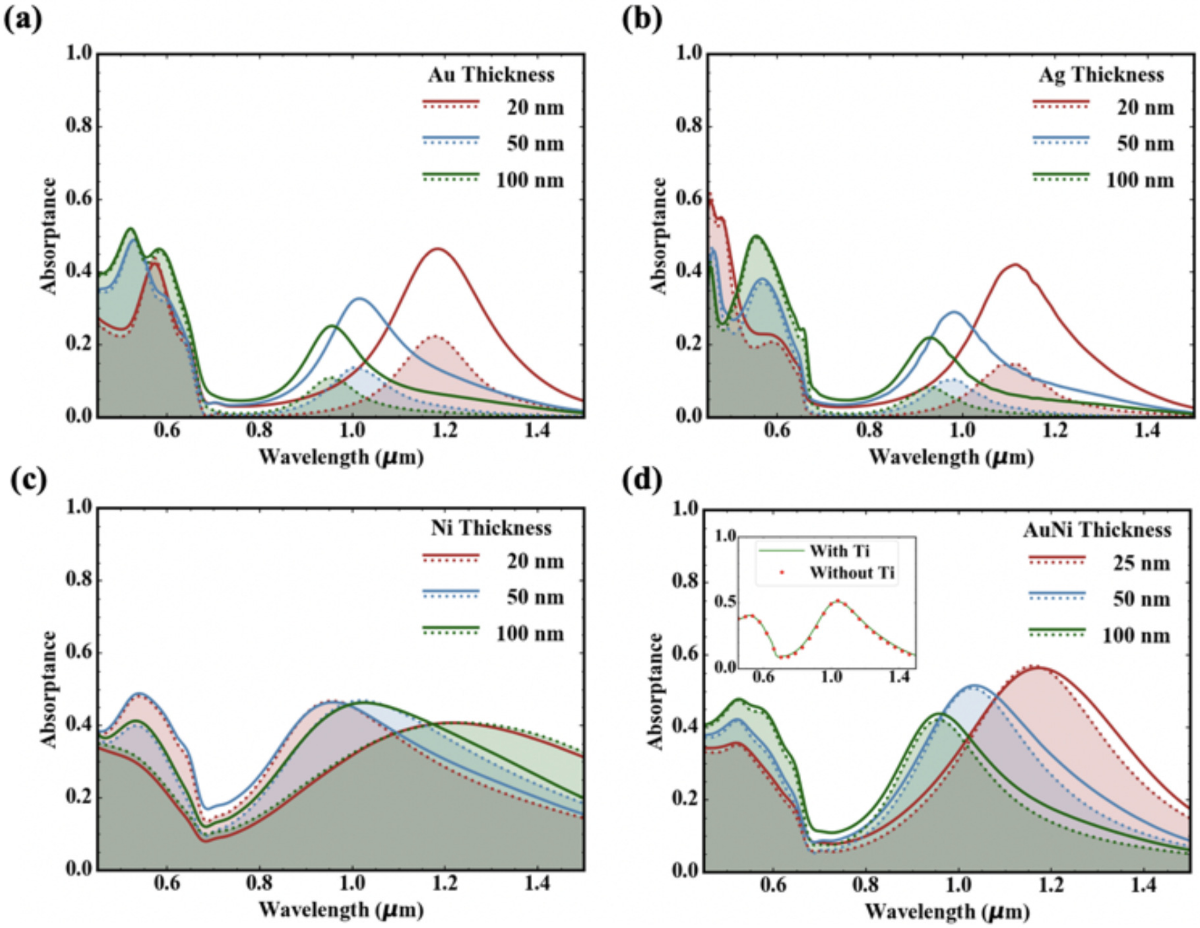

Figure 4.3: Absorptance of suspended fishbone nanostructures with (solid) and without (dotted-filled) graphene coating for different metals - gold (a), silver (b), nickel (c), and gold-nickel (d) of varied thickness. Inset of (d) – The effect of adhesion layer titanium (Ti) on the numerically calculated absorptance of the bimetallic fishbone.

their effect is overlooked as the thickness is negligible compared to other material layers. As we are using an atomically thin graphene sheet in our proposed design, we also examine the effect of having Ti in our FEM study. In the inset of Figure 4.3(d), we see that the adhesion layer Ti does not have any effect on the absorptance spectrum. The solid line represents the absorptance with Ti considered and the circle markers represents the absorptance without Ti layer.

The geometry of nanostructures can be adjusted to tune the absorption spectrum. We scrutinize the variation of the antenna length, width, and shape. We already have an idea of

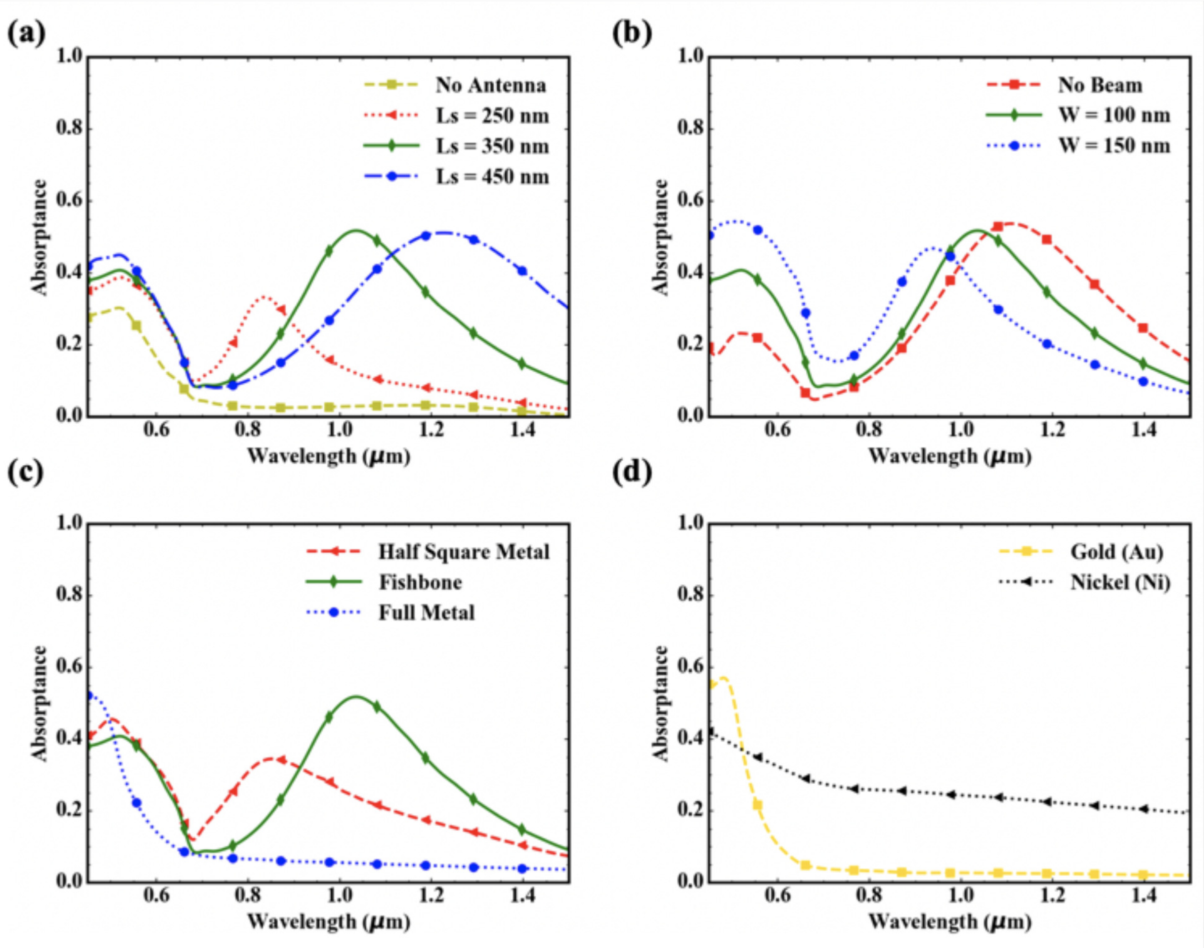

Figure 4.4: Absorptance adjustment by geometric tuning of suspended fishbone nanostructures - (a) variation of strip antenna length, L_s, without the antenna there is no absorption peak near 1 μm, (b) variation of beam width, W, (c) suspended metal shape, (d) absorption due to un-patterned suspended continuous gold and nickel film clarifying the high absorptance at lower wavelength in rest of the plots.

how the thickness variation for different materials influences the response from Figure 4.4. As the thickness is increased, the plasmonic coupling between the top and bottom surfaces of the nanowires decreases, so does the plasmonic absorption. The absorption peak also shows a blue shift. As the incident radiation has a polarization along the direction of the antenna, the antenna length can be tuned to tune the absorptance. The absorption peak expectedly shifts with the antenna length. This is shown in Figure 4.4(a). The purpose of the beam is to hold the strip antennas. However, the size of the beam impacts the plasmonic oscillation or resonance which is depicted in Figure 4.4(b). Wider beam reduces the absorption peak and causes blue shift of the absorption spectra. Finally, to peruse the high absorption coefficient at the lower wavelength (450-670 nm), we solve the absorptance for different shape of the suspended metal films. From our observation of Figure 4.4(c) and (d), we attribute that high absorption to the materials' inherited plasmonic property. However, the primary absorption peak around 1 μm is obviously because of the strip antennas as seen from Figure 4.4.

4.4 Sensitivity Analysis

We also study sensitivity of the proposed devices with different materials in combination with graphene coating. The sensitivity of the detector depends on the amount of evanescent coupling between the waveguide and nanostructure. We define a performance variable called evanescent intensity ratio (EIR), Figure 4.5(a), which is the ratio between the power of the leaked mode in the nanostructure to the total power. Higher EIR means more wave leaks and interacts with the metallic fishbone. The evanescent field and guided mode are shown in Figure 4.5(b).

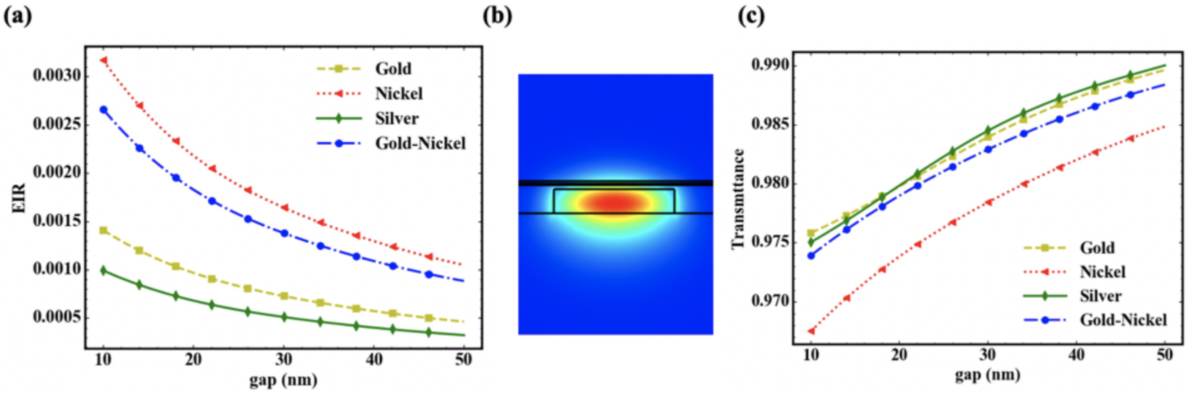

Figure 4.5: Sensitivity analysis – (a) evanescent intensity ratio (EIR) for different material nanostructure as a function of gap, (b) field view showing guided mode and field leakage to the nanowire region above the waveguide, (c) transmittance modulation as a function of the gap between waveguide and fishbone nanostructures for a single beam containing nanowires. Higher EIR causes larger change in the insertion loss of the waveguide.

We also report the variation of transmittance, Figure 4.5(c), through the waveguide as a function of distance (gap) between the waveguide top facet and a single-beam metallic fishbone. Higher EIR gives higher modulation of the transmission through the waveguide. So, it is beneficial to suspend the beams not too far above from the waveguide top facet.

The detector configured with 50 nm gold fishbone coated with graphene deflects 120 nm for a beam center-point temperature change of 82 K giving us a deflection of 1.46 nm/K for an incident radiation of 68 μW/μm^2 intensity. This is almost an order more deflection than out earlier report[28]. The deflection for 1 μW/μm^2 is calculated to be z_{vib}=1.76 nm/(μW/μm^2). Figure 4.5(c) further gives the idea of waveguide output modulation because of this vibration and it clearly depends on the rest gap between waveguide and nanostructure. We calculate over 0.1% change in waveguide output power for a change in radiation intensity of 1 μW/μm^2 with only a single beam of fishbone. Nickel and gold-nickel based nanowires show higher plasmonic interaction. We can also incorporate an array of the fishbone beams to get higher modulation strength at the waveguide output.

4.5 Noise Analysis

The plasmo-thermomechanical detector we designed is affected by three different noise sources – thermal, ambient, and mechanical. The thermal noise is dependent on the temperature and equivalent thermal conductivity of the device along the thermal path of interest. With graphene, we get a thermal noise power of $P_{th} = \sqrt{4k_B T^2 G}$= 4.74 pW/$\sqrt{Hz}$, where we consider thermal conductance G thorough air, gap and substrate, and primarily along the nanobeams, k_B is the Boltzmann constant, T is temperature. The contribution of graphene's large thermal conductivity to this noise is compensated by its tiny cross section. Ambient noise caused by radiative heat transfer to and from the device is negligible as the temperature build up is not too high. To analyze the mechanical noise, we calculate the equivalent Young's modulus of the nanowire to be E = 137 GPa. This results in 0.68 fm/$\sqrt{Hz}$ of non-resonant vibrational noise by using $z_{noise}=\sqrt{\frac{24k_BTl^3}{\pi^4 w\omega_o t^3 EQ}}$, where l, w, and t are the length, width, and thickness of the nanowire, Q is the quality factor obtained from simulation of the nanowire, ω_o is the resonant frequency. The power of vibrational noise thus appears to be $P_{vib}= \frac{z_{noise}}{z_{vib}}A$, where A is the 12.54×8.58 μm^2 detector footprint. P_{vib} is calculated to be 41.57 pW/$\sqrt{Hz}$ which is more than 7 times smaller than previously reported[28]. The overall device noise is thus dominated by the mechanical vibration of the device. However, the experimental result[28] and ambient condition suggest high system level noise coming from the air flow chamber that is used to keep the device free from dirt particles, optical table vibrations, and other microphonic sources. In the practical setting, the detector would be implemented in a vacuum sealed environment eliminating or reducing the possibility of contribution from different external noise sources.

4.6 Graphene's Effect on Thermal Relaxation Time

Graphene has a very large thermal conductivity [63] of over 5000 Wm^{-1}K^{-1}. Specially, the suspended graphene shows almost one order higher[68] thermal conductivity than the supported graphene. The large thermal conductivity allows graphene to quickly conduct heat from one position to another. So, graphene can work as a heat-spreader[69] that can enhance the extraction of heat out from the plasmonic hotspots. Thus, having a graphene layer on top of the fishbone nanowires proves to be even more useful since this quicker extraction of heat causes faster thermal relaxation. Absorbing the free-space radiation, the fishbone nanowires deform due to temperature gradient created along it. The heat dissipation mechanism is mostly conductive. The mechanical relaxation of nanowires upon the removal of the incident free-space radiation depends on how fast the heat can be dissipated. So, graphene allows the faster device operation when there is any time-varying radiation. The time-dependent study for nanowires of 50 nm thickness (for gold-nickel bimetallic nanowire, we consider 30 nm gold above 20 nm nickel) is shown in Figure 4.6. Comparing Figure 4.6(b) to (a), we observe a faster thermal oscillation resulting from a substantial reduction in the rising and falling time constants when graphene is incorporated in the nanowires. For gold and silver nanowires, thermal buildup from the absorptance enhancement (Figure 4.3(a) and (b)) by graphene dominates the thermal escape from the heat spreading property of graphene. The opposite happens for nickel and gold-nickel nanowires as they do not see significant enhancement in absorptance (Figure 4.3(c) and (d)). In Figure 4.6(c) and (d), we set the nanowire at an arbitrary but anticipated temperature gradient as an initial condition and then observe how the temperature profile along the beam varies with time. We clearly observe that for a given temperature gradient, the device coated with graphene cools down much faster than the one without, allowing faster operation of the detector.

To calculate the thermal time constant, we assume the convective and radiative heat transfer effects to be negligible in this system as their thermal resistances are more than 4 orders of magnitude higher than the thermal conduction resistance. For all nanowires considered in the analysis, the thermal time constants deduced separately from simulation and analytical calculation are observed to be in agreement. As an example, we report the thermal time constants of the gold-nickel nanowire with and without graphene calculated analytically and from simulation-obtained Figure 4.6(a) and (b). Our finite-element simulations show that the temperature distribution of the gold-nickel fishbone structure varies with a thermal time constant of 0.42 μs for rising edge and 0.45 μs for falling edge. Total temporal width in this case is 0.87 μs. If graphene is incorporated, the time constant becomes 0.13 μs for rising edge and 0.15 μs for falling edge which is three times less than the case without graphene. In this case, the total temporal width is 0.28 μs. Therefore, coating graphene sheet can boost the device thermal response speed by 3 times. The result from numerical analysis is shown in 4.6(c) and (d) showing the improvement in thermal dissipation speed. The conclusion from the numerical study aligns with our analytical results, in which a two-fold speed enhancement is derived based on the thermal time constant calculation for multilayer

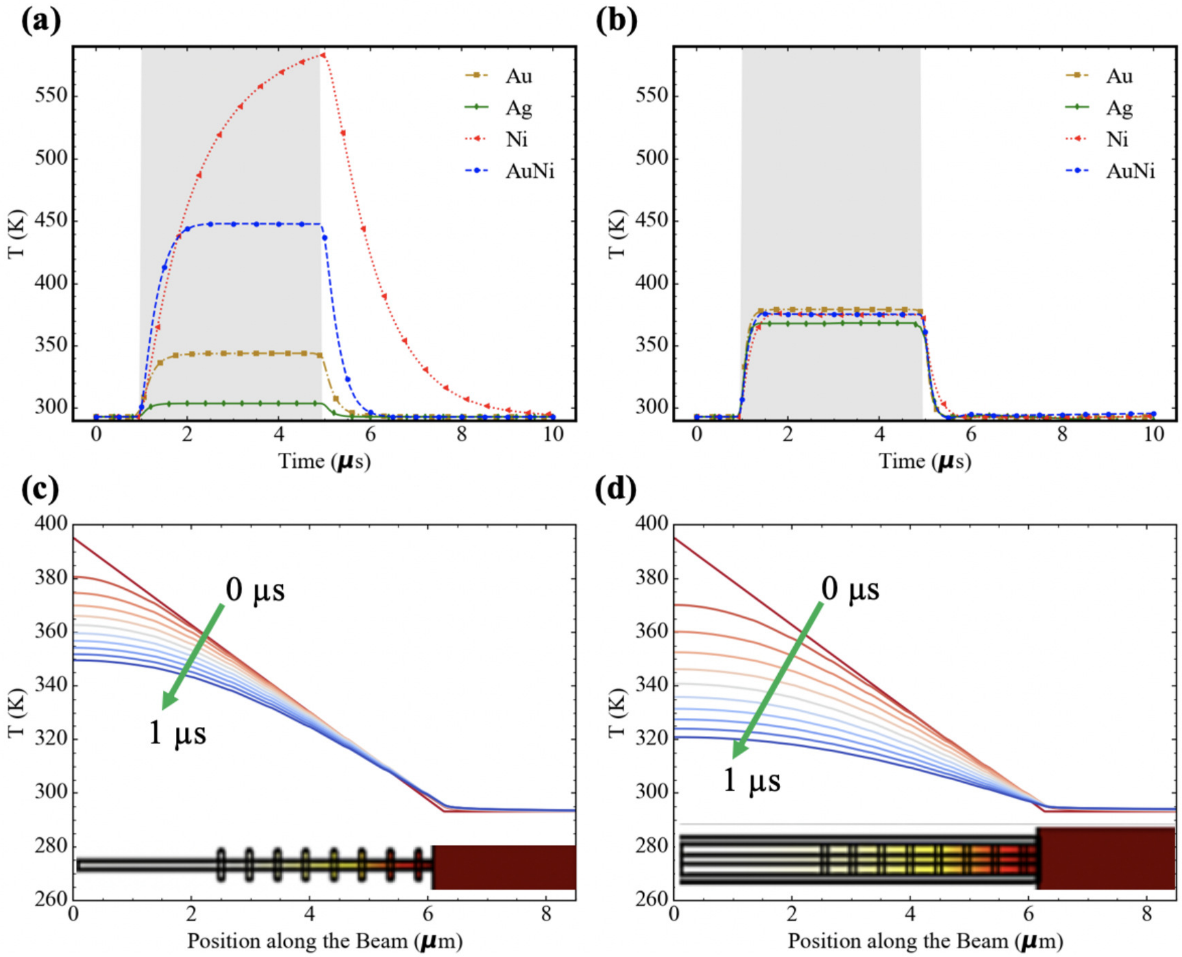

Figure 4.6: Time-dependent study of the IR detector - (a-b) temperature at the mid-point of different nanowires (a) without and (b) with graphene coating based on a given radiative pulse of 4 μs width. The shaded region shows the pulse duration., (c-d) spatial temperature profile along the Au-Ni beam (c) without and (d) with graphene for a given initial thermal distribution (0 μs). In both cases, the top view of the beam is placed as an inset, and the beam's geometric coordinates are aligned with the x-axis. With graphene, the profile cools down to a much lower temperature for a given time of 1 μs

.

thin films under periodic heating [70]. Based on thermal circuit analysis,

$$\tau = R \times C = \frac{L}{kA}\rho C_p V = \frac{L^2}{\alpha} \tag{4.2}$$

$$\alpha = \frac{\sum k_i h_i}{\sum \rho_i C_i h_i} \tag{4.3}$$

where R is the thermal resistance, C is the thermal capacitance, and α is the effective thermal diffusivity. Here, L is assigned to be 6.27 μm (half of the total length due to symmetry), i is material index (gold, nickel, graphene), ρ is material density, V is volume, h is thickness, C_p and C_i are specific heat. Gold and nickel have a bulk thermal conductivity [71] of 318 $\mathrm{Wm^{-1}K^{-1}}$ and 90.7 $\mathrm{Wm^{-1}K^{-1}}$, respectively. To capture more realistic thermal conductivities [72], we consider all the scattering mechanisms (thickness, boundary, and grain size) that result in $k_{Au} = 170\ \mathrm{Wm^{-1}K^{-1}}$ and $k_{Ni} = 60\ \mathrm{Wm^{-1}K^{-1}}$. The calculated diffusivities are $4 \times 10^{-5}\ \mathrm{m^2s^{-1}}$ and $7.3 \times 10^{-5}\ \mathrm{m^2s^{-1}}$ without and with graphene respectively resulting in 1 μs and 0.5 μs of time constant. The small difference between numerical and analytical calculation can be attributed to the fact that, in analytical calculation the change in cross-section along the beam is not taken into account. For the time-dependent thermal analysis, the ambient temperature is considered to be 20°C or 293.15 K. The higher thermal conductivity of graphene limits the maximum temperature build-up. However, graphene-enhanced absorptance and the large contrast between the thermal expansion coefficients of graphene ($-8 \times 10^{-6}\ \mathrm{K^{-1}}$) and the candidate metals ($13 - 18 \times 10^{-6}\ \mathrm{K^{-1}}$) allows for a large deflection in the graphene-coated nanowire resulting in higher sensitivity of the detector.

4.7 Mechanical Deflection Increment

As graphene has negative thermal expansion coefficient, coating graphene over metals will result in downward deflection of the nanowire beam when it absorbs radiation. So, suspension should be created far enough from the top facet of the waveguide in order to avoid collision.

We also numerically calculate the maximum von Mises stress of 40-130 MPa which is within the yield point of the materials in consideration. Therefore, we do not expect any significant plastic deformation of the nanowires. Figure 4.7(a) and (b) show the beam deformation for graphene on 50 nm thick gold (max. 120 nm downward) and 50 nm gold-nickel (max. 20 nm upward) nanowires respectively when the incident radiation of 68 μW/μm^2 intensity is at a wavelength that gives maximum absorptance. We see a six-fold beam deflection in graphene-coated beam that translates to increased sensitivity of the IR radiation detection.

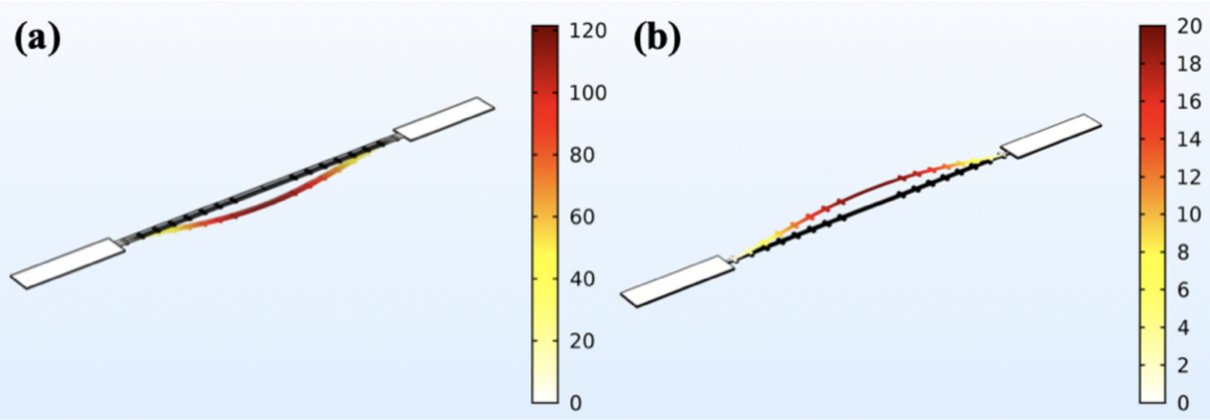

Figure 4.7: Nanowire deformation (nm) (a) with and (b) without graphene.

The higher defection causes larger modulation of the light through the waveguide. This results in higher sensitivity and modulation index of the detector, which enhances the detection sensitivity of the device.

4.8 Chapter Summary

The graphene-coated nanostructure is shown to be beneficial in manifold perspectives including the easy integration, enhanced sensitivity, and room temperature operation. For the IR detector we propose, we observe significant improvement in sensitivity in the form of absorptance increment, as well as in speed in the form of low thermal resistance heat dissipation path. We numerically and analytically calculated and compared the absorptance for graphene-metal nanowires and their time-constants of the thermal oscillation. In addition to its benefits, graphene is inexpensive and easy to fabricate. Besides graphene, other carbon-based materials like carbon nanotube (CNT) may also be considered for integration with metallic plasmonic nanostructures. Even polymers like PMMA, PDMS, SU-8 can be formed as a suspended nanowire system by methods like electrospinning over a trench waveguide to couple with external forces like acoustic wave or vibration which can be optically detected by the waveguide-nanowire interaction facilitating compact and efficient on-chip detection system.

Chapter 5

Bolometric Infrared Radiation Detector

5.1 Design

Proposed design has three main components: radiation absorber, VO_2 nanobeam, support structure with thermal isolation. Radiation absorber is the key component that determines the absorption efficiency, and it consists of single to multiple unit cells of plasmonic absorber. VO_2 nanobeam integrated with the plasmonic absorber functions as the transducing or sensing material. The support structure allows the suspension of the detector pixel and allow thermal isolation. The schematic of a single pixel with 9 absorber unit cells are depicted in Fig. 5.1(a). The unit cell schematic and cross-section including the dimensions are presented in Fig. 5.1(b). The number of unit cells present in a single pixel of the proposed infrared detector is scalable and depends on the absorbed power required for sufficient thermal buildup which, in turn, depends on the thermal isolation of the pixels. For our design, we have chosen the bolometer pixel with 3 × 3 unit cells as a balance of improvement between thermal resolution and spatial resolution. Larger number of unit cells will capture more radiation power that will result in increased thermal buildup ultimately resulting in a higher responsivity. However, larger pixel dimension will reduce the spatial resolution and degrade the thermal bandwidth of the detector. In this report, we only focus on the elements in a single pixel and select a conventional design for the pixel – suspension, support membrane, arms, etc. The optimization of the pixel structure, arm, suspension can be furthered to enhance thermal isolation for a better performance, and smaller pixel footprint.

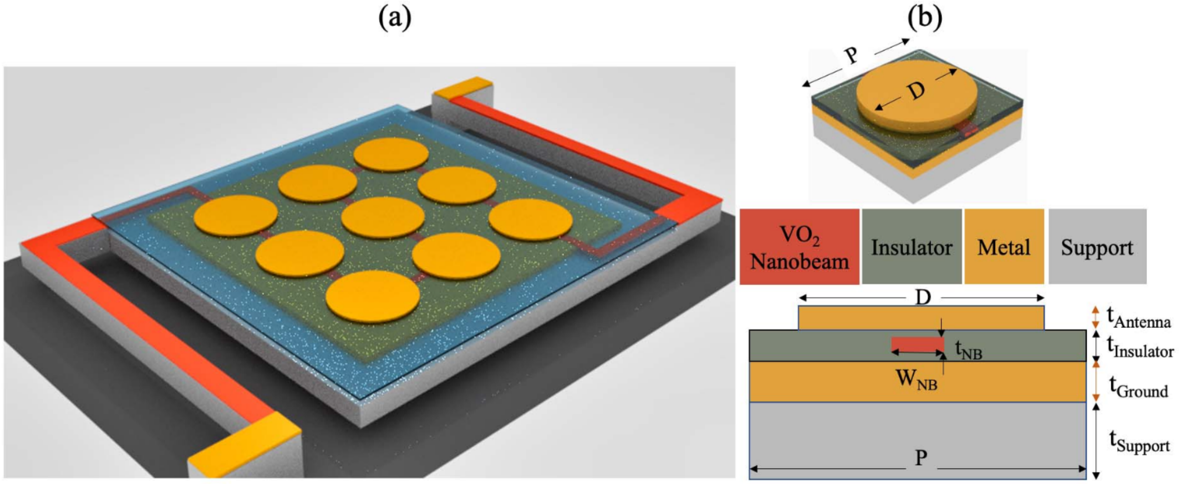

Figure 5.1: (a) Schematic of a single bolometer pixel showing the support structure, suspension arms, plasmonic array of 3 × 3-unit cells as selective radiation absorber. The translucent blue layer is the insulator where the nanobeam is buried. (b) Plasmonic absorber unit cell with the VO_2 nanobeam buried within the insulator of a metal-insulator-metal (MIM) type absorber and the cross-sectional view of the unit cell with material layer thicknesses. In our default design, to obtain maximum absorptance at 10 μm wavelength, antenna and ground layers are chosen to be gold (Au) with $t_{Antenna} = 20$ nm and $t_{Ground} = 50$ nm. Nanobeam transducing material is vanadium dioxide (VO_2) with $t_{NB} = 20$ nm and $W_{NB} = 100$ nm, insulator layer is magnesium fluoride (MgF_2) with $t_{Insulator} = 30$ nm, and support layer is silicon nitride (Si_3N_4) with $t_{Support} = 200$ nm. The default disk antenna diameter, $D = 2.6$ μm and unit cell period, $P = 3$ μm.

We choose metal-insulator-metal (MIM) type plasmonic absorber to efficiently absorb LWIR radiation from object. At lower wavelength, it behaves like a near-perfect absorber. Where most other plasmonic absorbers see significant decrease towards LWIR after scaling, a MIM type absorber demonstrates highly efficient absorption by a sub-wavelength feature that is critical for our application to reduce the pixel dimensions. The transducing VO_2 nanobeam is buried within the insulator. The plasmonic absorption-induced thermal increase locally affects the VO_2 nanobeam. Even though, silicon dioxide can be used as the insulator layer, it exhibits lossy behavior over 7 μm wavelength. We choose magnesium fluoride as the insulator for optimal design at LWIR. Finally, in our design, the use of nanobeam instead of a thin-film [73, 74, 75] benefits the design in two ways. First, the large length to cross-section ratio amplifies the change in the readout voltage $V(T) = I_{bias}\rho_{NB}(T)L_{NB}/A_{NB}$ producing high responsivity, where L_{NB} and A_{NB} is the length and cross-sectional area of the VO_2 nanobeam, ρ_{NB} is the temperature dependent resistivity of high-TCR VO_2, I_{bias} is the bias current, and 4 is the readout voltage. Second, since the bandwidth of thermal detectors are mainly determined by thermal mass and thermal conductance, the use of nanobeam instead of a film achieves a reduced pixel thermal mass thus an increase in the speed or bandwidth. Additionally, we propose to bias the device temperature at the phase transition point of VO_2 to utilize the high-TCR property of VO_2. At transition, the TCR can be as high as 200 K^{-1} [39, 40, 76] whereas other commonly used materials has a TCR below 3 K^{-1} [40]. However, due to hysteresis, the resistance-temperature fluctuation will result in micro-hysteresis [39, 40, 76], which is deterministic, and can be considered to calibrate the voltage readout. In following subsections, we will provide the details of individual components in design and performance point of view.

Sub-wavelength plasmonic features have spurred significant research interest and enabled novel applications such as radiation detection, spectroscopy, and sensing [28, 77, 7, 78]. Similarly, plasmonic absorbers [73, 74, 7, 79, 80] have the potential to enhance radiation absorption efficiency of thermal or infrared detectors that we are proposing while maintaining smaller pixel dimensions. Hence, these absorbers facilitate higher thermal buildup that is inversely proportional to the material volume and lead to a higher resistivity change of the transducing material. However, not all plasmonic absorbers are efficient over a wide range of wavelengths even after scaling the geometry. We choose metal-insulator-metal (MIM) type plasmonic structure that exhibits near perfect absorption [7] for short-wave infrared (SWIR), mid-wave infrared (MWIR) and over 55% absorptance at 10 μm wavelength or at long-wave infrared (LWIR). The schematic of the absorber in the unit cell is shown in Fig. 5.1(b). In the proposed MIM absorber, the metal layer is chosen to be gold and the insulator layer is chosen to be silicon dioxide (SiO_2) or magnesium fluoride (MgF_2). The top metal layer can be an array of circular or square patches in general. For optimized absorption at the 10 μm wavelength, we choose circular patch with a diameter of 2.6 μm which are placed periodically at a 3 μm pitch. Since SiO_2 becomes highly reflective between 8-12 μm (Restrahlen band) and loses its ideal insulating behavior, it is not usable as an insulator layer for this wavelength range. However, fluorides of calcium or magnesium offer insulating property over a wider wavelength range for LWIR applications. The key design parameters for the MIM absorber are – period (can be finite or infinite, latter for theoretical simplification of calculation and numerical analysis), top metal layer antenna diameter, insulator or spacer layer thickness and material (i.e., real and imaginary part of optical index), metal thicknesses at ground plane and antenna layer. The presence of the VO_2 nanobeam, in both - semiconducting and metallic states, has insignificant contribution to a change in the absorptance profile of MIM absorber. This is due to nanobeam's comparatively much smaller dimension than the wavelength and other features in the absorber. The reported absorption spectrums (obtained by optical simulation using COMSOL Multiphysics) in Fig. 5.2-5.4 present the effects of each of the design parameters by neglecting the insignificant variation caused by the presence of buried VO_2 nanobeam.

The resonance wavelength of the plasmonic antenna, or the peak absorption wavelength can be engineered by tailoring the antenna dimensions. Fig. 5.2 presents the absorption spectrum for different diameters of the circular gold (Au) antennas. However, depending on the fabrication process and required deposition temperature of VO_2, refractory metals like tungsten and platinum can also be used particularly for the ground metal plane. We have also investigated copper (Cu), silver (Ag), tungsten (W), and platinum (Pt) as the antenna

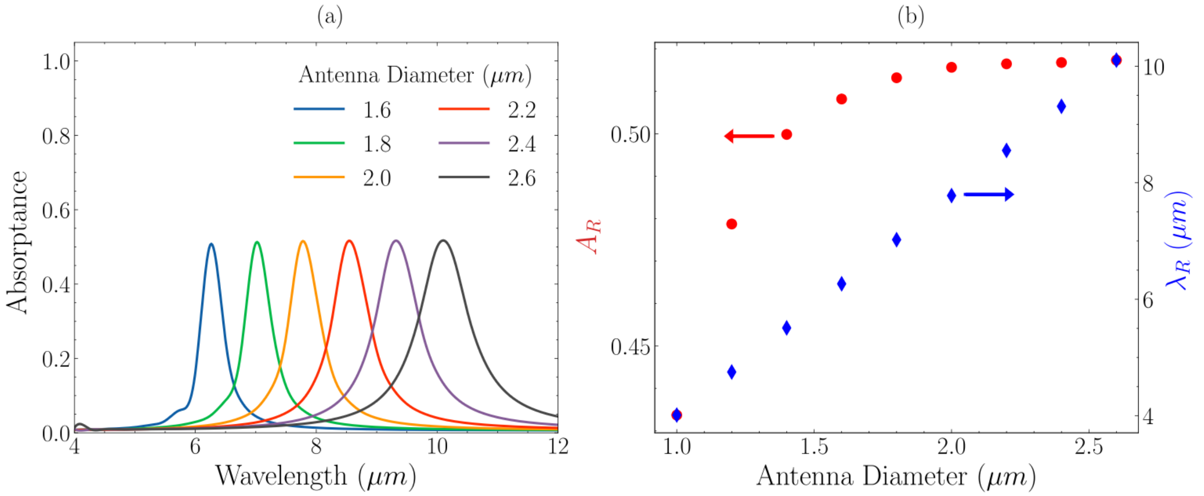

Figure 5.2: Effect of duty cycle or diameter variation when the period is 3 μm - (a) the absorption spectrum for varying antenna diameter showing tunability of peak absorption wavelength i.e., the range of object temperature, (b) effect of antenna diameter variation on the peak absorptance, A_R (left axis – red) and the resonant wavelength, λ_R (right axis – blue).

and ground metal plane. We report the results for gold as it has the most favorable optical properties at the targeted 10 μm wavelength. Fig. 5.2(b) presents the variations in peak absorption efficiency, A_R and resonance wavelength, λ_R for different antenna diameters as can be related with Fig. 5.2(a). The red markers present the value of resonant absorptance (left y-axis), and the blue markers present the value of resonant wavelength (right y-axis). As expected, the resonance wavelength is blue shifted with the decreasing antenna diameter [81]. We anticipate higher absorption efficiency at lower wavelengths. The nearly flat absorption efficiency in Fig. 5.2(b) is mainly due to decreasing fill factor since we kept the period same at 3 μm for all these calculations.

A thicker top metal patch improves absorption because of stronger plasmonic interaction as shown in Fig. 5.3. However, it also adds to thermal mass which is unexpected. However, we see over 55% absorptance for only a 20 nm thick gold layer as the top metal. The effect of the bottom or ground metal layer thickness is insignificant as reported in [82]. A thin bottom layer is desired for lower thermal mass, higher bandwidth as well as less heat spreading by

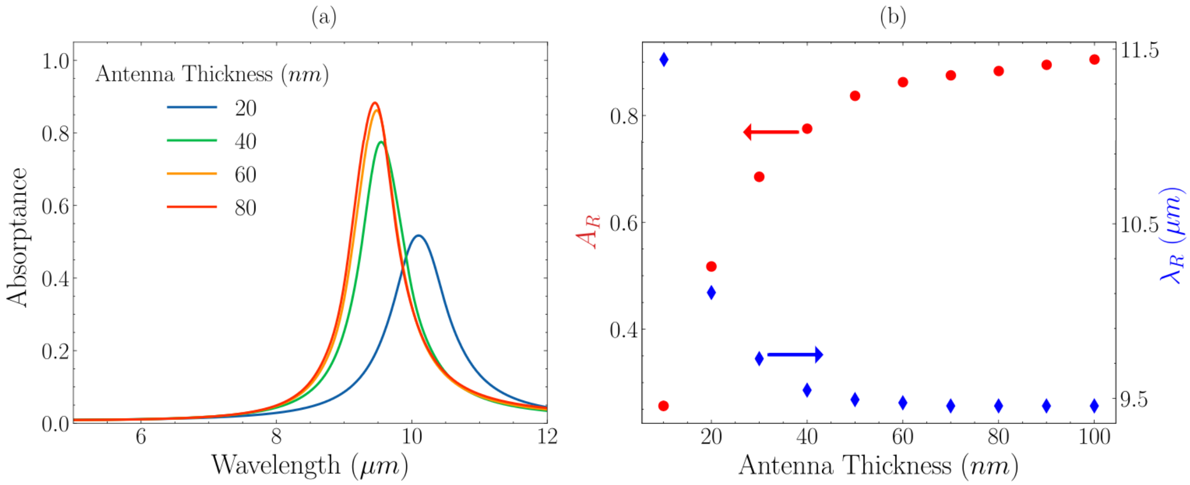

Figure 5.3: Effect of antenna thickness with unit cell period fixed at 3 μm and antenna diameter fixed at 2.6 μm – (a) absorptance profile vs wavelength for thickness of the antenna or top metal layer, (b) absorptance, A_R (left axis – red) and wavelength, λ_R (right axis – blue) at resonance for a range of antenna thickness.

the metal layer. Better thermal isolation and further reduction of heat spreading can be obtained with a discontinuous ground metal. However, it adds to the complexity and steps in the fabrication process. So, we focus to investigate the architecture with a continuous ground film across all unit cells in a single pixel.

In Fig. 5.4, we present the peak absorptance and related wavelength with respect to variation in other design parameters - period of absorber unit cell, insulator material properties, and thickness. The changes in the period of the arrayed structure only impacts the absorptance efficiency, not the peak absorbing wavelength. From Fig. 5.4(a), we observe larger absorptance for higher fill factor, $F = \frac{AntennaDiameter}{Period}$. The peak absorptance shows weak exponential decrease with the increase of unit cell period.

The thickness and the material properties i.e., the refractive index of the insulator impact both – the resonant absorption wavelength as well as peak absorptance value. The effect of the insulator layer thickness is shown in Fig. 5.4(b). Thicker insulator is observed to allow higher absorptance. However, it adds to thermal mass of the pixel and can potentially degrade the overall performance of the detector. The relationship between peak absorptance

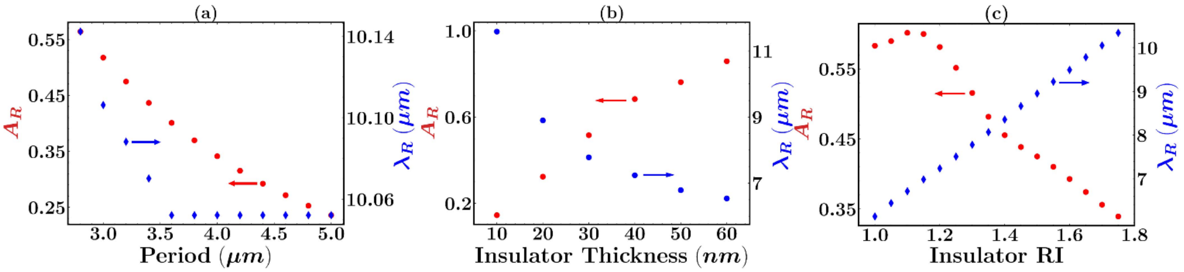

Figure 5.4: Peak absorptance, A_R (left axis – red) and the wavelength of peak absorptance, λ_R (right axis – blue) with respect to (a) period of absorber unit cell, (b) insulator thickness, and (c) insulator refractive index (RI) keeping all the other design parameters at default value.

wavelength and spacer refractive index is found to be linear (with slight variation due to numerical error) as also suggested by [74]. We also present the effect of the refractive index of the insulator layer material in Fig. 5.4(c) which shows that a lower range of refractive index allows higher peak absorptance and the resonant wavelength scales linearly with the insulator RI.

To enhance the responsivity, the device transducing material VO_2 nanobeam needs to operate at the transition point to have the highest TCR or sensitivity to temperature and radiation. We propose to operate the device at the transition point using a Peltier or thermo-electric heater to heat VO_2 nanobeam to the transition mid-point. Due to hysteresis of the phase transition in VO_2, the resistivity vs temperature will trace micro-hysteresis loops [40] for a small radiation fluctuation. However, the nature of the micro-hysteresis is expected to be deterministic as the material does not undergo any irreversible change.

A bolometer pixel is shown in Fig. 5.1(a). We choose a standard suspended pixel shape with two arms whose implementation can be further optimized which is beyond the scope of this work. We propose an arrangement of 3 × 3 array of absorber unit cells in a pixel with the VO_2 nanobeam spiral-traced below the absorbers and buried within the insulator layer. The nanobeam is 20 nm thick and 100 nm wide. This is an optimization between thermal and spatial resolution as mentioned earlier. The number of unit cell is chosen for sufficient radiation absorption to obtain high responsivity at the same time reducing the pixel pitch compared to state-of- the-art reports [83, 84, 85, 86, 87, 88].

The radiation emitted from the object, after being focused by lenses on the pixels, gets absorbed by the plasmonic absorber elements in a pixel. Local heating and temperature buildup occur due to the radiation absorption. The local temperature buildup causes the local portion of the nanobeam to undergo changes in resistivity depending on the temperature level. This change in resistivity carries the information of the radiation emitted from the object. The change is read out from properly biased individual pixels to finally create a thermal map of the object in focus.

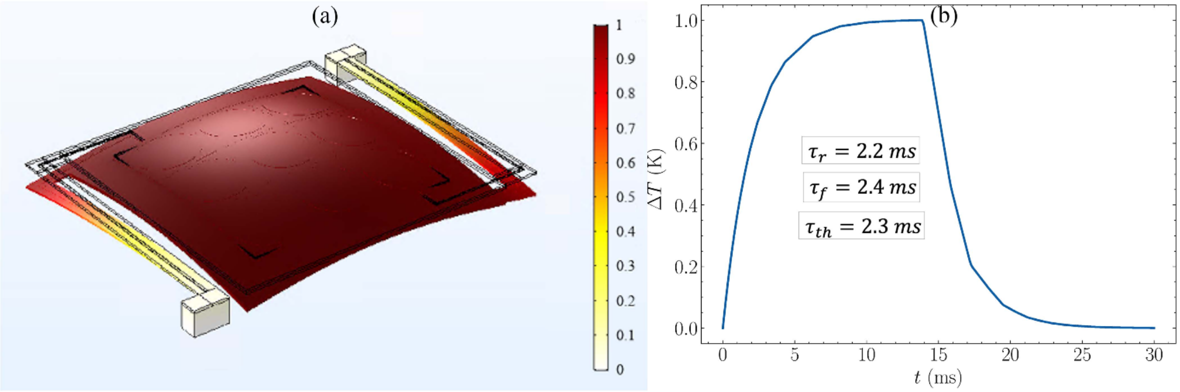

Figure 5.5: (a) Thermal analysis of bolometer showing the temperature map of the bolometer for a 30 nW of heat flux incidence normal from the top, (b) Transient analysis of the thermal fluctuation of the detector in response to pulsed heat flux incidence. The thermal time constants for rising (τ_R) and falling (τ_F) edge are also calculated from this graph. The average thermal time constant, τ_{th} is calculated by averaging the rising and falling edge time constants.

5.2 Thermal and Mechanical Analysis

Thermal conductance, G_{th} and heat capacity, C_{th} are the two key parameters for a bolometer design and performance. Lower thermal conductance allows larger thermal buildup that results in higher sensitivity infrared detection. This can be achieved by eliminating the heat escape mechanisms. Thus, the ideal limit of performance is the radiative limit. The heat escape can be reduced by implementing structure that demote heat escape by conductance, for example, using suspended membrane to reduce vertical heat transfer and using long, thin and narrow arms to reduce lateral heat transfer, and so on. However, the thermal time constant of the detector is inversely proportional to the thermal conductance and directly proportional to the thermal resistance R_{th}: $\tau_{th} = C_{th}/G_{th} = C_{th}R_{th}$. Therefore, there is a trade-off between the detection bandwidth and the heat capacity. The time constant directly defines the upper limit of the refresh rate in thermal cameras.

To obtain the thermal conductance of the proposed detector pixel, we calculate the amount of heat flux needed to raise the average temperature of the detector pixel by 1 K. We find the heat flux to be 30 nW per pixel area, resulting in a thermal conductance, $G_{th} = 3\times10^{-8}W/K$. The thermal profile obtained using COMSOL Multiphysics is shown in Fig. 5.5(a). Such low value of thermal conductance combined with high TCR of the VO_2 nanobeam allows the detection of very low radiation power emitted from the object of interest. This high sensitivity makes it possible even to distinguish tiny temperature differences or a low $NETD$ discussed on a later section. The displacement of the pixel in the figure is an exaggerated representation of the thermal response (in this case, only expansion) of the materials. We calculate the heat capacity to be $8.02 \times 10^{-11}J/K$ and the corresponding thermal time constant of 2.67 ms of the detector according to -

$$C_{th} = \sum_{\text{layers}} C_i \rho_i t_i A_d \tag{5.1}$$

where, C indicates heat capacity, ρ is density, t is the thickness, A_d is the area of each material layer in a pixel. We conduct numerical transient analysis to extract the thermal time constant of the detector. A square pulsed radiation of 30 nW and 30 ms period is considered to be incident on the detector pixel and the corresponding temperature buildup is calculated numerically. The simulated time response is shown in Fig. 5.5(b). From the figure, we observe an average thermal time constant of 2.3 ms which is in close agreement with the previously calculated value. Due to smaller pixel dimension and reduced thermal mass in our design, the time constant is smaller than recent reports [83, 85, 86, 88]. The thermal time constant defines the minimum response time or maximum bandwidth of the detector. The thermal bandwidth of the detector is calculated to be 108 Hz from the thermal time constant using $BW = \frac{1}{4\tau_{th}}$ [89]. The electrical bandwidth is defined by the integration time, and the final output bandwidth depends on the frame rate.

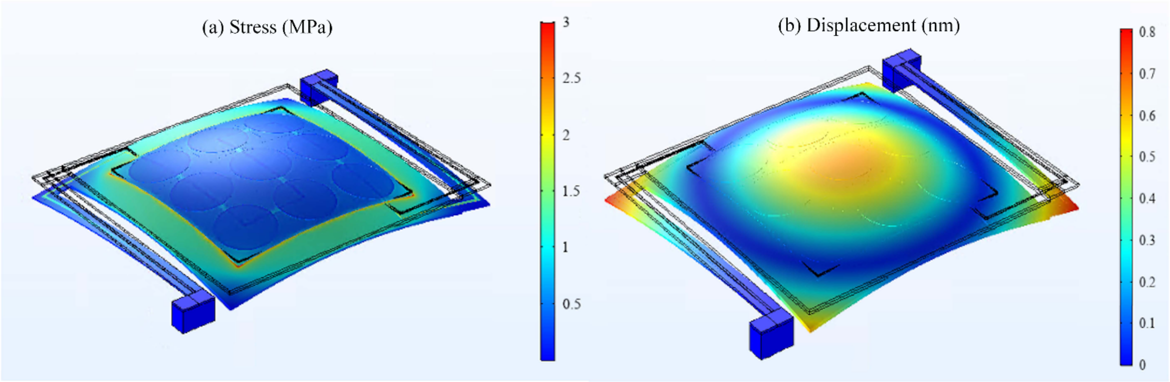

Figure 5.6: (a) Von Mises stress map of the detector showing critical regions of stress and (b) Displacement due to 30 nW of radiation incidence considering the thermal expansion coefficients of the materials in the bolometric detector.

The bolometer detector needs to be suspended to reduce conductive heat escape to the substrate and surrounding. We consider a 200 nm thick silicon nitride layer as the support as this material is commonly used for micro electro-mechanical system (MEMS) structures. The low thermal conductivity of silicon nitride allows the device to have low thermal conductance to ultimately obtain a high responsivity. Fig. 5.6 shows the numerical results for expected stress and displacement of the detector structure. The stress along the detector structure is below 3 MPa which is 2 to 3 orders lower than reported endurance limit of support nitride membrane [90, 91]. Hence, the structure will allow cyclic stress developed upon radiation fluctuations. Also, the displacement for thermal expansion of the materials is below 1 nm. Thus, the detector is mechanically stable and is expected to withstand periodic expansion and compression due to radiation exposure.

5.3 Performance

To assess the performance of the bolometer we look at its responsivity and the noise equivalent power. The responsivity can be determined from equation 3.6 where $K = I_{bias} \times R_{NB} \times TCR$, where I_{bias} is the bias current, which is considered to be 1 μA (to limit the Joule heating induced temperature change of the detector) through the analysis if not otherwise mentioned, R_{NB} is the nanobeam resistance, TCR is the temperature coefficient of resistance of the VO_2 nanobeam, ε is the emissivity of absorbing antennas, R_{th} is the thermal resistance, ω is the angular frequency, τ_{th} is the thermal time constant of the detector pixel. The responsivity of the detector is thus inversely proportional to the nanobeam cross-sectional area and proportional to the length. Hence, a detector with transducing nanobeams instead of a film thus facilitates higher responsivity. As an example, a nanobeam incorporated in our proposed 12 μm × 12 μm detector pixel will allow 270× responsivity compared to a film with the same thickness as the nanobeam (but different length to cross-sectional ratio) incorporated in the same pixel. The expected responsivity of the detector vs frequency is shown in Fig. 5.7(a). At a frequency of 100 Hz, we expect a responsivity of over 700 kV/W. As stated before, we are biasing the VO_2 nanobeam at the transition temperature. The responsivity is proportional to the TCR of the transducing material which in turn depend on the device bias temperature. The TCR of VO_2 can reduce by two orders of magnitude from on-transition to off-transition temperature [76]. As a result, the responsivity can degrade by up to two orders of magnitude if it is biased far from the transition temperature.

The radiative limit of responsivity, which is the theoretical performance limit of the device is shown in Fig. 5.7(b). Also, the noise equivalent power (NEP), defined as the signal level that produces a signal-to-noise ratio (SNR) of 1, is also presented. The NEP calculated

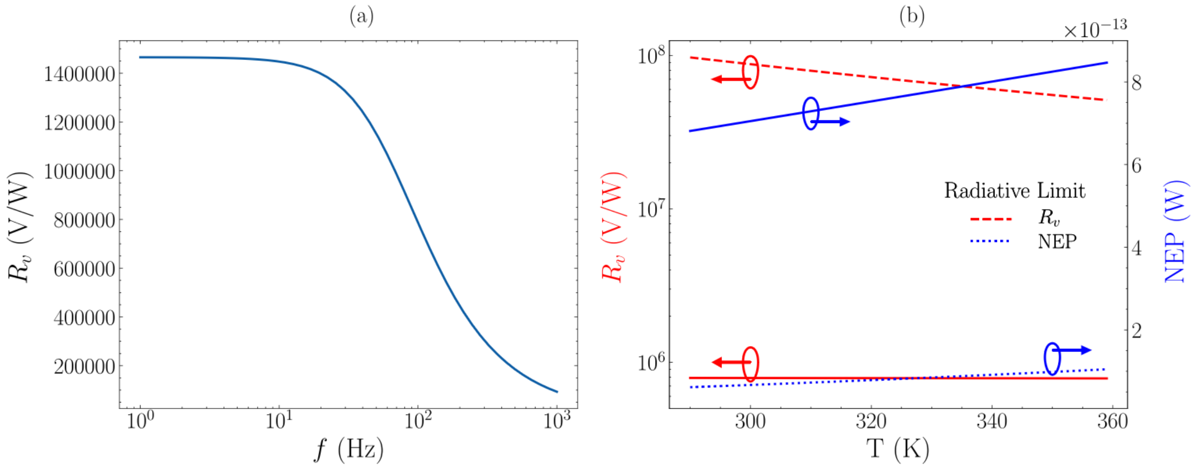

Figure 5.7: (a) Responsivity with respect to frequency at 341 K temperature (device bias temperature to be at VO_2 transition). We estimate over 700 kV/W of responsivity at 100 Hz. (b) Responsivity (left y-axis, red) and NEP (right y-axis, blue) at 100 Hz along with their theoretical (radiative) limit with respect to device temperature.

for the proposed detector design is very close to the radiative limit. The gap between the proposed detector and theoretical limit comes from the difference in radiative-only thermal conductance and detector thermal conductance.

The detectivity and noise equivalent temperature difference ($NETD$) are also important performance metrics for an infrared thermal detector. The detectivity is defined as:

$$D^* = \frac{\sqrt{(A_d \Delta f)}}{NEP} = \frac{K\epsilon R_{th}\sqrt{A_d}}{\sqrt{(1+\omega^2\tau_{th}^2)\left(\frac{4kT^2K^2R_{th}}{1+\omega\tau_{th}^2} + 4kTR\right)}} \tag{5.2}$$

where A_d is the active detector area. The obtained detectivity for the detector we propose is shown in Fig. 5.8. It is presented with respect to frequency, bias temperature, and thermal conductance. From Fig. 5.8(a), it is observed that device temperature has insignificant impact on the detectivity. This is due to large coefficient, K and large thermal resistance, R_{th} as they appear in equation 5. The detectivity with respect to the thermal conductance is presented in Fig. 5.8(b) as a reference to theoretical limit when G_{th} reaches its minimum possible value which is the case when only radiative thermal conductance is considered.

Thermal conductance in our design of bolometer pixel is 30 nW. As implied in Fig. 5.8(b), with improved design of the pixel arm, suspension, vacuum, and thermal isolation, detectivity can be improved further. Detectivity for 30 Hz and 60 Hz frequency is presented as they are two common refresh-rate currently used for visible wavelength and infrared cameras. The $NETD$, on the other hand, is a measure of thermal resolution. It defines the minimum temperature difference that is distinguishable by the detector and is expresses as [55]

$$NETD = 4\left(\frac{F}{\#}\right)^2 \sqrt{\frac{\Delta f}{A_d}} \left[\int_{\lambda_a}^{\lambda_b} \frac{\partial M(\lambda)}{\partial T} D^*(\lambda) d\lambda\right]^{-1} \tag{5.3}$$

where, $\frac{F}{\#}$ is the aperture F-number, M is radiant exitance, λ is wavelength. For a bandwidth, Δf of 100 Hz and $\frac{F}{\#}$ of 1, integral wavelength limits of 8 to 10 μm, we obtain an $NETD$ of 3.67 mK which is almost an order lower than the state-of-the-art detectors [83, 84, 85, 87, 88, 92] implemented in a smaller pixel.

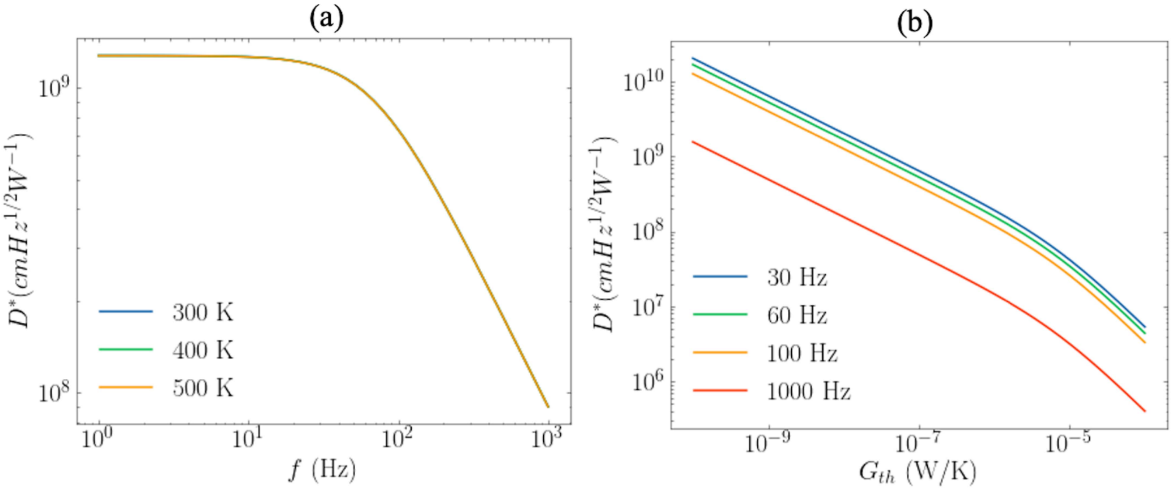

Figure 5.8: Detectivity with respect to (a)frequency at $G_{th} = 30$ nW at different temperature level, and (b) thermal conductance of the bolometer at $T = 341$ K showing the performance limit in terms of detectivity.

We compare the proposed detector performance with some recent works and state-of-the-art bolometric uncooled detector. Our design is estimated to have a responsivity of over 700 kV/W at lower frequency which is a significant improvement over the recently reported

Figure of Merit	This Work	[83]	[84]	[85]	[86]	[87]	[88]
$D^* \left(\mathrm{cmHz}^{1/2}\ \mathrm{W}^{-1}\right)$	1.2×10^9	5.4×10^8	NR	NR	1.0×10^7	NR	2.2×10^8
R_v(V/W)	$> 7 \times 10^5$	5×10^4	NR	NR	1×10^4	NR	5×10^5
τ_{th}(ms)	2.3	5.3	NR	5.9	< 10	NR	4.5
Area (μm × μm)	12 × 12	40 × 40	17 × 17	17 × 17	35 × 35	35 × 35	17 × 17
G_{th}(nW/K)	30	NR	NR	40	700	NR	62
$NETD$ (mK)	3.67	NR	35	NR	NR	71	NR
NEP (pW)	1	NR	NR	NR	NR	NR	100

Table 5.1: Comparison to other recent works (NR = Not Reported)

detectors [83, 84, 85, 87, 88]. The recently demonstrated detector pixel size is 17 μm × 17 μm [84, 85, 88]. Our design requires the pixel size to be 12 μm × 12 μm while at the same time providing improved performance in terms of detectivity, responsivity, $NETD$. The NEP is estimated to be very close to the theoretical limit. In Table 5.1, we show the summary of the comparison (NR stands for not reported). It is observed that, our proposed design shows improvement in every possible angle even where it is very challenging due to the design dilemma between different parameters.

We acknowledge that the properties of VO_2 is dependent on fabrication process especially temperature, substrate, strain, and geometry [93, 94, 95, 96, 97, 98]. In addition, VO_2 nanostructure (nanowire and nanobeam) resistivity along with its relationship with respect to temperature depends on its geometry and can differ from bulk and thin-film properties by up to an order of magnitude [93, 94, 95, 97]. The resistivity impacts device responsivity and noise performance. The final design, particularly the nanobeam geometry needs to be optimized by taking into consideration the variations in fabrication process. Most studies [93, 97, 98, 99, 100] on VO_2 nanostructures focus on the mechanically transferred VO_2 nanowires and nanobeams after being synthesized using vapor transport method. However, random growth and subsequent transfer of VO_2 nanostructure is not suitable for our proposed design of bolometer pixel as the nanobeam traces integrated with the plasmonic absorbers need to be physically and electrically continuous and aligned with absorbers and electrical contacts. On the other hand, the use of lift-off technique for patterning the nanobeam traces is not suitable due to high deposition temperature of VO_2 films. Therefore, dry etching [101] of the sputtered VO_2 film to pattern the nanobeam is suggested.

5.4 Noise Analysis

As discussed in earlier chapters, the major sources of noise in a bolometer detector are Johnson or resistive noise (V_j), thermal fluctuation noise (V_{th}), flicker noise ($V_{\frac{1}{f}}$), and background noise (V_b). Johnson noise can be estimated from equation 3.9 where R can be approximated to be the nanobeam resistance considering the insulator layer to have much higher resistance, and Δf is the bandwidth. The major component of the resistance is the VO_2 nanobeam itself. By biasing the device at the transition temperature of VO_2, the resistivity of the nanobeam VO_2 can be reduced by two orders of magnitude compared to its room-temperature semiconductor phase resistivity. This results in decrease of the Johnson noise and ultimately compensate for the noise development due to increased device temperature. Thus, the overall Johnson noise depends on the bandwidth, operating temperature, and the resistance of the device.

The second noise source or thermal fluctuation noise can be found using equation 3.10. For the proposed design parameters, we observe this noise to be in the level of tens of micro-volts for a given device temperature of 341 K and at a frequency of 100 Hz.

The third type of noise or background noise is calculated using equation 3.11 to be in the order of 10^{-11} V over the frequency and bias temperature range of interest, this type of noise has insignificant contribution to the overall noise and thus can be neglected for the proposed detector.

All the noise components and their trend with respect to frequency and device temperature

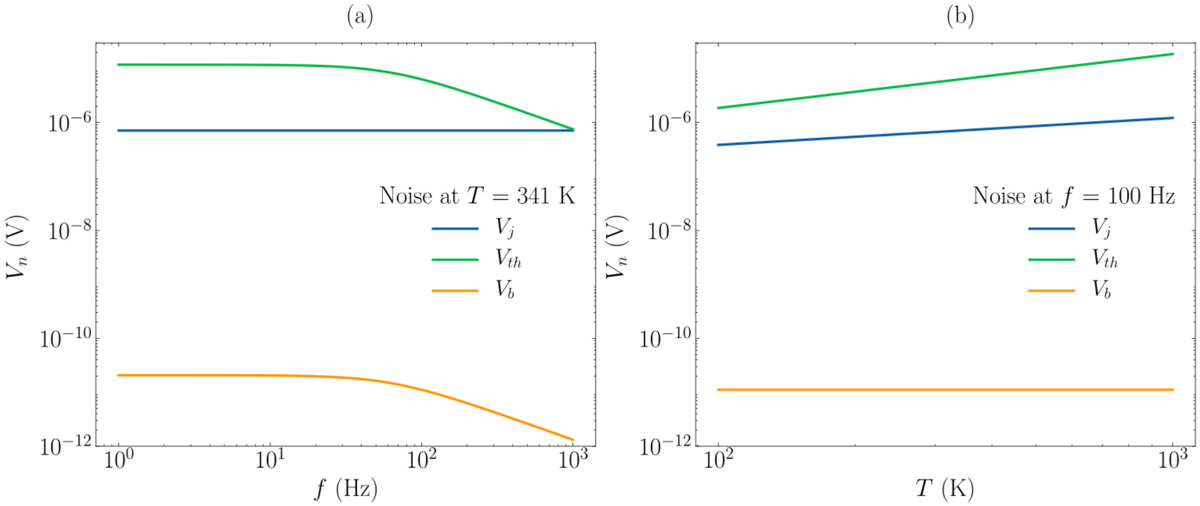

Figure 5.9: All noise sources with respect to (a) frequency at bolometer temperature of 341 K and (b) bolometer temperature at a frequency of 100 Hz.

is presented in Fig. 5.9. Putting all the different noises together, thermal fluctuation noise is observed to be dominant. However, since the flicker noise is highly process and material dependent, we ignore its contribution [55]. Based on actual device fabrication parameters this type of noise should be added for completeness.

5.5 Chapter Summary

In this chapter, we discuss a novel LWIR detector architecture with plasmonic absorber and VO_2 nanobeam integrated. The plasmonic absorber allows efficient and selective radiation detection from the radiating object. The design of the absorber can be scaled to tune the wavelength or temperature band of interest. Additionally, the sub-wavelength plasmonic features allow the detection of wavelength by a detector with a much smaller form factor. The use of VO_2 nanobeam, instead of a simple VO_2 film, amplifies the slope of the temperature dependent resistance due to the large ratio between length to cross-sectional area of the nanobeam allowing high responsivity. The proposed design and estimated performance are desired for mission critical applications where high sensitivity, high bandwidth, and noise immunity come as strict requirements such as thermal and medical imaging, night vision, detection and tracking, etc. We present the numerical analysis, noise analysis, and figure of merits of the proposed detector design. The structural, thermal and transient analysis of the bolometer are discussed. Whereas conventional approach trades off performance with active detector area; we observe significantly improved detectivity, $NETD$, responsivity for a detector of smaller form-factor. The design allows improvement in spatial resolution as well as thermal responsivity. We obtain a responsivity of over 700 kV/W at 100 Hz for only a 12 μm × 12 μm pixel size. The noise equivalent temperature difference for the proposed design is calculated to be as low as 3.67 mK, almost an order lower than detectors reported with larger pixel dimension.

Chapter 6

Bolometric Terahertz Radiation Detector

6.1 Design

The proposed THz bolometric sensor consists of a 2D arrangement of many bolometer pixels depending on the expected active area of the sensor, the specification of lenses, and the target field of view. One such bolometric pixel containing MIM absorbers and transducer VO_2 beams is shown in Fig. 6.1(a). The three-dimensional schematic shows how the pixel is suspended with four anchored connections to the substrate to allow proper thermal isolation and structural support. In addition, the entire detector is considered in a vacuum packaging to reduce heat flow by convection. Fig. 6.1(b) shows the top-view of a single pixel, and Fig. 6.1(c) illustrates the cross-sectional schematic, dimensions as well as material selections used in a pixel. The active detector area of each pixel is suspended and supported by the silicon nitride layer with four arms only making contact to the substrate at the pads (four rectangular features connecting the arms) that work as support anchors as well as readout access points. Such suspended structure can be achieved by etching the sacrificial layer underneath. By creating suspension, the active area of the detector is thus ensured to have reduced direct thermal contact with the substrate to promote thermal isolation and thus detector sensitivity.

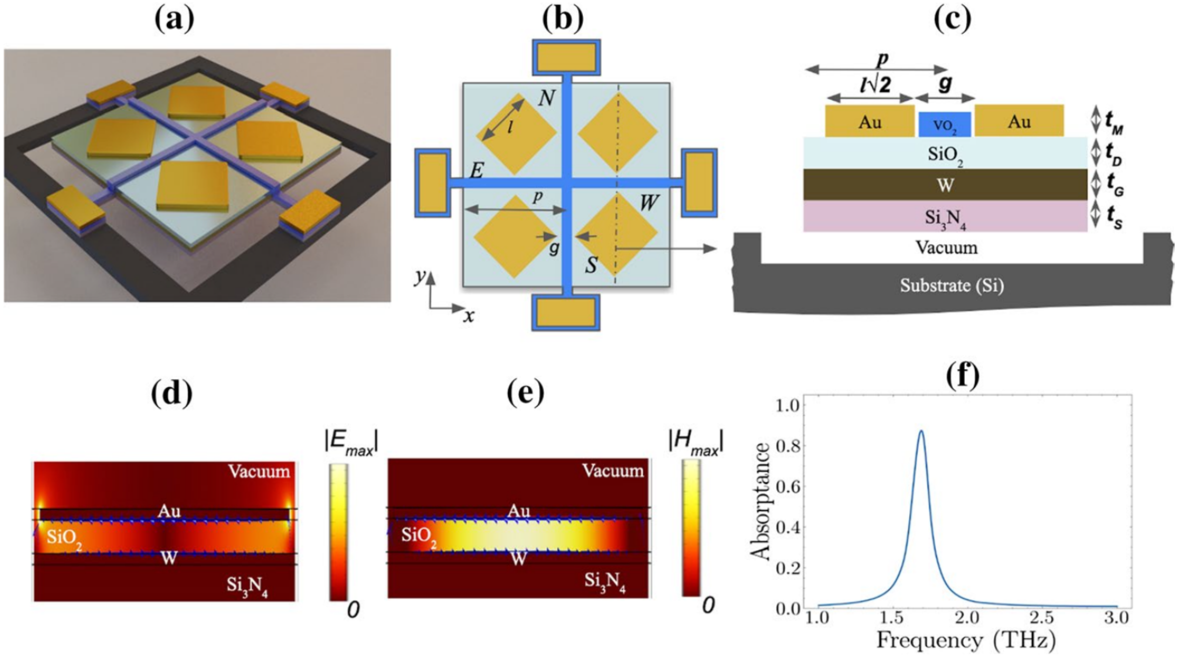

Figure 6.1: (a) Three-dimensional schematic of the proposed THz bolometer pixel, (b) Top-view schematic (not to scale) of proposed THz bolometric sensor (single pixel). The four gold (Au) patches along with the insulator and metal layer underneath construct the Metal–Insulator-Metal (MIM) absorber. The transducer has four arms (named N, W, S, and E for future references) positioned along the gaps of metal patches and connected to four terminal pads for electronic readout, (c) cross-sectional view (not to scale) and material selection for the default design. The default film thicknesses are chosen as $t_M = 0.5$ μm, $t_D = 1.5$ μm, $t_G = 1$ μm, $t_S = 0.3$ μm, and the side of square patches, $l = 40$ μm, gap, $g = 2$ μm, (d) electric field profile of absorber unit cell at resonance showing concentrated field at the sides of the gold patches; arrows point to the direction of the electric displacement field vector; $|E_{max}|$ is the magnitude of maximum electric field, (e) magnetic field distribution showing generation of strong magnetic field at the center of the absorber cell at resonance in accordance with the contra-directional electric displacement fields along the top gold patch and the tungsten ground plane; arrows represent the displacement field vector; $|H_{max}|$ is the magnitude of maximum magnetic field, (f) calculated absorptance profile showing resonant absorption at 1.7 THz achieved by the absorber with default design parameters.

A two-dimensional array of metal square patches (in the illustrated design it is chosen to be gold) of length l are placed diagonally to construct the top metal layer of the 2D MIM absorber which, in our design, is shown to selectively absorb narrow band radiation around 1.7 THz. We choose four unit cells of absorber in a pixel to keep balance between the total absorbed power (scales in proportion to pixel size) and the pixel density. The ground layer of the MIM absorber is a thin metal film, preferably a refractory metal such as tungsten (W) or tantalum (Ta) that are highly resistant to heat in order to withstand the high deposition temperature of subsequent VO_2 layer. We investigate multiple suitable materials for bolometer application. In the design discussed here, we choose tungsten (W) as the ground layer. The insulator layer can be a lossless dielectric material at the wavelength range of interest such as silicon dioxide and polyimide near 1.7 THz. The transducer four arms in our design can be deposited on the insulator layer (Fig. 6.1(c) or buried within (this variant is not shown here, offers better protection from ambient condition with decreased sensitivity). The arms connect to four terminal pads and can be probed individually by gated readout. They are named (N, W, S, and E) based on their location for future references. The use of transducer beam allows the measurement of localized field confinement and subsequent heating which is polarization dependent thus indicating polarization of the incident radiation.

We use three-dimensional (3D) finite-element method (FEM) by COMSOL Multiphysics to calculate the absorption profile of the MIM resonant absorber. In such absorbers, localized surface plasmon polaritons (LSPPs) are generated to achieve high absorption efficiency by a small footprint absorber area. Fig. 6.1(d), (e) illustrates the electric and magnetic field distributions of an absorber unit cell at resonance upon normal incidence of a plane wave with E_x polarization. The electromagnetic fields are calculated by 3D FEM on COMSOL Multiphysics platform. Fig. 6.1(d) shows strong electric dipole resonance from charge accumulations at the sides of gold patches which couple to their image charges in the tungsten ground plane. The contra-directional electric displacement vectors represented by the arrows in both figures along the gold patch and the tungsten film generate a significant magnetic response denoted by the surface colormap in Fig. 6.1(e). The strong absorption is thus induced by the excitation of localized magnetic and electric dipole resonances. Such phenomenon adds to the design flexibility based on geometric parameters rather than the material properties. In the design of MIM absorber with periodic 2D metal patches, the patches can be squares, circles, or crosses, etc. Each patch acts as a single isolated resonator, where the resonance is supported by the unit cell MIM absorber structure. The periodicity or array structure has less impact on the absorption profile. Therefore, we can use small number of unit cells to keep the pixel footprint as small as possible. In the demonstrated design, the 2D arrangement of 2 by 2 (or quad) unit cells is used to construct the absorber in a single pixel. We can utilize commonly used metals such as, gold (Au), aluminum (Al), silver (Ag) to generate surface plasmon polaritons (SPPs). The insulator layer between the two metal layers needs to be lossless in the frequency band of interest. As such, polyimide or silicon dioxide can be used. Fig. 6.1(f) illustrates the absorption profile we obtain by using $l = 40\ \mu$m square gold patches and silicon dioxide as dielectric. Theoretical analysis provided here uses previously reported frequency dependent material properties given for gold [102], polyimide [103], silica [104], and VO_2 [105]. A resonant absorption by the MIM absorber with over 85% efficiency is observed to take place at a frequency of 1.7 THz. The design can be modified to resonantly absorb radiation at other THz frequency ranges by choosing appropriate materials or by tuning the design parameters such as geometry and dimension (patch length, thickness, etc.). Broadband or multiband absorbers can also be implemented by engineering the patch absorber shapes.

Fig. 6.2 shows the electromagnetic study to obtain optimized bolometer absorber design parameters. The study is conducted by solving Maxwell's equation using finite element method in COMSOL Multiphysics tool. In Fig. 6.2(a), (b), the variation of metal patch length, l is studied and presented. In 6.2(a), the period is varied with the length as $p = l\sqrt{2} + g$, where g is the gap between patches. A small gap is desired to achieve a high fill-factor absorber (thus, high-efficiency absorption) and to ensure that the VO_2 beams are placed in proximity to the patches (thus, high-sensitivity readout). However, in our design, we choose $g = 2\mu m$ to provide ease of fabrication and to avoid coupling between neighboring patch antennas which may cause a significant shift in the resonance frequency. In 6.2(b), the length, l is varied while keeping the period constant as $p = l_{max}\sqrt{2} + g$, where l_{max} is $50\mu m$ for this analysis. The length of the metal patch is observed to be predominantly controlling the frequency or wavelength of the resonance peak, which is expected, as resonant wavelength, $\lambda_R \propto l$ [106]. Fig. 6.2(c), (d) shows the absorption profiles as the metal patch thickness, t_M and dielectric thickness, t_D of the MIM structure is varied. We observe that the absorption by bolometer active area is higher for higher values of thicknesses within the considered range that is deemed practical. As such, it may seem desirable to choose thicker materials stacks for the bolometer device for better sensitivity. However, there is a trade-off between material thickness and bolometer bandwidth. A thicker material stack costs in terms of sensor speed or bandwidth as it leads to larger heat capacity and higher thermal time constant. Overall, these results from our analyses thus suggest a shift in strength and wavelength of resonance for a change in MIM absorber layer thicknesses and/or patch length which causes shift in magnetic and electric dipole resonance at radiation incidence. The design is thus highly flexible and scalable.

Each pixel absorbs incident radiation and converts absorbed energy to heat. At transient, the heat is localized based on the plasmonic field enhancement, and the localized temperature variation affects the resistivity of local transducer beam. The steady-state heat is distributed over the entire pixel causing the rise in its temperature profile. High-TCR VO_2 beams [107, 108] biased at transition are integrated in the pixel to electronically sense this temperature variation with highest possible sensitivity. Biasing the phase-changing beams near their transition temperature (68°C) ensures the device operation near the highest-TCR point. The temperature biasing can be done by setting the device at the transition temperature by thermo-electric or Peltier heater. As an alternative, engineered VO_2 [109, 110, 111, 112] with lower transition temperature closer to room temperature can also be used to circumvent the necessity of thermal biasing. The use of micro/nano-transducer beams enables higher readout

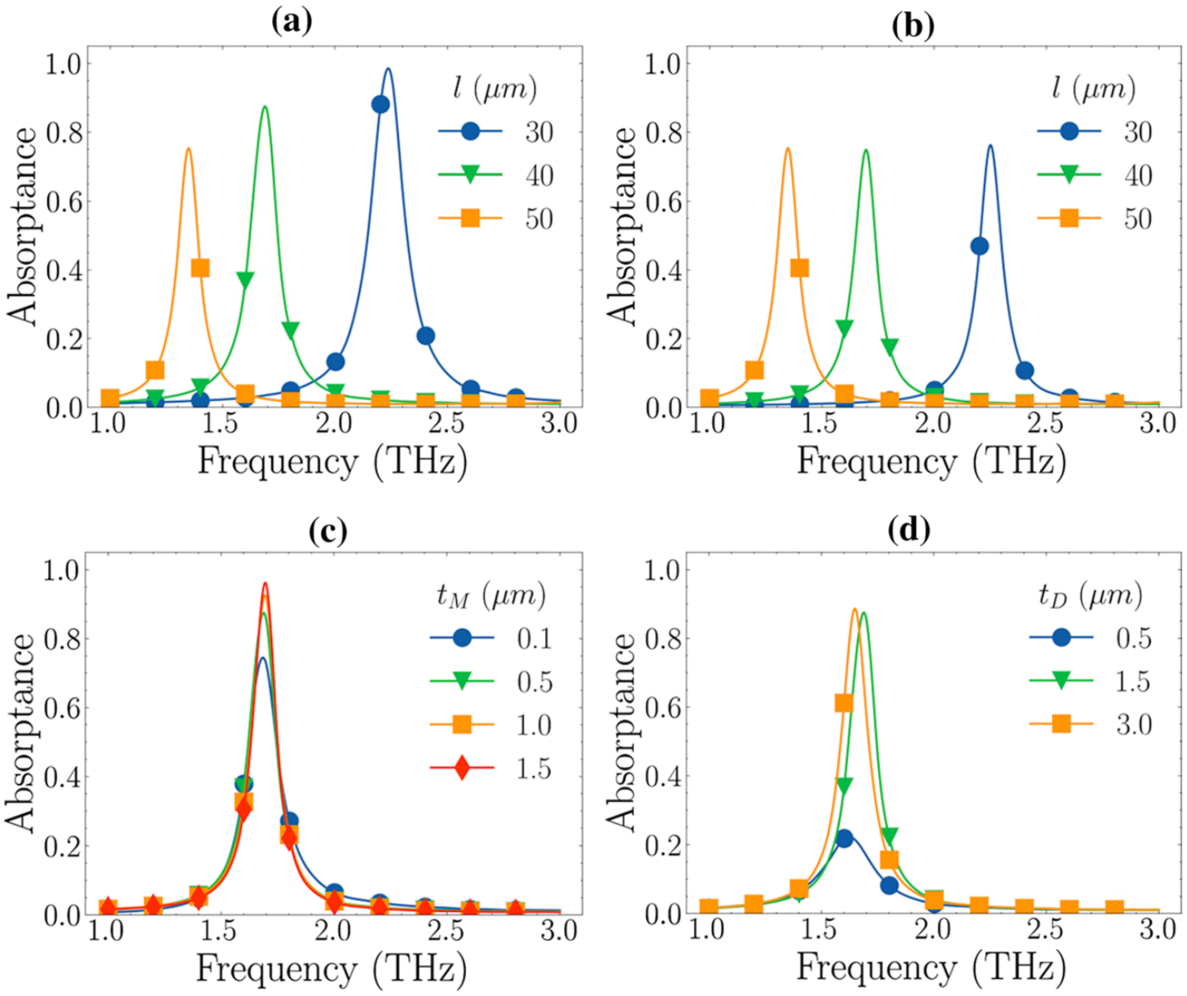

Figure 6.2: Electromagnetic study of bolometer absorber design parameters to achieve high radiation absorption efficiency. Absorptance profile—(a) for varying patch length, l . In this case the period, $p = l\sqrt{2} + g$, where g is the gap between patches with a default value of 2 μm, (b) again for varying patch length l . In this case the period, $p = l_{max}\sqrt{2} + g$, where l_{max} is 50 μm and g is 2 μm by default, (c) for varying metal patch thicknesses, t_M. for default design 0.5 μm is selected as a trade-off between bandwidth and sensitivity, (d) for varying dielectric thickness, t_D. In the default proposed design, t_D of 1.5 μm is selected for the same reason

resistance variation and sensitivity due to increased length to cross-sectional ratio [107, 108]. Overall, the integration of plasmonic absorbers and transducer beams in the bolometer pixel allows significant design flexibility and scalability while improving the responsivity and pixel density.

6.2 Thermal and Mechanical Analysis

The proposed THz bolometer consists of suspended structures or pixels to allow better thermal isolation and increased sensitivity. The suspended design helps to reduce the thermal conductance and increase thermal resistance and isolation allowing the desired heat buildup for sensing the temperature induced variation in resistance. The suspended structure also necessitates mechanical stability under periodic radiation incidence over a long time. Previously, we have studied the interplay between mechanical design and thermal performance of bolometers and plasmonic sensors for IR detection [107, 108, 113, 114, 115]. However, the shift in target wavelength and frequency of operation to THz regime renders a shift in the design parameters such as device geometry. As such, thermal, mechanical, and thermo-mechanical properties are expected to change, and a careful study should be performed for new frequencies. Therefore, it is essential to study the thermal and mechanical properties of the suspended structure for THz domain, which we cover in this section.

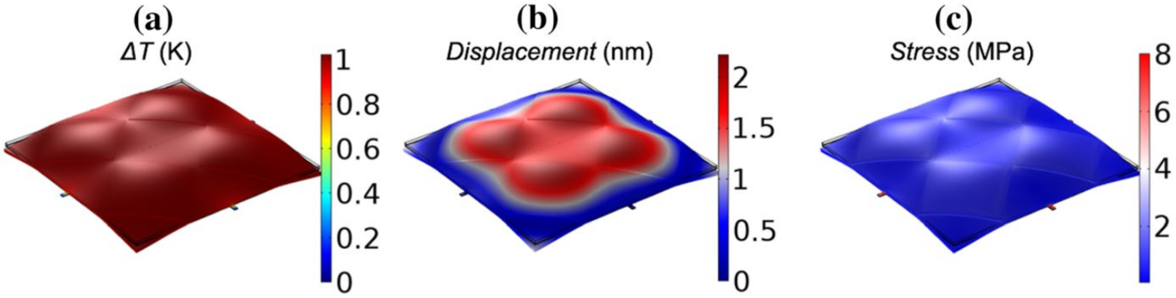

Figure 6.3: Thermal and mechanical study of the proposed THz bolometer pixel under suspension. (a) $\Delta T = T - T_o(K)$, where T_o is the ambient temperature, when radiation at peak absorption frequency of 16 μW power is incident on the pixel. The steady state average temperature rise of 1 K on the pixel indicates that the thermal conductance of the bolometer design is 16 μW. (b) Displacement (nm) of the bolometer pixel due to mechanical suspension and thermal stress, showing a maximum displacement of about 2 nm. (c) von Mises stress (MPa) profile of the bolometer pixel showing a maximum stress of about 8 MPa near the arms of the suspended structure.

A bolometer performance metrics depend on the value of thermal conductance, G_{th}, which is defined as the incident heat power that is required to increase the steady-state temperature of a structure by 1 K. We calculate the amount of required incident radiation that raises the temperature of the device active area by 1 K as $G_{th} = 16$ μW/pixel. Fig. 6.3(a) illustrates the expected temperature change profile ($\Delta T = T - T_o$, where T_o is the ambient temperature) at the steady state following a 16 μW/pixel incident radiation at the absorber resonant frequency. The mechanical displacement profile of the suspended structure corresponding to 1 K temperature change is shown in Fig. 6.3(b). We observe a maximum displacement of 2 nm due to thermal stress upon radiation incidence. Fig. 6.3(c) shows von Mises stress profile in MPa. A maximum stress of 8 MPa is observed on the bolometer arms. This is much smaller than the limit of 44–470 MPa that silicon nitride can endure over many cycles as a support layer [116, 117]. This stress limit determines the maximum incident power that each pixel can withstand over multiple cycles. The high-TCR VO_2 beams allow the detection of even a tiny fraction of 1 K temperature variation. This reflects in high responsivity which is discussed in later section.

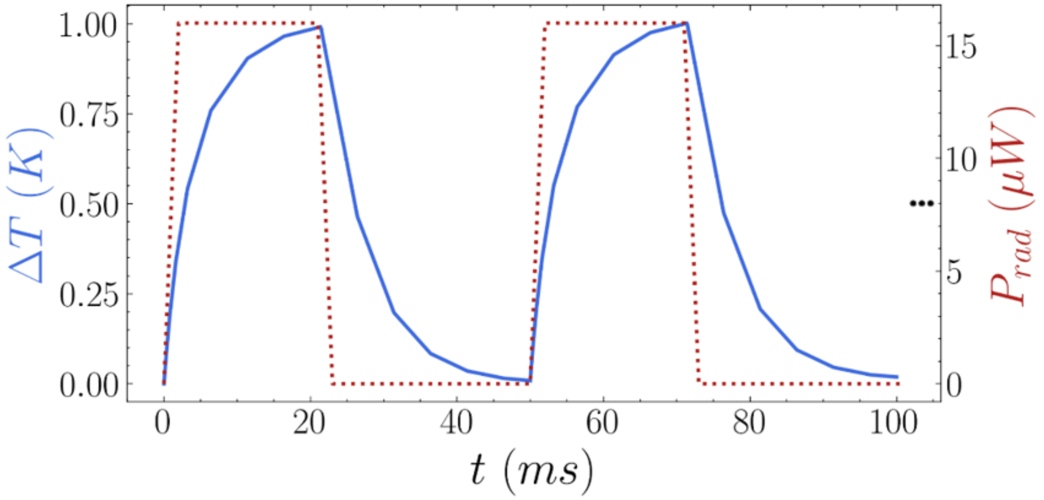

Figure 6.4: Thermal time (t) response of the bolometer pixel upon periodic radiation incidence of 50 ms period and 40% duty cycle. Red dotted line shows the 1.7 THz incident radiation power P_{rad} (right y-axis) pulsating between 0 and 16 μW, which is the power required to increase device temperature by 1 K. Blue solid line shows the average temperature rise of the device (left y-axis) along the location of the four arms upon pulsed radiation incidence, $\Delta T = T - T_o(K)$, where T_o is the ambient temperature. From the transient analysis, the rise time, τ_R and fall time, τ_F are calculated to be 10.9 ms and 13.4 ms, respectively. The average thermal time constant is calculated as $\tau_t h = (\tau_R + \tau_F)/2 = 12.15 ms$.

The speed of operation or bandwidth of the bolometer is determined by the device thermal time constant. It is obtained by conducting transient analysis by applying a pulsed heat source. A $16\mu W$ 1.7 THz rectangular pulsed radiation of 50 ms period with a pulse duration of 20 ms is modeled to be incident upon the bolometer structure. The average temperature rise is calculated by Multiphysics analyses and plotted in Fig. 6.4. We calculate the rise and fall times by taking the time difference between 90% and 10% of the final temperature difference at the rising and falling edges, respectively. We obtain the rise time, $\tau_R = 10.9$ ms, and the fall time, $\tau_F = 13.4$ ms. Hence, the thermal time constant, $\tau_{th} = 12.15$ ms is calculated by taking the average of the rising- and falling-edge time constants.

6.3 Polarization Detection

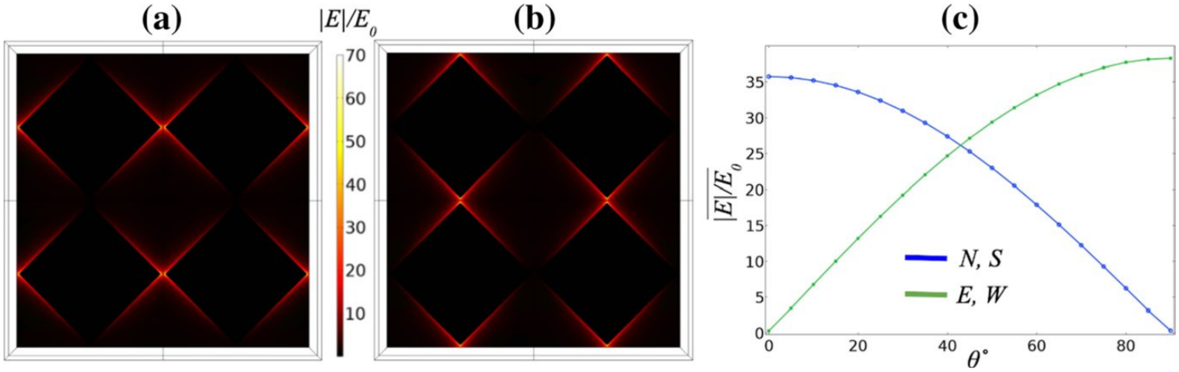

Figure 6.5: (a) Field distribution for E_x (same axis as Fig. 6.1(b)) showing field enhancement at horizontal tips of the square patches (b) field distribution for E_y showing field enhancement at the vertical tips (c) calculated average field enhancement along the gap between tips with respect to polarization angle (x-axis, $\theta = 0°$ and y-axis, $\theta = 90°$) at the horizontal (blue—transducer beam arm location N and S as in Fig. 6.1(b)) and at the vertical (green—transducer beam arm location E and W as in Fig. 6.1(b)) tips of the top layer patches

Along with the detection of THz radiation intensity, the knowledge of its polarization can often be essential for interpreting the results and measurements particularly in THz spectroscopy and imaging [118, 119]. With the proposed implementation of plasmonic absorber cells and transducer beams, polarization of the incident radiation can be determined without additional components or complexity in the system. The transient heating due to incident radiation is localized at specific patch gaps based on polarization and can lead to different thermal energy development at different transducer arms. To highlight polarization sensitivity, the field distributions in a pixel for incident E_x and E_y polarizations are shown in Fig. 6.5(a), (b). We acknowledge that, at steady state, the temperature rise due to radiation absorption and localized field will be distributed across the entire pixel. However, the transient localized field and temperature rise will contribute to the readout signal across a particular arm. This transient duration depends on the thermal time constant of the pixel which in turn depends on device geometry and material properties like heat capacity and thermal conductivity. Hence, a transient probe can enable the polarization detection of the incident radiation. As observed from Fig. 6.5(a), E_x polarization causes transient local heating near arms N and S. Arms E and W do not experience the local heat buildup thus far. Therefore, the readout signal along N-S will manifest stronger modulation compared to E-W. When the temperature gets distributed across the entire pixel by means of conduction, the readout along E-W will be similar to N-S. Similarly, E_y polarization causes greater change in readout signal along E-W compared to N-S. Hence, the instantaneous reading across N-S or E-W electrodes reveal the polarization state of the incident beam. Fig. 6.5(c) demonstrates the average field enhancements along the gap between the tips of adjacent square patches for a polarization angle between 0° and 90°. We observe that the average field enhancement along the gap can reach up to 35 and declines to 0 for a polarization orthogonal to the gap line. Any arbitrary polarization angle, θ between 0° and 90° can be estimated by

$$\theta = \tan^{-1}\left(\frac{F \cdot E_{\cdot E,W}}{F \cdot E_{\cdot N,S}}\right) \tag{6.1}$$

where, $F.E._{E,W}$ is the average field enhancement along E and W arms, and $F.E._{N,S}$ is the average field enhancement along N and S arms. The readout signals across the arms depend on local temperatures which in turn depend on field enhancement. Consequently, by measuring the relative strength of transient readout signals across E-W and N-S arms, we can estimate the polarization angle.

6.4 Performance

The performance of a bolometer is evaluated based on its responsivity (R_v), noise equivalent power (NEP), and detectivity (D^*). The responsivity, R_v is an important performance metric that is defined by the generated current or voltage for a 1 W incident radiation, and it can be expressed as equation 3.6.

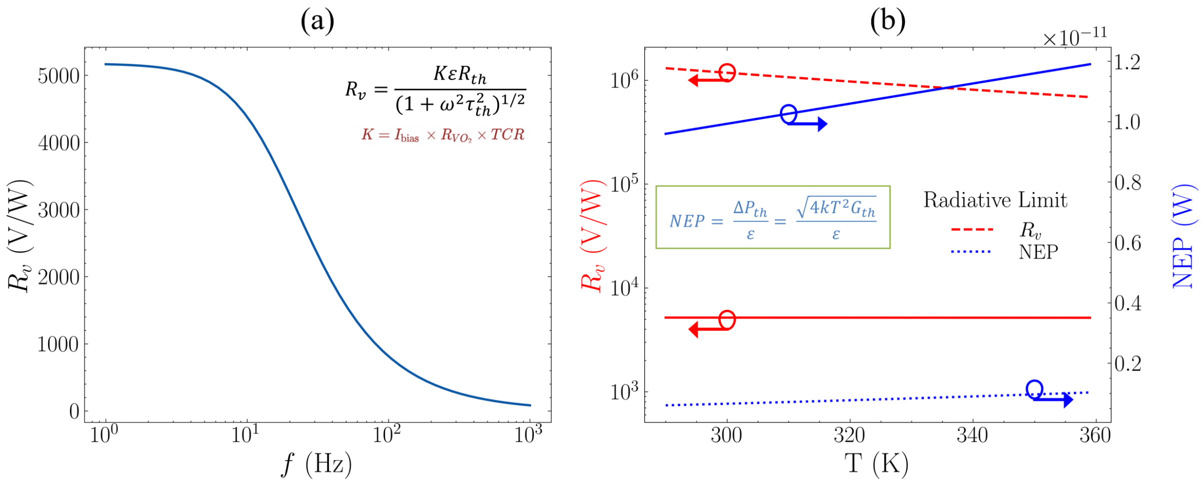

Figure 6.6: (a) Responsivity of the proposed design of THz bolometer over a range of frequency from 1 Hz to 1 kHz at a device temperature of 341 K, and (b) Responsivity (red, left y-axis) and NEP (blue, right y-axis) with respect to device temperature at 1 Hz. The radiative performance limit is shown as well with broken lines

I_{bias} is the bias current, which has a default value of $1\mu A$ for all calculations. This value of current is practical and is chosen to limit the Joule heating induced temperature change in the detector as well as to keep the power requirement as low as possible while producing readout voltage signals above the noise level. Through-out the analysis, $R_{VO_2} = \rho_{VO_2}\frac{l_{beam}}{A_{beam}}$, is the resistance of VO_2 beam, where ρ_{VO_2} is the resistivity of VO_2 material strongly dependent on temperature, l_{beam} and A_{beam} are the length and cross-sectional area of the VO_2 beam along readout path with values of 125 μm and 0.15 μm × 1.8 μm, respectively. Such dimensions of the beam are chosen to limit resistive noise ($\propto R_{VO_2}$) while enhancing responsivity. As apparent from Eq. 3.6, the responsivity of the detector is proportional to the beam length, l_{beam} and inversely proportional to the beam cross-sectional area, A_{beam}. The resistivity at the transition temperature (68°C) is considered to be 10^{-2} $\Omega.cm$ for calculation [120]. TCR is the temperature coefficient of resistance of the transducing VO_2 beam which is temperature-dependent and has a value of $200K^{-1}$ at phase transition [121, 122, 123, 124], ε is the emissivity of absorbing antennas which is same as the absorptance calculated earlier which at resonance has a maximum value of 0.87, $R_{th} = \frac{1}{G_{th}}$ is the thermal resistance, ω is the angular frequency of the radiation, τ_{th} is the thermal time constant of the detector pixel. Thus, using transducing beams instead of a film in a bolometer detector results in higher responsivity detection. Fig. 6.6(a) shows the responsivity of the proposed design for THz bolometer at 341 K (VO_2 transition-edge thermal bias) over the frequency ranging from 1 Hz to 1 kHz. The cutoff frequency that defines the bandwidth of the detector is observed to be about 20 Hz. The bandwidth can also be related to the thermal time constant, $BW =$ 20.58 Hz. The responsivity at 1 Hz with respect to device temperature is shown in Fig. 6.6(b)—red, solid line. Its value decreases with temperature although it is observed to be flat in a log-scale for the range of temperatures shown. Due to the selected large length to area ratio of the VO_2 beams, the low-frequency responsivity is estimated to be over 5000 V/W.

NEP of the proposed bolometer can be estimated using equation 3.7. A is active area which is $2l\sqrt{2} + g$ by $2l\sqrt{2} + g$, where l is the side of square patches (default value 40 μm) and g (default value 2 μm) is the gap between the patch tips, T = 341 K. Fig. 6.6(b) shows the NEP over a range of practical device operating temperatures. The estimated NEP is $10^{-12}pW$ over the temperature ranging from 290 to 360 K at 1 Hz frequency. This value of NEP is competitive with other THz bolometers reported in recent years

[125, 126, 127, 128, 129, 130]. As expected, the NEP increases with temperature due to the increased resistive noise contribution at higher temperature and decreased responsivity.

$$NEP = \frac{\Delta P_{th}}{\kappa} = \frac{\sqrt{4kT^2G_{th}}}{\sigma} \tag{6.2}$$

The radiative limit is the theoretical performance limit of the device when the device operates in a perfect vacuum system with only the radiative heat transfer mechanism present. The conductive and convective heat transfer is considered insignificant in this definition. The radiative limit responsivity and NEP are shown in Fig. 6.6(b)—red and blue broken lines, respectively. The radiative or theoretical limit of NEP is achieved when G_{th} approaches $G_{th} = 4A\varepsilon\sigma T^3$ [58]. The proposed detector is observed to have an NEP close to the radiative limit. However, the responsivity limit is in the order of 10^6, which is much higher than the value we report. The proposed design can be modified, for example, by utilizing narrower and longer suspension arms, thus increasing bolometer thermal isolation, to achieve a performance closer to radiative or theoretical limit in terms of sensitivity i.e., responsivity and NEP. However, the trade-off between sensitivity and frequency response is needed to be considered.

The calculated detectivity for the proposed design is calculated using Eq. 3.8 and is shown in Fig. 6.7. We present the detectivity of our THz bolometer with respect to frequency, device temperature, and thermal conductance. Our design achieves a low-frequency detectivity over 4×10^8 $cm.Hz^{1/2}.W^{-1}$ Fig. 6.7(a) shows slight temperature dependency on the detectivity as higher operating temperature reduces sensitivity. A large coefficient, K and large thermal resistance, R_{th} contribute to large detectivity. The detectivity with respect to the device temperature is presented in Fig. 6.7(b) for different discrete frequency of operation showing a down trend with increasing device temperature. D^* is also calculated for a range of thermal conductance at discrete frequency and temperature values and shown in Fig. 6.7(c),

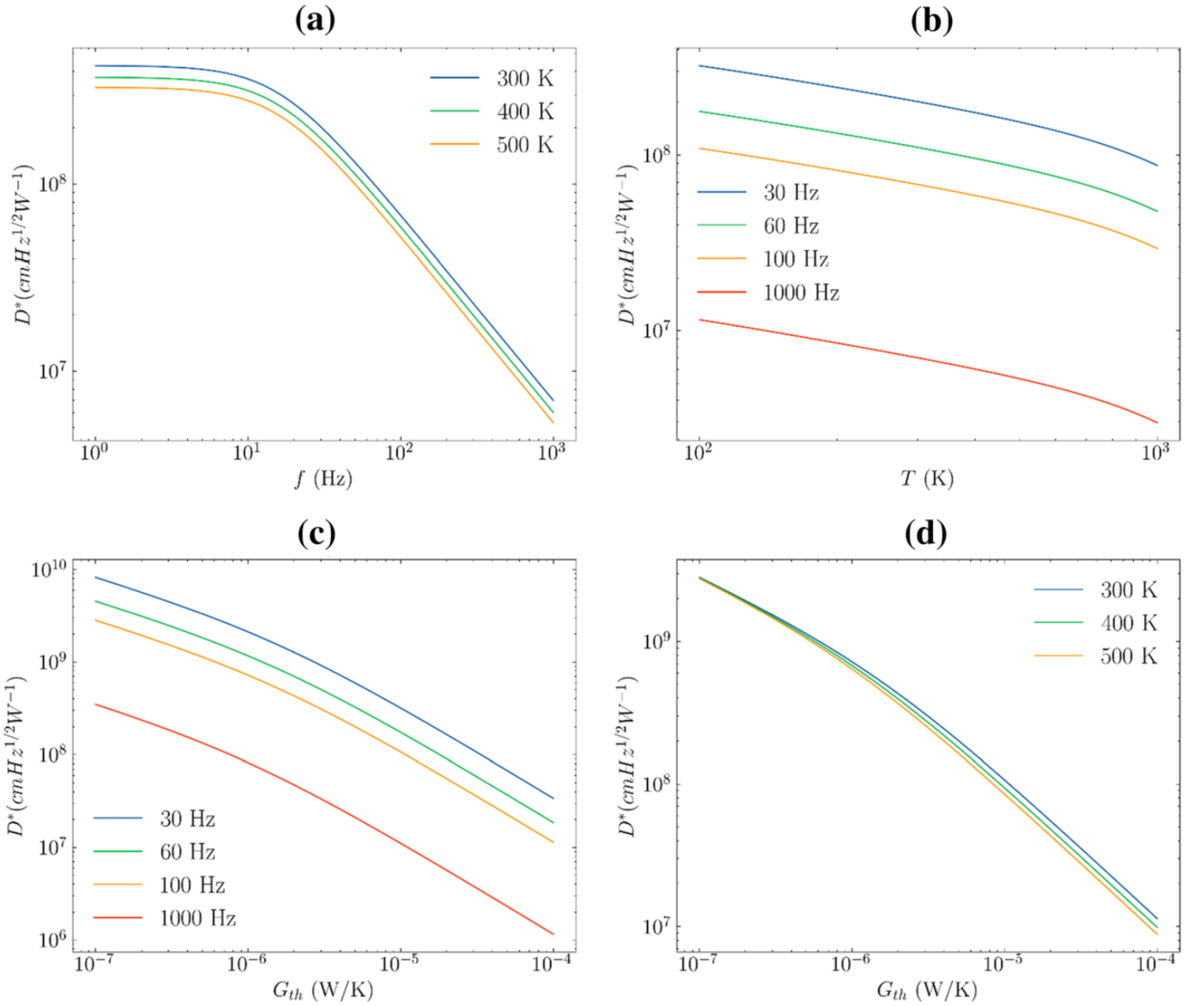

Figure 6.7: Detectivity with respect to frequency, device temperature, and thermal conductance. (a) Over the frequency range from 1 Hz to 1 kHz for three different device temperatures, (b) over the device temperature range from 100 K to 1000 K for four different frequencies of operation, (c) over theoretical thermal conductance range from 10^{-7} W/K to 10^{-4} W/K for different frequency, and (d) different device temperature

(d), respectively. The graphs indicate the required G_{th} that is needed to achieve a certain D^* as a reference for device optimization. Design parameters, materials, and geometry of the bolometer can be modified to reach different levels of thermal conductance G_{th} and thus different levels of D^*. For example, a thermo-mechanical design with narrower and longer legs to reduce the thermal conductance G_{th} to 10^{-7} $W.K^{-1}$ could enhance D^* to up to 10^{10} $cm.Hz^{1/2}.W^{-1}$ at a frequency of 30 Hz.

6.5 Noise Analysis

Fig. 6.8 shows all three noises as a function of frequency when the device is at 341 K temperature and as a function of device temperature when the frequency is fixed at 100 Hz. As seen from Eq. 3.9, the overall Johnson noise depends on the bandwidth, operating temperature, and the resistance of the device. The Johnson noise is resistive and increases with device temperature and equivalent readout resistance. We define the equivalent readout resistance as the resistance appearing between terminals where bias current is applied, and voltage signal is read across. The main contributing resistance is the resistance of the VO_2 beam resulting in an equivalent resistance very close to R_{VO_2}. Below transition temperature, a VO_2 beam is highly insulating and will result in a very large resistance value and thus a very large resistive noise. To mitigate this noise and at the same time achieve greater sensitivity with high TCR, we propose to set the device temperature at the transition temperature of VO_2. The resistivity of the VO_2 beam can thus be reduced by two orders of magnitude compared to its room-temperature semiconductor phase resistivity. Besides providing a high-TCR transducer, transition-edge biasing results in decrease of the Johnson noise and ultimately compensate for the noise development due to increased device temperature. Fig. 6.8(a) shows how the Johnson noise is a white noise and flat with respect to the frequency, and Fig. 6.8(b) shows how it increases with temperature.

Any temperature fluctuation on the detector generates thermal fluctuation noise. It is proportional to the thermal resistance and to the square of temperature. This is one reason to keep the thermal resistance in check. The temperature fluctuation contributes to fluctuation in readout voltage, V_{th} which is expressed in Eq. 3.10. We observe the frequency dependence of thermal fluctuation noise from Fig. 6.8(a). Its relation to temperature is represented by Fig. 6.8(b) and it shows expected trend with respect to temperature.

The third type of noise is the background noise, V_b which is caused by radiative heat exchange

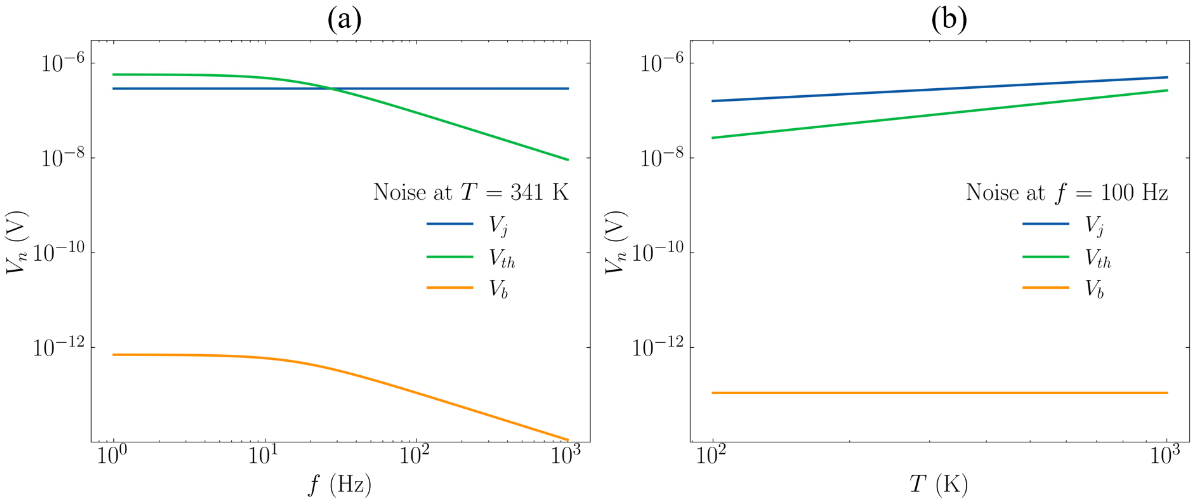

Figure 6.8: All noise sources with respect to (a) frequency at bolometer temperature of 341 K and (b) bolometer temperature at a frequency of 100 Hz.

between the detector and ambient. It is related to the bolometer parameters by Eq. 3.11. Being in the order of 10^{-13} V over the frequency and bias temperature range of interest, this type of noise has insignificant contribution to the overall noise and thus can be neglected for the proposed detector. Putting all the different noises together, thermal fluctuation and Johnson noise are observed to be dominant and of the same order (sub 1 μV).

6.6 Chapter Summary

In summary, we report a novel THz sensor with the capability to detect incident radiation along with its polarization at 1.7 THz frequency. The sensor incorporates polarization-sensitive plasmonic absorber and phase-changing VO_2 transducer beams. Our design is estimated to achieve a responsivity over 5000 V/W, an NEP below 12 pW, and detectivity over 10^8 $cm.Hz^{1/2}.W^{-1}$ The design can be easily tuned to accommodate absorption of different bands within the THz spectrum as well as multi-band detection. Our proposed device can be utilized in THz imaging and sensing applications that requires inexpensive uncooled detection with high sensitivity.

Chapter 7

Proof-of-concept Prototype

A proof-of-concept device fabrication and characterization is planned and executed to gauge the practicality of the proposed integration of plasmonic absorbers and rectangular VO_2 beams. The layout of the proof-of-concept device along with the two main characterization components is shown in Fig. 7.1.

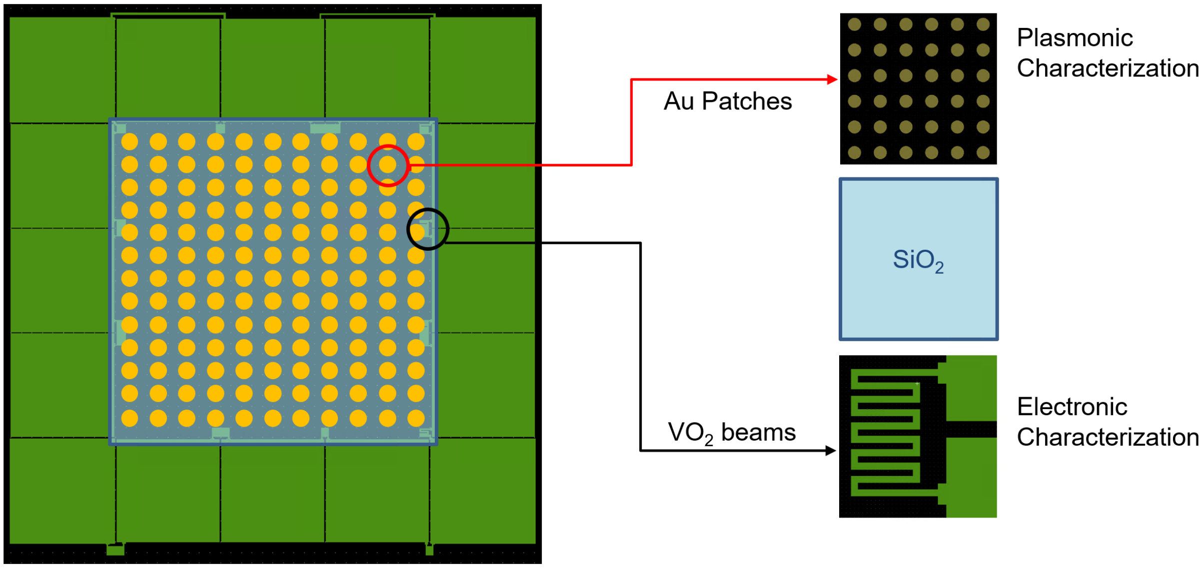

Figure 7.1: Layout of the proof-of-concept device

The green square blocks represent the pads required for electronic probing. The pads separate two regions - inner and outer. The inner region has vertical layers as presented in 5.1. The stack-up (from bottom to top) of material layers in the inner region is Si/ SiO_2/ Si_3N_4/ W /SiO_2 /VO_2 (only present in the beam patterns) /SiO_2/Au (patch shapes - circular or square). SiO_2 is used instead of suspension due to its thermal insulating property and for ease of fabrication for the proof-of-concept device. The outer region does not have the top two layers - SiO_2 burial layer and top gold patches. The inner region surrounded by the pads are about 3 mm × 3 mm. Such dimension is chosen to allow spectroscopic measurement of the plasmonic absorber design. This is because the Cary-7000 Universal Measurement Spectrophotometer (UV-Vis-IR) which is used for the spectroscopic characterization has a rectangular beam of about 1 mm × 3 mm dimension. In Fig. 7.1, the gold patches are exaggerated in shape and understated in numbers for visualization purpose. The diameters of the fabricated gold patches and gaps between adjacent patches range from 1.6 μm to 5 μm. Each proof-of-concept device is about 5 mm. As such, we use diced square samples of 3 cm sides consisting of 9 devices with different patch shapes and diameters (1.6 μm to 5 μm).

The material stack-up in the pads location is Si/SiO_2/Si_3N_4/W/SiO_2/VO_2(only present in the beam patterns)/Au. The pad dimensions are kept large enough (1 mm × 1 mm) to comfortably allow the placement of probe tips or wire bonds. The pads basically act like electronic terminals for the temperature sensitive resistors (VO_2 beams) in between. VO_2 beams of different sizes and aspect ratios are included in the pattern to be studied. VO_2 beams are included both in the inner and outer region. The inner beams are integrated with the plasmonic absorbers whereas, the outer beams are not integrated with plasmonic absorbers. The comparative study between inner and outer VO_2 beams aims to reflect the effect of plasmonic absorbers. The width of the VO_2 beams to be fabricated ranges from 2 μm (close to photo-lithographic limit) to 10 μm. The length ranges from 50 μm to 1.1 mm. Most beams are laid out in a winding or serpentine path. Two outer beams are kept straight to easily calibrate each sample after fabrication. The legs of the beams (where the beams connect to terminal pads) are made wider to avoid high impedance zones or breaks in connection after lithography and etching.

A 300 nm thin stoichiometric Si_3N_4 film is first deposited on a Si (585 μm)/SiO_2 (4 μm) substrate by low pressure chemical vapor deposition (LPCVD). Then a 50 nm tungsten (W) and a 50 nm SiO_2 film is deposited respectively by sputtering (Denton Discovery 550). VO_2 film of 50 nm thickness is then deposited by PLD method. Sputtering process for VO_2 deposition and sputtered VO_2 films are also studied and characterized. However, this method was not used for the proof-of-concept device fabrication due to extensive calibration requirement and poor repeatability in our case. After the deposition of VO_2 film, it is etched using lithography steps to produce VO_2 pads and beams of different sizes. The second layer of 50 nm SiO_2 is then sputtered and lifted-off to bury the VO_2 beams in the inner region where top metal patches are designated to be deposited and patterned. This is important to avoid unintended electrical shorting of VO_2 beams by the metallic structures. Also, the VO_2 pad regions are exposed after the lift-off so that the metal pads can be deposited directly on the VO_2 pads for proper electronic probing with low contact impedance. Finally, the 100 nm thick gold pads (aligned with the VO_2 pads) and circular patches (as the top metal layer of the plasmonic absorbers) are created by lift-off technique after e-beam deposition (CHA Solution electron beam evaporator). The pads are 1 mm × 1 mm to easily allow electronic probing via wirebonding or directed contact with probe-tips. The summary of the fabrication steps is shown in Fig. 7.2.

Similar lithographic steps are carried out to pattern VO_2 beams, pads, SiO_2 top layer, Au patches and pads. The AZ 5214E resist is used for all lithography steps as both negative and positive photoresist depending on the mask layout and patterning method (i.e., lift-off or etching). Before the resist coating, the sample is cleaned using acentone, IPA, and DI water. Then the sample is baked at 100°C for 2 mins to remove water molecules from the sample. After the dehydration bake, the sample is kept in a hexamethyldisilazane or HMDS chamber

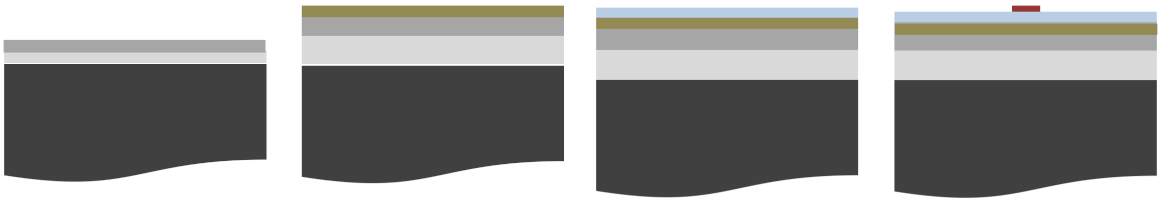

(a) LPCVD Nitride (b) W Film Deposition (c) SiO_2 sputtering (d) VO2 Deposition and Etching

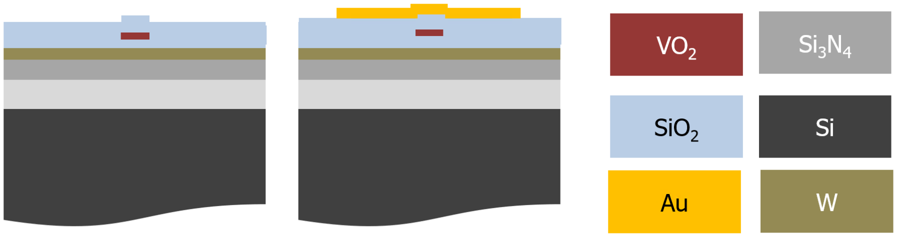

(e) Second SiO2 Sputtering (f) Au Deposition and Lift-off

Figure 7.2: Fabrication steps summary for the proof-of-concept device (material layer thickness and lateral dimensions are not to scale). (a) LPCVD Si_3N_4 deposition on Si/SiO_2 substrate, (b) Sputtering tungsten, (c) Sputtering SiO_2, (d) Deposition and etching of patterned VO_2, (e) Sputtering of the second SiO_2 to cover VO_2 beams where needed, (f) Gold e-beam deposition and lift-off to create plasmonic absorber patches and pads.

for 5 mins. HMDS acts as a photoresist adhesion promoter and is commonly used before the application of the photoresist making the resist-coating process easier and uniform. The AZ 5214E resist is then spun-coated on the sample with a 4500 rpm spin rate for 30 seconds giving a uniform resist profile of 1.6 μm (checked by Nanospec). The sample is soft-baked at 100 °C for 50 seconds to prepare it for UV exposure. Karl Suss MA6 contact aligner is used for mask-sample alignment and UV exposure (365 nm wavelength). The first UV exposure time is adjusted to 5 - 7 seconds for different steps of the lithography. To use the photoresist as a negative resist, the sample is undergone two additional steps - reversal baking the sample at 120°C for 45 seconds and flood exposure for 30 seconds. The exposed and cross-linked resist is developed in AZ 300 MIF for 70 seconds making the sample ready for etching or deposition and lift-off. Long acetone soak and ultrasonic acetone bath are used for resist removal (lift-off) after etching (deposition). Designated and stronger resist strippers like AZ 300T, NMP (N-Methylpyrrolidone) etc. are avoided as they tend to corrode metal films and VO_2. The optical microscopic images of VO_2 films and nanobeams after photoresist stripping process with AZ 300K are shown in 7.3. Corrosion is observed in the features. The extent of corrosion depends on the time of the process.

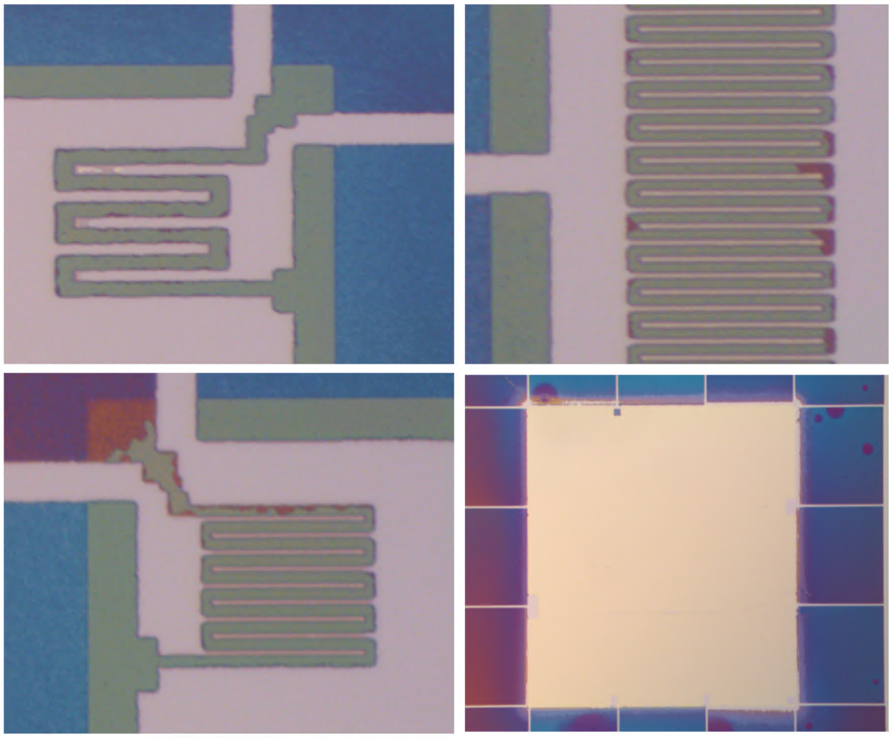

Figure 7.3: Damage of VO_2 films and nanobeams after using AZ 300K resist stripper. The optical microscopy shows clear corrosion in VO_2 features when strong resist strippers are used.

7.1 X-ray Diffraction

X-Ray Diffraction or XRD is a widely used technique to study the crystallographic structure of a material. It is done by measuring the diffraction pattern produced when a beam of x-rays is directed onto the sample. The diffraction pattern resulting from the interaction of the x-ray beam with the sample carries information regarding the crystal structure of the materials. As such, the pattern can be analyzed to determine the crystal structure and orientation of single and polycrystalline materials as well as powders. It is a non-destructive technique, meaning that the sample is not altered or damaged during the measurement. It is a common technique for the characterization of a wide range of materials used in materials science, geology, chemistry, and other fields. There are a few variants of XRD, for example, HTXRD and GIXRD, which are used in this work.

HTXRD stands for High-Temperature X-Ray Diffraction. It is used to study the crystal structure of materials at high temperatures. Some materials undergo a change in their phase or crystal structure at elevated temperature. HTXRD is often used to study the phase transformations that occur in materials as they are heated or cooled, and to determine the thermal stability of materials.

Another special variant of XRD is GIXRD, which stands for Grazing Incidence X-Ray Diffraction. It is particularly useful in the study of structure and composition of thin films and surfaces. In normal XRD, samples with single or multiple thin films generate diffraction patterns for multiple materials, making the analysis and identification difficult. In GIXRD, to avoid mutiple patterns obscuring each other, a beam of x-rays is directed onto the surface of a sample at a low angle of incidence, typically less than 2°. The small incident angle limits the beam penetration into the bulk material (or other films underneath) as well as optimize the intensity to enhance the sensitivity to the surface region of the sample. It allows the detection of changes in the crystal structure and composition that may occur at or near the surface by reducing overlapping peaks from different depths of sample. It is often used to study thin films, coatings, and other materials with complex surface structures, such as nanoparticles or layered materials.

7.2 VO_2 Film Deposition

The deposition of VO_2 thin films on substrates for device applications is crucial, but it is challenging to achieve uniform films with high purity and crystallinity. Techniques such as sputtering [45, 131, 132, 133, 46], pulsed laser deposition (PLD) [134, 135, 136, 137, 138], and chemical vapor deposition (CVD) [139, 140] are commonly used, but they require precise control over deposition parameters to avoid defects and impurities [141, 49]. The phase transition properties such as the change in the magnitude of resistivity and the width of hysteretic transition are the indicators of film quality which depend on stoichiometry and crystalline structure [141, 49, 142, 143]. Many research efforts have aimed to reduce the transition temperature, including ion-assisted reactive evaporation followed by thermal annealing and relaxing tensile stress by ion bombardment. However, these methods can lead to some degradation of the desired electrical and optical properties.

The deposition of a pure VO_2 film is challenging due to the close co-existence of multiple oxides of vanadium. As such, the deposition process needs to be tightly controlled. We carried out two different deposition techniques - RF magnetron sputtering [144, 145] and PLD [134, 146, 147, 148], however the latter was used for final proof-of-concept device fabrication due to better repeatability. In both techniques, the substrate temperature and the partial pressure of oxygen (O_2) needs to be controlled. Both deposition techniques require high substrate temperature over 400°C. Since, VO_2 material layer, in our proposed design, is integrated with the metal-insulator-metal type absorber, the choice of materials deposited before VO_2 is crucial. Common plasmonic metal films such as gold and their patterned structures can be irreversibly damaged at high temperature [149, 150]. As such, refractory metals [149] are chosen as the ground metal layer of the plasmonic metal-insulator-metal absorber that are deposited before VO_2 deposition.

7.2.1 Sputtered VO_2 Film

The sputtered VO_2 film was achieved by sputtering a 2-inch vanadium (V) target in a AJA ATC 2200-V sputter machine on different substrates such as Si, Si_3N_4, and SiO_2. In O_2

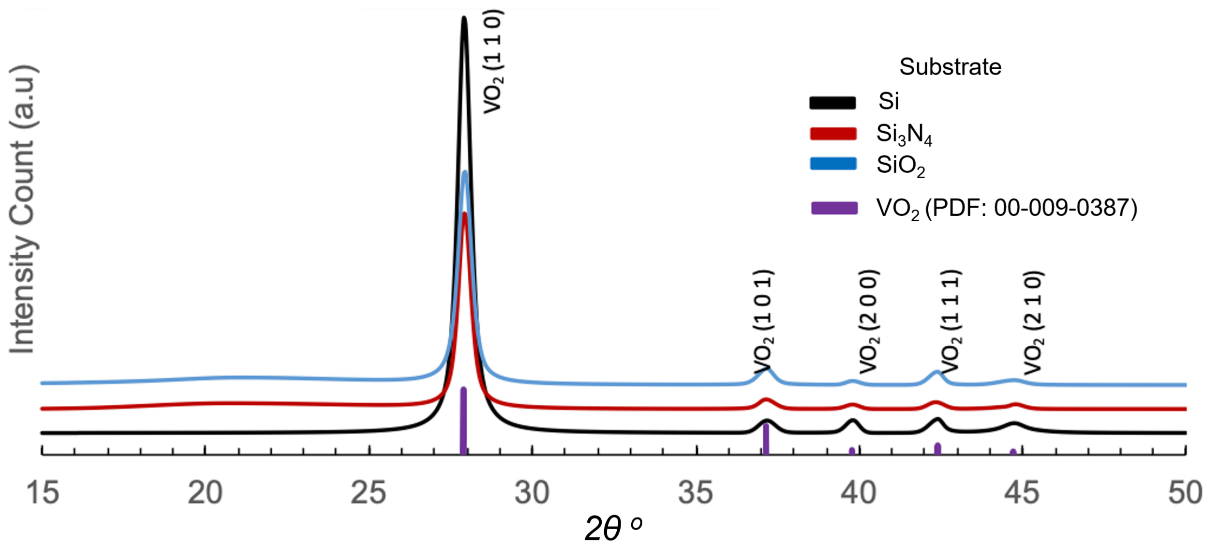

Figure 7.4: XRD profile of sputtered VO_2 film on Si, Si_3N_4, and SiO_2 substrate. The peak positions of the reference material with the best match are also shown.

partial pressure of 0.4 mT and substrate temperature of 500°C resulted in high-quality VO_2 films on all three substrates. Higher O_2 partial pressure resulted in V_2O_5 films whereas lower O_2 partial pressure resulted in V_2O_3 for substrate temperature between 400°C to 600°C conforming with previously reported trend [46].

The XRD analyses of VO_2 films on all three substrates are conducted in Rigaku Smartlab XRD tool and presented in Fig. 7.4. The reference material from software database with the best matching diffraction pattern is presented for identifying the VO_2 and its crystallographic orientation. Additionally, temperature-dependent or high-temperature x-ray diffraction (HTXRD) analysis is carried out on the deposited film to confirm the stoichiometric VO_2 film and its phase transition property. The Anton Paar DHS domed hot stage was used to conduct the temperature-dependent study. The diffraction data are collected 10 mins after the temperature of the stage stabilizes to ensure even and correct temperature distribution in the sample, particularly the top VO_2 film. The temperature-dependent diffraction profile is shown in Fig. 7.5 showing the temperature ramp up and ramp down cycle. Here, the main diffraction peak corresponding to VO_2 is focused for better visualization. The inset demonstrates the peak diffraction angle with respect to temperature showing the hysteresis of VO_2 phase transition. The dominant peak angle of diffraction profile changes from 27.90° to 27.77° as the sputtered film undergoes the transition from insulating to conducting phase upon temperature increase. The diffraction angle along with its shift with temperature corresponds to earlier reported work on the study of VO_2 phase transition [151].

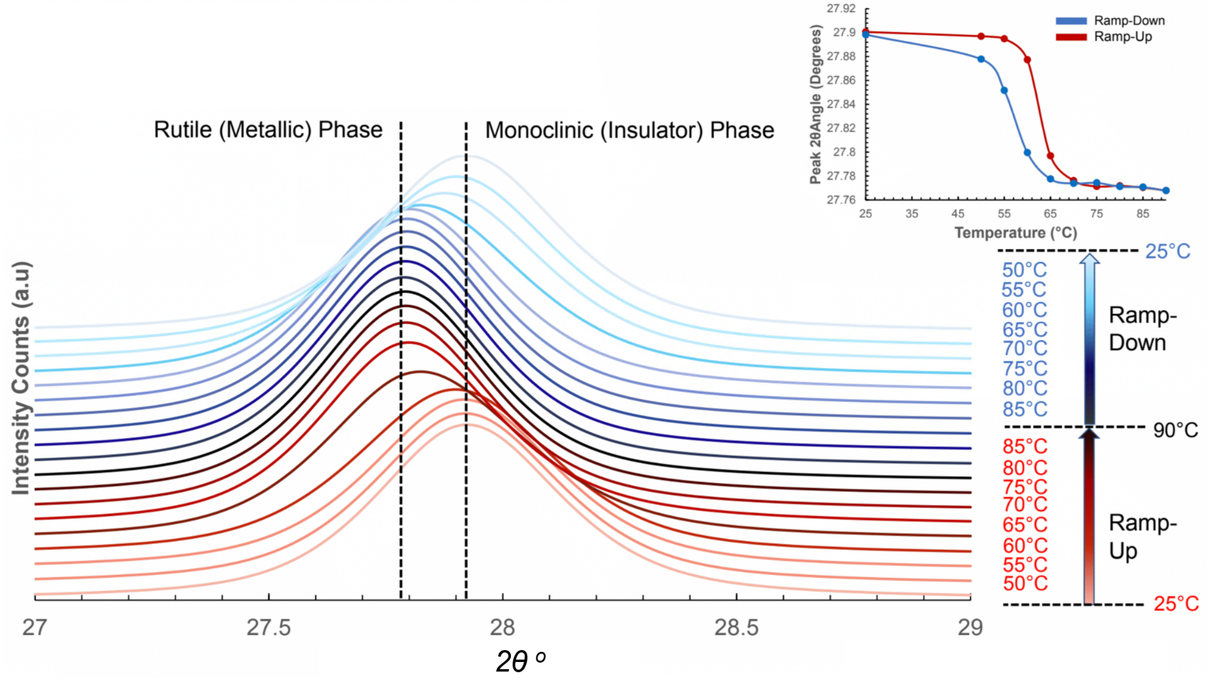

Figure 7.5: Temperature-dependent XRD profile of sputtered VO_2 film on Si substrate showing monoclinic to rutile crystallographic phase transition of VO_2 near 60°C. Y-axis offsets are used to show the XRD profile at different temperatures. Inset shows the diffraction peak angle with respect to temperature confirming the phase transition and hysteresis behavior of VO_2. The transition width is observed to be approximately 5°C.

7.2.2 PLD VO_2 Film

For the proof-of-concept device, a 50-nm thick film of VO_2 is deposited using PLD. The VO_2 layer is deposited on a substrate with pre-existing 300-nm thick dielectric support layer of Si_3N_4, 50-nm thick ground plane metal layer (tungsten, W) of MIM absorber, and a 50-nm insulator layer made of SiO_2, respectively from bottom to top.

The background pressure of the PLD chamber was 3 x 10^{-7} Torr. The deposition of VO_2 was carried out at 500 °C by ablating V_2O_5 ceramic target with 248 nm pulsed laser. The laser frequency and energy fluence were 2 Hz and 1.5 J/cm^2, respectively. The target and sample were constantly rotated during the growth to ensure film uniformity. Oxygen partial pressure of 10 mTorr was maintained during and after growth of film until the temperature was cooled down to 100°C at a rate of 10°C/min.

Because of the multiple thin material layers in the sample, normal XRD gives strong signatures from multiple materials making it challenging to distinguish and identify the diffraction peak of the PLD VO_2 film. To avoid, or at least reduce the diffraction signatures collected from materials underneath the VO_2 film, grazing incidence XRD (GIXRD) is used. The GIXRD profile is shown in Fig. 7.6.

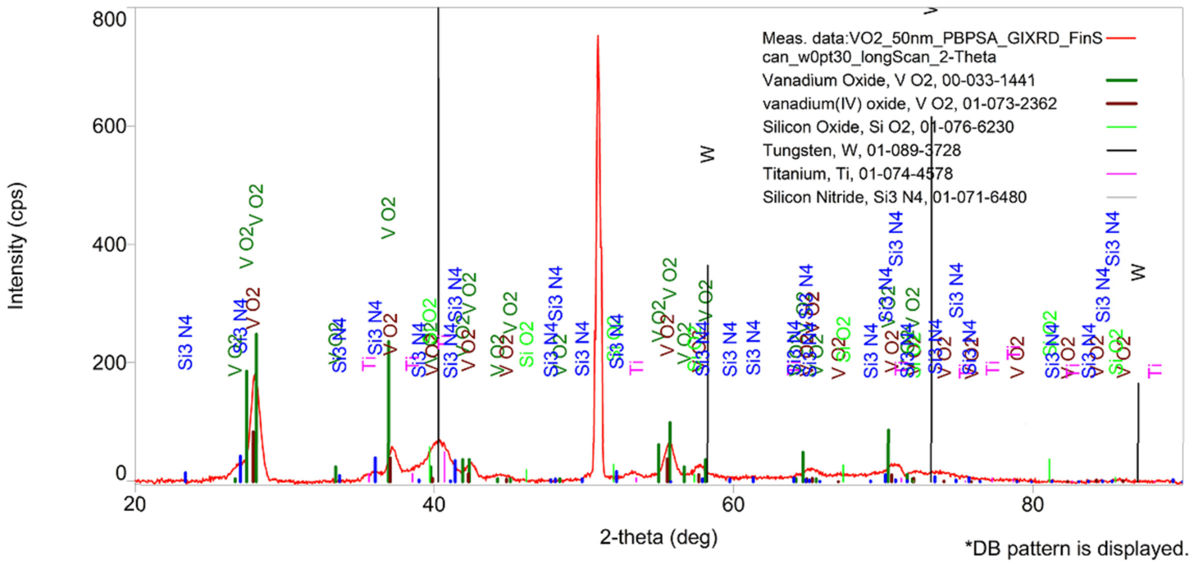

Figure 7.6: GIXRD profile of PLD VO_2 film on substrate with multiple pre-existing layers for proof-of-concept device fabrication. Reference material peaks are shown for identification of different peaks. Multiple diffraction peaks corresponding to inner thin films are observed even with a very small incidence angle of $< 2°$.

Even with low angle of incidence ($< 2°$), diffracted peaks from multiple material layers are observed. The peaks are observed to be relevant to the existing material layers. A strong peak near 28° corresponds to the VO_2 film. However, temperature-dependent study is required to confirm the VO_2 film, which is presented in Fig. 7.7. It shows a hysteretic phase transition of VO_2 confirming the film composition from PLD deposition. The diffraction peak angle corresponding to VO_2 film shifts from 28.08° to 27.94° and a broad hysteresis is observed.

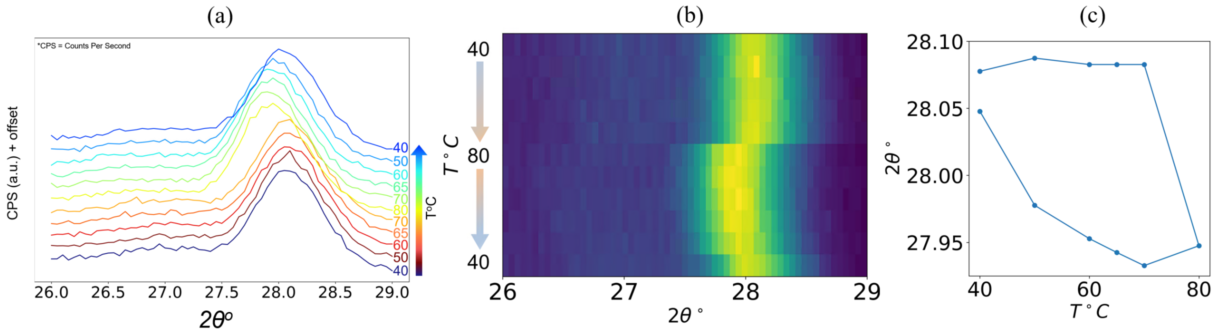

Figure 7.7: (a) Temperature-dependent GIXRD over thermal ramp-up and ramp-down cycle from 40°C to 80°C. Y-axis offsets are used to show the XRD profile at different temperatures. A clear shift in diffraction peak of VO_2 is seen which corresponds to its phase transition property from monoclinic (semiconductor) to rutile (metallic) phase and hysteretically back to monoclinic phase (b) Colorplot showing the peak shift with temperature cycle, (c) diffraction peak angle with respect to temperature showing the hysteresis.

7.3 VO_2 Etching

For patterning VO_2 structures using lithography, lift-off is not suitable due to very high deposition temperature (> 400°C) of VO_2 as the resist material will be damaged at high temperature. As such, it is more feasible to dry etch after VO_2 film deposition to create structured VO_2. Many dry etching processes use O_2 chemistry. However, VO_2 tend to get oxidized very easily [49], and even more so at elevated temperature. Consequently, it is very important to avoid O_2 chemistry during subsequent steps after VO_2 deposition to de-risk oxidization of VO_2 to upper oxides such as V_2O_5. Since VO_2 film is deposited over SiO_2 film, it is important to choose an etching process that has high selectivity between the etch rates of VO_2 and SiO_2 [101]. Based on such limitations, we choose inductively coupled plasma (ICP, PlasmaTherm SLR 770) etching of VO_2 film with Ar/Cl_2 chemistry. Total gas pressure of 12 mTorr with an input ICP power of 600 W and bias power of 50 W was used. The total gas flow rate was kept at 40 sccm with a 60% Cl_2 and 40% Ar (24 sccm Cl_2 and 16 sccm Ar). The estimated VO_2 etch rate was found to be approximately 64 nm/min, similar to the reported etch rate in a previous work [101].

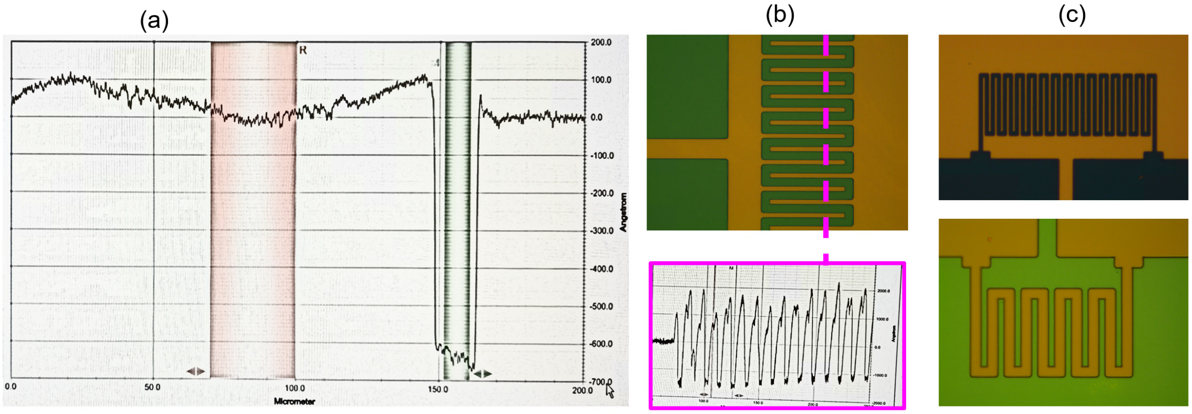

Figure 7.8: (a) Surface profiler measurement on an ICP etched (1 min) VO_2 sample showing etch height profile over a 200 μm horizontal distance, (b) surface profile over the VO_2 serpentine beam, (c) two VO_2 serpentine beams after dry etching.

Fig. 7.8(a) shows the etching height profile for a 1 min etching time with the above-mentioned parameters. A surface profiler (Veeco Dektak 150) was used for such measurement. The depth of etching is measured to be about 640 $\mathring{A}$ or 64 nm. The surface profile along the VO_2 serpentine beam is shown in Fig. 7.8(b). The stylus tip (radius 12.5 μm) of surface profiler is much wider than VO_2 beam spacing (2-10 μm) which leads to erroneous depth profile measurement. However, the profile is still indicative of the surface height after etching process. Fig. 7.8(c) shows two more VO_2 beam structures after the dry etching demonstrating VO_2 beams with different lengths and widths.

7.4 Final Device

Some microscopic images of the final proof-of-concept device are shown in Fig. 7.9. The bright colored shapes indicate the gold layer of 100 nm thickness which includes large gold pads of 1 mm sides and circular top layer patches of different diameters ranging from 1.6

μm to 5 μm. The outline of the second SiO_2 layer is visible along the inner edges of the gold pads. The mask is designed in such a way so that the second SiO_2 layer overlaps a small portion of the pads to avoid unintended shorts along the serpentine beams due to mask alignment errors. The VO_2 beams underneath the gold patches and second SiO_2 layer are visible (bluish tone) confirming the creation of buried VO_2 beams within the MIM absorbers.

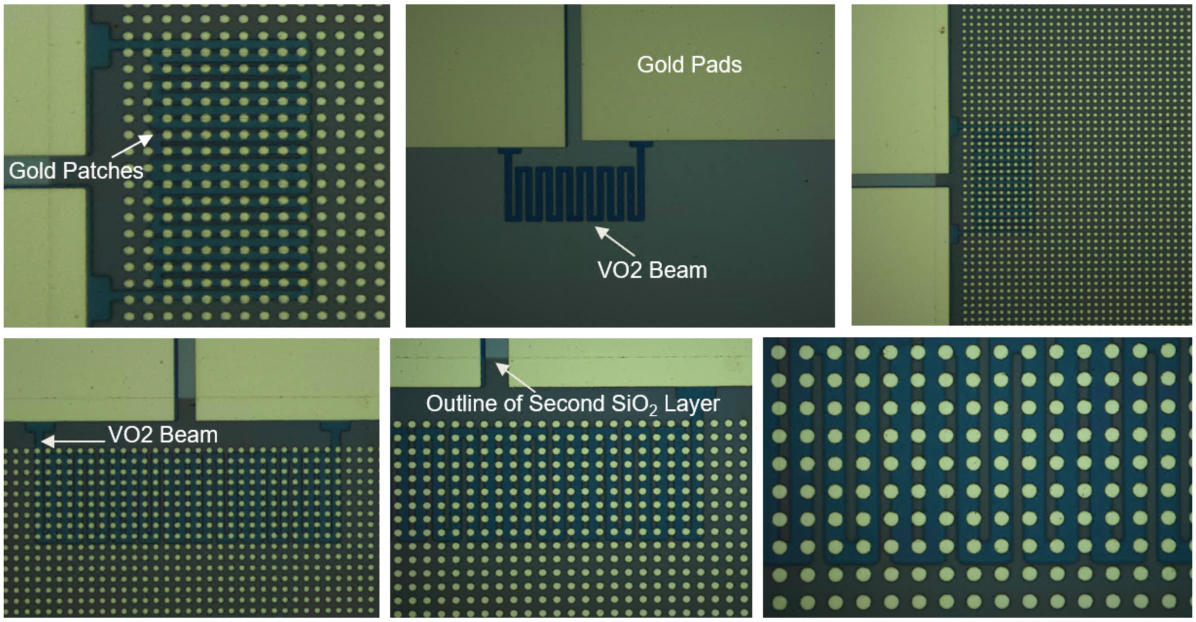

Figure 7.9: Microscopic images of final fabricated proof-of concept device showing top gold patches (circular shapes), gold pads, VO_2 beams underneath the plasmonic absorber patches, exposed VO_2 beams, etc.

7.5 Spectroscopy of Plasmonic Absorber

This section presents the spectroscopic absorption profile of the plasmonic absorbers with circular patches in the proof-of-concept device which follows a similar design as proposed in chapter 5. The absorption profile is experimentally measured by Cary-7000 Universal Measurement Spectrophotometer. Sample absorbers with three different sizes of metal patches were fabricated to measure the absorption profile up to the maximum wavelength of the measuring tool (2.5 μm). The numerically calculated results obtained from COMSOL Multiphysics (3D FEM) are also appended for comparison. The observed discrepancy between simulated and experimental absorption profile can be attributed to fabrication induced variations, measurement equipment noise, and baseline correction. Additionally, the negative absorptance is not practical and a result of baseline correction. The spectroscopic measurement shows the expected plasmonic resonant absorption of a particular range of wavelengths which is needed for selective and efficient detection of infrared radiation.

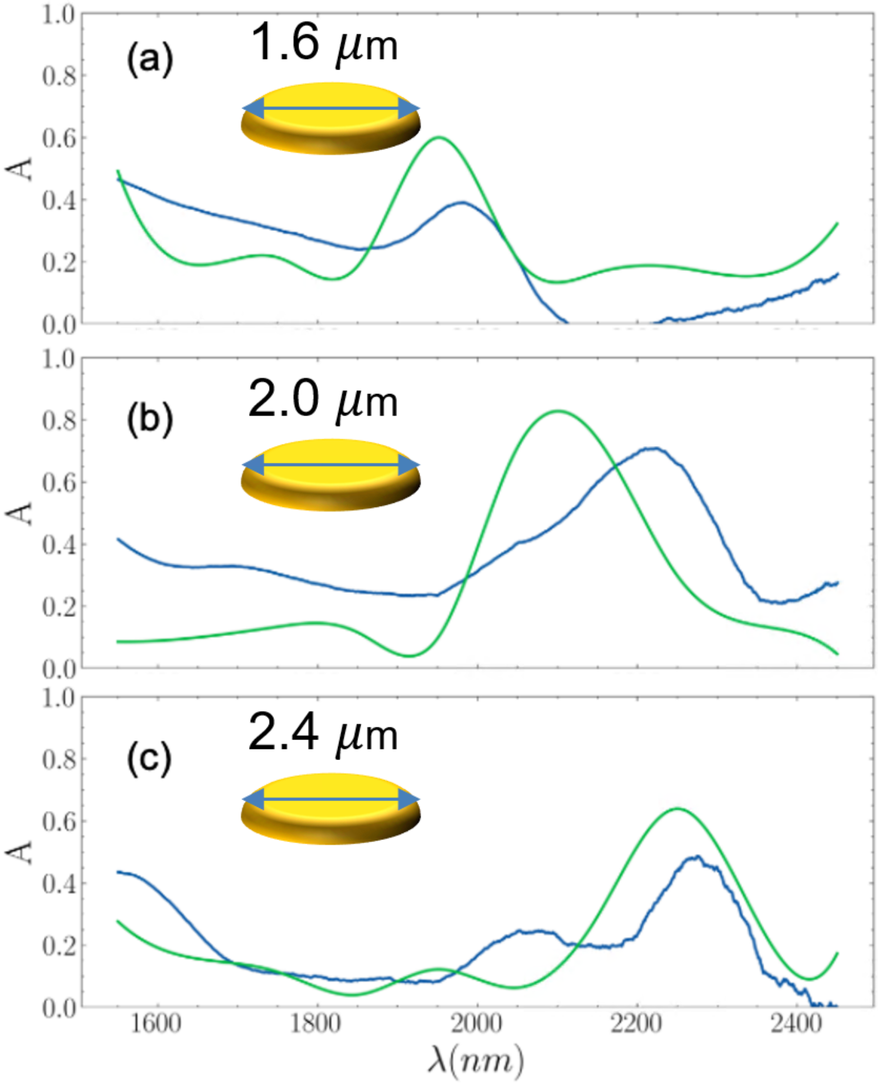

Figure 7.10: Absorption profile of the MIM plasmonic absorber in proof-of-concept device with 3 different sizes - (a) 1.6 μm, (b) 2 μm, (c) 2.4 μm of top metal patches (blue - experimental, green - simulated).

7.6 Electronic Probing

Semiconducting VO_2 material has a temperature coefficient of resistance (TCR) of about 3 K^{-1} [40, 76]. Whereas, at phase transition, the TCR is about 200 K^{-1} [40, 76]. Despite such pronounced sensitivity and large TCR, most VO_2-incorporated sensors and bolometers are operated outside the transition region. The transition-edge behavior of VO_2 still remains debated, unexplored, and unexploited. In addition, the hysteretic phase transition adds to the challenges in operating a VO_2 device at transition. To exploit the large TCR of VO_2 and extract highest-possible sensitivity from the implemented sensor or devices, the device should be operated near phase transition.

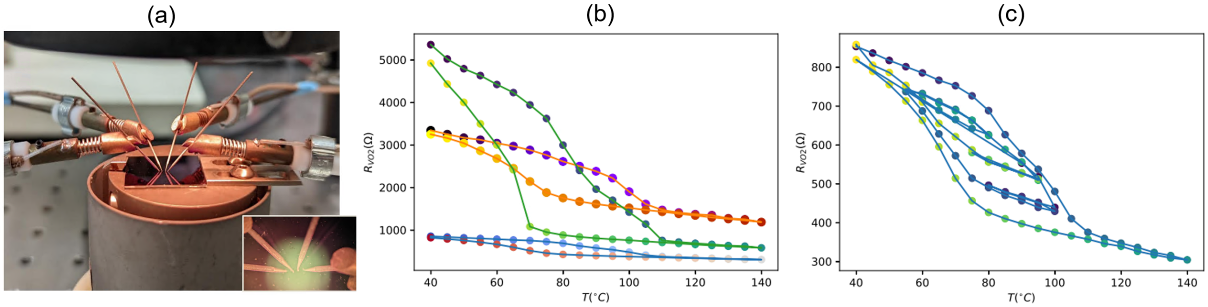

Figure 7.11: (a) Temperature-dependent electronic resistance measurement with a sample on a hot-plate; inset on the bottom-right shows probes touching the sample film (b) Resistance vs. temperature at three different locations on the sample (c) Resistance measurement over multiple temperature cycles near the phase transition point. Micro-hysteresis loops are observed.

It is important to note here that the transition-edge properties of VO_2 is crucial for transition-edge operations as proposed in this work. Temperature-dependent resistivity measurements were conducted for electronic characterization using microscopic probes on a proof-of-concept sample placed in a hot-plate as shown in Fig. 7.11 (a). Resistances at three different locations of a sample are plotted in Fig. 7.11 (b). The color progression follows the sample sequence which follows the thermal cycle of the experiment. To evaluate the transition-edge properties, we measure the electronic resistance of deposited VO_2 film over multiple thermal cycles near the VO_2 transition temperature. Result for one example measurement is presented in Fig.

7.11(c). Multiple micro-hysteresis loops are observed at the transition edge which is expected [124, 76].

Nanostructures of VO_2 hold the potential to further engineer the phase transition behavior. Many studies have been carried out to investigate the size dependence of the semiconductor-to-metal transition of VO_2 nanobeams [152, 153, 154, 155] fabricated by vapor transport or vapor deposition method. However, the report on etched VO_2 nanobeams is limited. Here, we present the temperature-dependent electronic resistivity measurement of the buried VO_2 beams fabricated on the proof-of-concept device by dry etching. The sample is placed on a hot plate. Signatone SE-20BCB probe tips of 125 μm were gently placed on the measurement pads of the sample with the help of a microscope and Signatone S-725 micropositioners. The probe tips were connected to a digital multimeter to collect the temperature dependent resistance of the VO_2 beams.

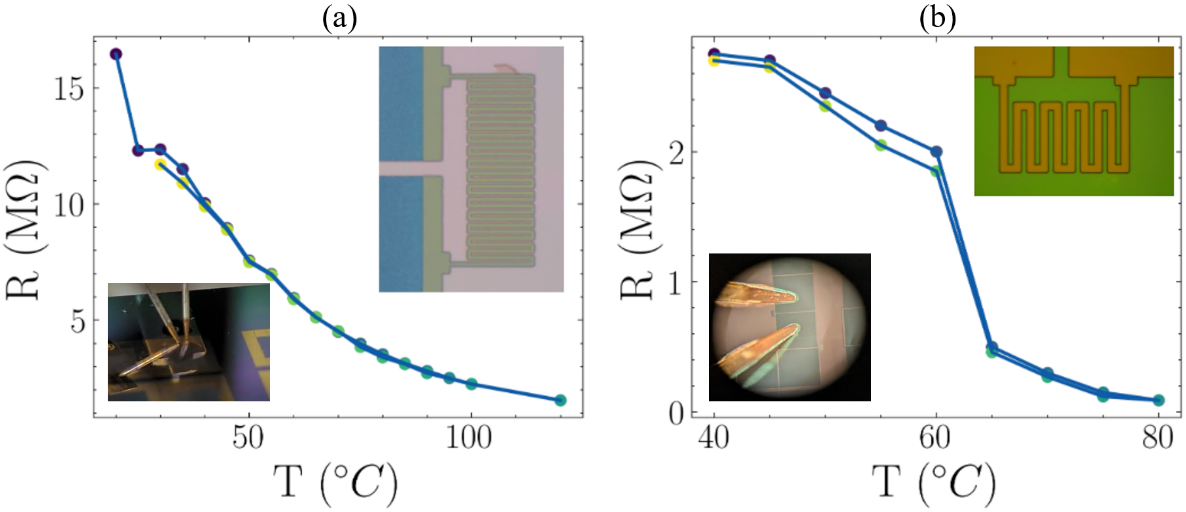

Figure 7.12: Resistance with respect to temperature for two different VO_2 beams (a) 4 μm wide, 50 nm thick, 600 μm long and (b) 8 μm wide, 50 nm thick, 1500 μm long

The results from electronic probe measurements presented in Fig. 7.12 thus confirm the phase-transition and high-TCR of VO_2 beams. Narrower beams are observed to have lower transition temperature but broader transition range. Overall, compared to a VO_2 film, the hysteresis of the phase transition in VO_2 beams is observed be narrower, whereas the transition happens over a longer range of temperature. Additionally, the magnitude of resistance variation is observed to change based on the dimension and aspect ratio of length to width of the beams [93]. Further study on the structured beams of phase transition materials will be of significant benefit to advance such sensing technologies.

Chapter 8

Conclusion

In this work, we have studied the integration of plasmonic absorbers with optical waveguides to achieve enhanced plasmo-thermomechanical all-optical radiation detector. In such device, the radiation information is plasmonically converted to heat-induced mechanical deflection of suspended metallic beams. The deflection drives the change in the insertion loss of optical waveguides underneath the beams. The incoming radiation information is thus produced at the output port of the waveguides. As a result, such devices do not need intermediate electronic conversion of the radiation signal which makes it possible to achieve a simpler and efficient integrated photonic chip. Graphene is demonstrated to enhanced the performance of plasmo-thermomechanical radiation detection by means of its strong plasmonic absorption property and high thermal conductivity. Plasmonic absorbers are also studied with phase-transition and high-TCR VO_2 beams to achieve microbolometers with high-sensitivity thermo-electronic detection of radiation. Here, the incident radiation is efficiently converted into thermal energy by plasmonic absorbers. VO_2 beams indicate the temperature change by producing variation in its resistance which is detected by means of electronic readout. The detector shows almost 3× pixel density and 5× thermal resolution at 10 μm LWIR wavelength when compared to recent reports on microbolometers. Such integration is further demonstrated to be scalable and applicable for far infrared spectrum or THz frequencies. A 1.7 THz radiation detector is also presented to be capable of sensing the intensity as well as polarization of the THz radiation without additional components. The development of such uncooled and high-sensitive radiation detectors with high pixel density, and bandwidth remains crucial for various critical applications such as medical imaging, autonomous driving, and military applications. Future work following the dissertation can benefit the fields of high-resolution radiation sensing and imaging by incorporating novel device design integrating nanostructured VO_2 beams and plasmonic enhancement.

Bibliography

[1] Alexander N Grigorenko, Marco Polini, and KS Novoselov. Graphene plasmonics. *Nature photonics*, 6(11):749–758, 2012.

[2] Yang Wang, Tianyi Sun, Trilochan Paudel, Yi Zhang, Zhifeng Ren, and Krzysztof Kempa. Metamaterial-plasmonic absorber structure for high efficiency amorphous silicon solar cells. *Nano letters*, 12(1):440–445, 2012.

[3] Chihhui Wu, Burton Neuner III, Jeremy John, Andrew Milder, Byron Zollars, Steve Savoy, and Gennady Shvets. Metamaterial-based integrated plasmonic absorber/emitter for solar thermo-photovoltaic systems. *Journal of Optics*, 14(2):024005, 2012.

[4] Peiqi Yu, Hua Yang, Xifang Chen, Zao Yi, Weitang Yao, Jiafu Chen, Yougen Yi, and Pinghui Wu. Ultra-wideband solar absorber based on refractory titanium metal. *Renewable Energy*, 158:227–235, 2020.

[5] Meiyan Pan, Yun Huang, Qiang Li, Hao Luo, Huanzheng Zhu, Sandeep Kaur, and Min Qiu. Multi-band middle-infrared-compatible camouflage with thermal management via simple photonic structures. *Nano Energy*, 69:104449, 2020.

[6] Gustav Edman Jonsson, Vladimir Miljkovic, and Alexandre Dmitriev. Nanoplasmon-enabled macroscopic thermal management. *Scientific reports*, 4(1):5111, 2014.

[7] Na Liu, Martin Mesch, Thomas Weiss, Mario Hentschel, and Harald Giessen. Infrared Perfect Absorber and Its Application As Plasmonic Sensor. *Nano letters*, 10(7):2342–2348, 2010.

[8] Lijun Meng, Ding Zhao, Zhichao Ruan, Qiang Li, Yuanqing Yang, and Min Qiu. Optimized grating as an ultra-narrow band absorber or plasmonic sensor. *Optics letters*, 39(5):1137–1140, 2014.

[9] James Clerk Maxwell. *A treatise on electricity and magnetism*, volume 1. Oxford: Clarendon Press, 1873.

[10] Anatoly V Zayats, Igor I Smolyaninov, and Alexei A Maradudin. Nano-optics of surface plasmon polaritons. *Physics reports*, 408(3-4):131–314, 2005.

[11] Zhanghua Han and Sergey I Bozhevolnyi. Radiation guiding with surface plasmon polaritons. *Reports on Progress in Physics*, 76(1):016402, 2012.

[12] Xin Guo, Yaoguang Ma, Yipei Wang, and Limin Tong. Nanowire plasmonic waveguides, circuits and devices. *Laser & Photonics Reviews*, 7(6):855–881, 2013.

[13] Rupert F Oulton, Volker J Sorger, DA Genov, DFP Pile, and X Zhang. A hybrid plasmonic waveguide for subwavelength confinement and long-range propagation. *nature photonics*, 2(8):496–500, 2008.

[14] Anatoly V Zayats and Igor I Smolyaninov. Near-field photonics: surface plasmon polaritons and localized surface plasmons. *Journal of Optics A: Pure and Applied Optics*, 5(4):S16, 2003.

[15] Wen-Hung Chuang, Jyh-Yang Wang, CC Yang, and Yean-Woei Kiang. Differentiating the contributions between localized surface plasmon and surface plasmon polariton on a one-dimensional metal grating in coupling with a light emitter. *Applied Physics Letters*, 92(13):133115, 2008.

[16] Shinpei Ogawa and Masafumi Kimata. Metal-Insulator-Metal-Based Plasmonic Metamaterial Absorbers at Visible and Infrared Wavelengths: A Review. *Materials*, 11(3), March 2018.

[17] Min Yan. Metal–insulator–metal light absorber: a continuous structure. *Journal of Optics*, 15(2):025006, 2013.

[18] Antoni Rogalski, Jarek Antoszewski, and Lorenzo Faraone. Third-generation infrared photodetector arrays. *Journal of Applied Physics*, 105(9):091101–NA, 2009.

[19] Simone Bianconi and Hooman Mohseni. Recent Advances in Infrared Imagers: Toward Thermodynamic and Quantum Limits of Photon Sensitivity. *Reports on progress in physics. Physical Society (Great Britain)*, 83(4):044101–044101, 2020.

[20] A. Rogalski. Recent progress in infrared detector technologies. *Infrared Physics & Technology*, 54(3):136–154, May 2011.

[21] Ibrahim Kimukin, Necmi Biyikli, Tolga Kartaloglu, O Aytur, and Ekmel Ozbay. High-speed insb photodetectors on gaas for mid-ir applications. *IEEE Journal of selected topics in quantum electronics*, 10(4):766–770, 2004.

[22] Sarath D Gunapala, SV Bundara, John K Liu, Winn Hong, Mani Sundaram, Paul D Maker, Richard E Muller, Craig A Shott, and Ronald Carralejo. Long-wavelength 640/spl times/486 gaas-algaas quantum well infrared photodetector snap-shot camera. *IEEE Transactions on Electron Devices*, 45(9):1890–1895, 1998.

[23] Daniele Palaferri, Yanko Todorov, Azzurra Bigioli, Alireza Mottaghizadeh, Djamal Gacemi, Allegra Calabrese, Angela Vasanelli, Lianhe Li, A Giles Davies, Edmund H Linfield, et al. Room-temperature nine-µm-wavelength photodetectors and GHz-frequency heterodyne receivers. *Nature*, 556(7699):85–88, 2018.

[24] Chee Leong Tan and Hooman Mohseni. Emerging technologies for high performance infrared detectors. *Nanophotonics*, 7(1):169–197, January 2018.

[25] R McClintock, JL Pau, K Minder, C Bayram, P Kung, and M Razeghi. Hole-initiated multiplication in back-illuminated GaN avalanche photodiodes. *Applied Physics Letters*, 90(14):141112–NA, 2007.

[26] Ozdal Boyraz and Bahram Jalali. Demonstration of a silicon Raman laser. *Optics express*, 12(21):5269–5273, 2004.

[27] Valentina Donzella, Ahmed Sherwali, Jonas Flueckiger, Sahba Talebi Fard, Samantha M Grist, and Lukas Chrostowski. Sub-wavelength grating components for integrated optics applications on SOI chips. *Optics express*, 22(17):21037–21050, 2014.

[28] Qiancheng Zhao, Mohammad Wahiduzzaman Khan, Shiva Farzinazar, Jaeho Lee, and Ozdal Boyraz. Plasmo-thermomechanical radiation detector with on-chip optical readout. *Optics Express*, 26(23):29638, November 2018.

[29] Mohammad Wahiduzzaman Khan, Parinaz Sadri-Moshkenani, Md Shafiqul Islam, and Ozdal Boyraz. Graphene-coated suspended metallic nanostructures for fast and sensitive optomechanical infrared detection. In *CLEO: Science and Innovations*, pages JTu2A–51. Optical Society of America, 2019.

[30] Mohammad Wahiduzzaman Khan, Qiancheng Zhao, Parinaz Sadri-Moshkenani, Md Shafiqul Islam, and Ozdal Boyraz. Graphene-incorporated plasmo-thermomechanical infrared radiation detection. *Journal of the Optical Society of America B*, 37(3):774–783, 2020.

[31] Frank Niklaus, Christian Vieider, and Henrik Jakobsen. Mems-based uncooled infrared bolometer arrays: a review. *MEMS/MOEMS technologies and applications III*, 6836:125–139, 2008.

[32] Jin-Shown Shie, Yeong-Maw Chen, Mang Ou-Yang, and Bruce CS Chou. Characterization and modeling of metal-film microbolometer. *Journal of Microelectromechanical systems*, 5(4):298–306, 1996.

[33] X Gu, G Karunasiri, G Chen, U Sridhar, and B Xu. Determination of thermal parameters of microbolometers using a single electrical measurement. *Applied Physics Letters*, 72(15):1881–1883, 1998.

[34] R Andrew Wood. Uncooled thermal imaging with monolithic silicon focal planes. In *Infrared Technology XIX*, volume 2020, pages 322–329. Spie, 1993.

[35] A Basantani Hitesh, Hang Beum Shin, Thomas Nelson Jackson, and Mark William Horn. Vertically integrated pixel microbolometers for ir imaging using high resistivity vox. In *39th Infrared Technology and Applications*, page 87041A, 2013.

[36] Bin Wang, Jianjun Lai, Hui Li, Haoming Hu, and Sihai Chen. Nanostructured vanadium oxide thin film with high TCR at room temperature for microbolometer. *Infrared Physics & Technology*, 57(NA):8–13, 2013.

[37] HS Choi, JS Ahn, JH Jung, TW Noh, and DH Kim. Mid-infrared properties of a VO 2 film near the metal-insulator transition. *Physical review. B, Condensed matter*, 54(7):4621–4628, 1996.

[38] Nicolas Émond, Ali Hendaoui, and Mohamed Chaker. Low resistivity wxv1- xo2-based multilayer structure with high temperature coefficient of resistance for microbolometer applications. *Applied Physics Letters*, 107(14):143507, 2015.

[39] Carl D Reintsema, Erich N Grossman, and Jonathan A Koch. Improved VO2 microbolometers for infrared imaging: operation on the semiconducting-metallic phase transition with negative electrothermal feedback. *SPIE Proceedings*, 3698(NA):190–200, 1999.

[40] Luiz Alberto Luz de Almeida, Gurdip Singh Deep, Antonio Marcus Nogueira Lima, and Helmut Neff. Modeling of the hysteretic metal-insulator transition in a vanadium dioxide infrared detector. *Optical Engineering*, 41(10):2582–2588, 2002.

[41] Sihai Chen, Hong Ma, Sihua Xiang, and Xinjian Yi. Fabrication and performance of microbolometer arrays based on nanostructured vanadium oxide thin films. *Smart Materials and Structures*, 16(3):696–700, 2007.

[42] Jun Gou, Jun Wang, Xing Zheng, Deen Gu, He Yu, and Yadong Jiang. Detection of terahertz radiation from 2.52 THz CO2 laser using a 320 × 240 vanadium oxide microbolometer focal plane array. *RSC Advances*, 5(102):84252–84256, 2015.

[43] Thang Duy Dao, Anh Tung Doan, Satoshi Ishii, Takahiro Yokoyama, Handegård Sele Ørjan, Dang Hai Ngo, Tomoko Ohki, Akihiko Ohi, Yoshiki Wada, Chisato Niikura, et al. MEMS-Based Wavelength-Selective Bolometers. *Micromachines*, 10(6):416–NA, 2019.

[44] Evan Smith. Vanadium oxide microbolometers with patterned gold black or plasmonic resonant absorbers. 2015.

[45] Elizabeth E. Chain. Optical properties of vanadium dioxide and vanadium pentoxide thin films. *Applied optics*, 30(19):2782–2787, 1991.

[46] CH Griffiths and HK Eastwood. Influence of stoichiometry on the metal-semiconductor transition in vanadium dioxide. *Journal of Applied Physics*, 45(5):2201–2206, 1974.

[47] E Kusano, JA Theil, and John A Thornton. Deposition of vanadium oxide films by direct-current magnetron reactive sputtering. *Journal of Vacuum Science & Technology A: Vacuum, Surfaces, and Films*, 6(3):1663–1667, 1988.

[48] Ping Jin Ping Jin and Sakae Tanemura Sakae Tanemura. Formation and Thermochromism of VO2 Films Deposited by RF Magnetron Sputtering at Low Substrate Temperature. *Japanese Journal of Applied Physics*, 33(3):1478–1483, 1994.

[49] Run Shi, Nan Shen, Jingwei Wang, Weijun Wang, Abbas Amini, Ning Wang, and Chun Cheng. Recent advances in fabrication strategies, phase transition modulation, and advanced applications of vanadium dioxide. *Applied Physics Reviews*, 6(1):011312–NA, 2019.

[50] Run Shi, Jingwei Wang, Xiangbin Cai, Linfei Zhang, Pengcheng Chen, Shiyuan Liu, Liang Zhang, Wenkai Ouyang, Ning Wang, and Chun Cheng. Axial Modulation of Metal–Insulator Phase Transition of VO2 Nanowires by Graded Doping Engineering for Optically Readable Thermometers. *The Journal of Physical Chemistry C*, 121(44):24877–24885, 2017.

[51] Semih Korkmaz, Mustafa Turkmen, and Serap Aksu. Mid-infrared narrow band plasmonic perfect absorber for vibrational spectroscopy. *Sensors and Actuators A: Physical*, 301(NA):111757–NA, 2020.

[52] Shaohua Wang, Yufei Wang, Siriguleng Zhang, and Wanhua Zheng. Mid-infrared broadband absorber of full semiconductor epi-layers. *Physics Letters A*, 381(16):1439–1444, 2017.

[53] Leland Nordin, Abhilasha Kamboj, Priyanka Petluru, Eric Shaner, and Daniel Wasserman. All-Epitaxial Integration of Long-Wavelength Infrared Plasmonic Materials and Detectors for Enhanced Responsivity. *ACS Photonics*, 7(8):1950–1956, 2020.

[54] Shinpei Ogawa, Junya Komoda, Kyohei Masuda, and Masafumi Kimata. Wavelength selective wideband uncooled infrared sensor using a two-dimensional plasmonic absorber. *Optical Engineering*, 52(12):127104–127104, 2013.

[55] Antoni Rogalski. *Infrared Detectors, Second Edition - Infrared Detectors, Second Edition*, volume NA. 2010. Issue: NA Pages: NA Publication Title: NA.

[56] SG Burnay, TL Williams, and Colin Hywel Jones. *Applications of thermal imaging.* CRC Press, 1988.

[57] R Clark Jones. Performance of detectors for visible and infrared radiation. *Advances in Electronics and Electron Physics*, 5:1–96, 1953.

[58] Antonio Rogalski. *Infrared detectors.* CRC press, 2000.

[59] Yuan Liu, Rui Cheng, Lei Liao, Hailong Zhou, Jingwei Bai, Gang Liu, Lixin Liu, Yu Huang, and Xiangfeng Duan. Plasmon resonance enhanced multicolour photodetection by graphene. *Nature Communications*, 2:579, December 2011.

[60] T. J. Echtermeyer, L. Britnell, P. K. Jasnos, A. Lombardo, R. V. Gorbachev, A. N. Grigorenko, A. K. Geim, A. C. Ferrari, and K. S. Novoselov. Strong plasmonic enhancement of photovoltage in graphene. *Nature Communications*, 2:458, August 2011.

[61] Mahdieh Hashemi, Mahmood Hosseini Farzad, N. Asger Mortensen, and Sanshui Xiao. Enhanced absorption of graphene in the visible region by use of plasmonic nanostructures. *Journal of Optics*, 15(5):055003, 2013.

[62] Ming Liu, Xiaobo Yin, Erick Ulin-Avila, Baisong Geng, Thomas Zentgraf, Long Ju, Feng Wang, and Xiang Zhang. A graphene-based broadband optical modulator. *Nature*, 474(7349):64–67, June 2011.

[63] Alexander A. Balandin, Suchismita Ghosh, Wenzhong Bao, Irene Calizo, Desalegne Teweldebrhan, Feng Miao, and Chun Ning Lau. Superior Thermal Conductivity of Single-Layer Graphene. *Nano Letters*, 8(3):902–907, March 2008.

[64] Wenyi Wang, Andrey Klots, Yuanmu Yang, Wei Li, Ivan I Kravchenko, Dayrl P Briggs, Kirill I Bolotin, and Jason Valentine. Enhanced absorption in two-dimensional materials via fano-resonant photonic crystals. *Applied Physics Letters*, 106(18):181104, 2015.

[65] Semih Cakmakyapan, Ping Keng Lu, Aryan Navabi, and Mona Jarrahi. Gold-patched graphene nano-stripes for high-responsivity and ultrafast photodetection from the visible to infrared regime. *Light: Science & Applications*, 7(1):20, 2018.

[66] L. A. Falkovsky and S. S. Pershoguba. Optical far-infrared properties of a graphene monolayer and multilayer. *Physical Review B*, 76(15):153410, October 2007.

[67] Jianing Chen, Pablo Albella, Zhaleh Pirzadeh, Pablo Alonso-González, Florian Huth, Stefano Bonetti, Valentina Bonanni, Johan Åkerman, Josep Nogués, Paolo Vavassori, Alexandre Dmitriev, Javier Aizpurua, and Rainer Hillenbrand. Plasmonic Nickel Nanoantennas. *Small*, 7(16):2341–2347, August 2011.

[68] Liu Cui, Sanqiang Shi, Zhao Li, Gaosheng Wei, and Xiaoze Du. Manipulating Thermal Conductance of Supported Graphene via Surface Hydroxylation of Substrates. *The Journal of Physical Chemistry C*, 122(48):27689–27695, December 2018.

[69] Z. Gao, Y. Zhang, Y. Fu, M. Yuen, and J. Liu. Graphene heat spreader for thermal management of hot spots. In *2013 IEEE 63rd Electronic Components and Technology Conference*, pages 2075–2078, May 2013.

[70] G. Chen, C. L. Tien, X. Wu, and J. S. Smith. Thermal Diffusivity Measurement of GaAs/AlGaAs Thin-Film Structures. *Journal of Heat Transfer*, 116(2):325–331, May 1994.

[71] Jerome G Hust and Patricia J Giarratano. *Thermal Conductivity and Electrical Resistivity: Standard Reference Materials–tungsten SRM's 730 and 799, from 4 to 3000K*, volume 260. US Department of Commerce, National Bureau of Standards, 1975.

[72] Yuan Shiping and Jiang Peixue. Thermal conductivity of nanoscale thin nickel films. *Progress in Natural Science*, 15(10):922–929, October 2005.

[73] Seth Calhoun, Sara Demonaco, Chad Spence, Robert E Peale, Evan Smith, Shiva Vangala, and Justin W Cleary. Multispectral Plasmonic Perfect Absorbers Integrated with Room-Temperature VO x Air-Bridge Bolometers. *2019 IEEE Research and Applications of Photonics in Defense Conference (RAPID)*, NA(NA):NA–NA, 2019.

[74] Rachel N Evans, Seth R Calhoun, Jonathan R Brescia, Justin W Cleary, Evan M Smith, and Robert E Peale. Far-infrared bands in plasmonic metal-insulator-metal absorbers optimized for long-wave infrared. *MRS Advances*, 4(11):667–674, 2019.

[75] Evan M Smith, James C Ginn, Andrew P Warren, Christopher J Long, Deep Panjwani, Robert E Peale, and David J Shelton. Linear bolometer array using a high TCR VOx-Au film. *SPIE Proceedings*, 9070(NA):589–596, 2014.

[76] LAL De Almeida, GS Deep, AMN Lima, IA Khrebtov, VG Malyarov, and H Neff. Modeling and performance of vanadium-oxide transition edge microbolometers. *Applied Physics Letters*, 85(16):3605–3607, 2004.

[77] Amr Shebl Ahmed, Hye Jin Kim, Jinsik Kim, Kyo Seon Hwang, and Seonghwan Kim. Enhancing the Responsivity of Uncooled Infrared Detectors Using Plasmonics for High-Performance Infrared Spectroscopy. *Sensors (Basel, Switzerland)*, 17(4):908–NA, 2017.

[78] VI Belotelov, IA Akimov, M Pohl, VA Kotov, S Kasture, AS Vengurlekar, Achanta Venu Gopal, DR Yakovlev, AK Zvezdin, and M Bayer. Enhanced magneto-optical effects in magnetoplasmonic crystals. *Nature nanotechnology*, 6(6):370–376, 2011.

[79] Cheng-Wen Cheng, Mohammed Nadhim Abbas, Chao-Wei Chiu, Kun-Ting Lai, Min-Hsiung Shih, and Yia-Chung Chang. Wide-angle polarization independent infrared broadband absorbers based on metallic multi-sized disk arrays. *Optics express*, 20(9):10376–10381, 2012.

[80] Ahasanul Haque, Monir Morshed, Ziyuan Li, Kaushal Vora, Li Li, Andrey Miroshnichenko, and Haroldo T Hattori. Broadband and thermally stable tungsten boride absorber. *Journal of the Optical Society of America B*, 36(10):2744–2749, 2019.

[81] Justin W Cleary, Robert E Peale, Evan Smith, and Janardan Nath. Wavelength-selective thermal detection apparatus and methods, October 16 2018. US Patent 10,101,212.

[82] Mohammad Wahiduzzaman Khan, Parinaz Sadri-Moshkenani, Md Shafiqul Islam, Ozdal Boyraz, Jonathan Sullivan, Ziqi Yu, and Jaeho Lee. Selective and efficient infrared detection by plasmonically heated vanadium-dioxide nanowire. *Plasmonics: Design, Materials, Fabrication, Characterization, and Applications XVIII*, 11462(NA):119–123, 2020.

[83] Omar Alkorjia, Amjed Abdullah, Akshay Koppula, Cameron Warder, Tao Liu, Chuang Qu, Chen Zhu, Edward Kinzel, and Mahmoud Almasri. Metasurface Based Uncooled

Microbolometer with High Fill Factor. *2019 20th International Conference on Solid-State Sensors, Actuators and Microsystems & Eurosensors XXXIII (TRANSDUCERS & EUROSENSORS XXXIII)*, NA(NA):2126–NA, 2019.

[84] O Celik, E Inceturkmen, B Kaplan, B Barutcu, O Aydin, IE Gonenli, R Kepenek, C Tunca, M Akbulut, O Nuzumlali, et al. 640 x 480 17 μm microbolometer uncooled detector development at aselsan, inc. In *Infrared Technology and Applications XLVI*, volume 11407, pages 119–127. SPIE, 2020.

[85] C Baristiran Kaynak, A Goeritz, EC Durmaz, M Wietstruck, E Onat, AS Ozcan, ER Turkoglu, Y Gurbuz, and M Kaynak. Thermo-Mechanical Modeling and Experimental Validation of an Uncooled Microbolometer. *2020 IEEE 20th Topical Meeting on Silicon Monolithic Integrated Circuits in RF Systems (SiRF)*, NA(NA):NA–NA, 2020.

[86] Evan M Smith, Deep Panjwani, James Ginn, Andrew P Warren, Christopher Long, Pedro Figuieredo, Christian Smith, Janardan Nath, Joshua Perlstein, Nick Walter, et al. Dual band sensitivity enhancements of a VO(x) microbolometer array using a patterned gold black absorber. *Applied optics*, 55(8):2071–2078, 2016.

[87] Firat Tankut, Mustafa H Cologlu, Hande Ozturk, Gorkem Cilbir, Orhan S Akar, and Tayfun Akin. A 160x120 LWIR-band CMOS Infrared (CIR) microbolometer. *Infrared Technology and Applications XLV*, 11002(NA):376–385, 2019.

[88] Tsung-Han Yeh, Cheng-Kang Tsai, Shao-Yu Chu, Hsin-Ying Lee, and Ching-Ting Lee. Performance improvement of Y-doped VOx microbolometers with nanomesh antireflection layer. *Optics express*, 28(5):6433–6442, 2020.

[89] Margaret Kohin and Neal R Butler. Performance limits of uncooled VO x microbolometer focal plane arrays. *SPIE Proceedings*, 5406(NA):447–453, 2004.

[90] Takashi Kawakubo and K Komeya. Static and Cyclic Fatigue Behavior of a Sintered Silicon Nitride at Room Temperature. *Journal of the American Ceramic Society*, 70(6):400–405, 1987.

[91] Wen-Hsien Chuang, Rainer K Fettig, and Reza Ghodssi. Nano-scale fatigue study of LPCVD silicon nitride thin films using a mechanical-amplifier actuator. *Journal of Micromechanics and Microengineering*, 17(5):938–944, 2007.

[92] David Benirschke and Scott Howard. Characterization of a low-cost, commercially available, vanadium oxide microbolometer array for spectroscopic imaging. *Optical Engineering*, 56(4):040502–040502, 2017.

[93] Liu Hongwei, Lu Junpeng, Zheng Minrui, Tang Sing Hai, Sow Chorng Haur, Zhang Xinhai, and Ke Lin. Size effects on metal-insulator phase transition in individual vanadium dioxide nanowires. *Optics express*, 22(25):30748–30755, 2014.

[94] Virginie Théry, Alexandre Boulle, Aurelian Crunteanu, Jean-Christophe Orlianges, Arnaud Beaumont, Richard Mayet, Amine Mennai, F Cosset, A Bessaudou, and Marc Fabert. Role of thermal strain in the metal-insulator and structural phase transition of epitaxial VO 2 films. *Physical Review B*, 93(18):184106–NA, 2016.

[95] Jiang Wei, Zenghui Wang, Wei Chen, and David H Cobden. New aspects of the metal–insulator transition in single-domain vanadium dioxide nanobeams. *Nature nanotechnology*, 4(7):420–424, 2009.

[96] Haidan Wen, Lu Guo, Eftihia Barnes, June Hyuk Lee, Donald A Walko, Richard D Schaller, Jarrett A Moyer, Rajiv Misra, Yuelin Li, Eric M Dufresne, et al. Structural and electronic recovery pathways of a photoexcited ultrathin VO 2 film. *Physical Review B*, 88(16):165424–NA, 2013.

[97] Junqiao Wu, Qian Gu, Beth S Guiton, Nathalie P De Leon, Lian Ouyang, and Hongkun Park. Strain-induced self organization of metal-insulator domains in single-crystalline VO2 nanobeams. *Nano letters*, 6(10):2313–2317, 2006.

[98] Chun Cheng, Kai Liu, Bin Xiang, Joonki Suh, and Junqiao Wu. Ultra-long, free-standing, single-crystalline vanadium dioxide micro/nanowires grown by simple thermal evaporation. *Applied Physics Letters*, 100(10):103111–NA, 2012.

[99] Beth S Guiton, Qian Gu, Amy L Prieto, Mark S Gudiksen, and Hongkun Park. Single-crystalline vanadium dioxide nanowires with rectangular cross sections. *Journal of the American Chemical Society*, 127(2):498–499, 2004.

[100] Servin Rathi, Jin-Hyung Park, In-yeal Lee, Jeong Min Baik, Kyung Soo Yi, and Gil-Ho Kim. Unravelling the switching mechanisms in electric field induced insulator–metal transitions in VO2 nanobeams. *Journal of Physics D: Applied Physics*, 47(29):295101–NA, 2014.

[101] Taehoon Lee, Alexander Efremov, Yong-Hyun Ham, Sun Jin Yun, Nam-Ki Min, Munpyo Hong, and Kwang-Ho Kwon. Etching characteristics and mechanism of vanadium dioxide in inductively coupled Cl2/Ar plasma. *Journal of Micro/Nanolithography, MEMS, and MOEMS*, 8(2):021110–NA, 2009.

[102] Francisco Javier González, Javier Alda, Jorge Simón, James Ginn, and Glenn Boreman. The effect of metal dispersion on the resonance of antennas at infrared frequencies. *Infrared Physics & Technology*, 52(1):48–51, 2009.

[103] Paul D Cunningham, Nestor N Valdes, Felipe A Vallejo, L Michael Hayden, Brent Polishak, Xing-Hua Zhou, Jingdong Luo, Alex K-Y Jen, Jarrod C Williams, and Robert J Twieg. Broadband terahertz characterization of the refractive index and absorption of some important polymeric and organic electro-optic materials. *Journal of applied physics*, 109(4):043505–043505, 2011.

[104] Federico Sanjuan and Jorge O Tocho. Optical properties of silicon, sapphire, silica and glass in the terahertz range. In *Latin America Optics and Photonics Conference*, pages LT4C–1. Optica Publishing Group, 2012.

[105] Fang Ling, Zheqiang Zhong, Renshuai Huang, and Bin Zhang. A broadband tunable terahertz negative refractive index metamaterial. *Scientific reports*, 8(1):9843, 2018.

[106] Evan Smith. Vanadium oxide microbolometers with patterned gold black or plasmonic resonant absorbers. 2015.

[107] Mohammad Wahiduzzaman Khan, Jonathan Matthew Sullivan, Jaeho Lee, and Ozdal Boyraz. High sensitivity long-wave infrared detector design based on integrated plasmonic absorber and vo_2 nanobeam. *IEEE Journal of Quantum Electronics*, 57(4):1–11, 2021.

[108] Mohammad Wahiduzzaman Khan, Parinaz Sadri-Moshkenani, Md Shafiqul Islam, Ozdal Boyraz, Jonathan Sullivan, Ziqi Yu, and Jaeho Lee. Selective and efficient infrared detection by plasmonically heated vanadium-dioxide nanowire. In *Plasmonics: Design, Materials, Fabrication, Characterization, and Applications XVIII*, volume 11462, pages 119–123. SPIE, 2020.

[109] Zewei Shao, Xun Cao, Hongjie Luo, and Ping Jin. Recent progress in the phase-transition mechanism and modulation of vanadium dioxide materials. *NPG Asia Materials*, 10(7):581–605, 2018.

[110] Yuanjie Xu, Wanxia Huang, Qiwu Shi, Yang Zhang, Linwei Song, and Yaxin Zhang. Synthesis and properties of mo and w ions co-doped porous nano-structured vo 2 films by sol–gel process. *Journal of sol-gel science and technology*, 64:493–499, 2012.

[111] Yanfei Wu, Lele Fan, Qinghua Liu, Shi Chen, Weifeng Huang, Feihu Chen, Guangming Liao, Chongwen Zou, and Ziyu Wu. Decoupling the lattice distortion and charge doping effects on the phase transition behavior of vo2 by titanium (ti4+) doping. *Scientific reports*, 5(1):9328, 2015.

[112] Keisuke Shibuya, Masashi Kawasaki, and Yoshinori Tokura. Metal-insulator transition in epitaxial $v_{1-x}w_xo_2$ $(0 \leq x \leq 0.33)$ thin films. *Applied Physics Letters*, 96(2):022102, 2010.

[113] Qiancheng Zhao, Mohammad Wahiduzzaman Khan, Shiva Farzinazar, Jaeho Lee, and Ozdal Boyraz. Plasmo-thermomechanical radiation detector with on-chip optical readout. *Optics express*, 26(23):29638–29650, 2018.

[114] Qiancheng Zhao, Mohammad Wahiduzzaman Khan, Parinaz Sadri-Moshkenani, Regina Regan, Filippo Capolino, and Ozdal Boyraz. Demonstration of a plasmo-thermomechanical radiation detector with si3n4 waveguide optical readout circuit. In *CLEO: Science and Innovations*, pages JW2A–175. Optica Publishing Group, 2018.

[115] Qiancheng Zhao, Parinaz Sadri-Moshkenani, Mohammad Wahiduzzaman Khan, Rasul Torun, and Ozdal Boyraz. On-chip bimetallic plasmo-thermomechanical detectors for mid-infrared radiation. *IEEE Photonics Technology Letters*, 29(17):1459–1462, 2017.

[116] Takashi Kawakubo and K Komeya. Static and cyclic fatigue behavior of a sintered silicon nitride at room temperature. *Journal of the American Ceramic Society*, 70(6):400–405, 1987.

[117] Wen-Hsien Chuang, Rainer K Fettig, and Reza Ghodssi. Nano-scale fatigue study of lpcvd silicon nitride thin films using a mechanical-amplifier actuator. *Journal of Micromechanics and Microengineering*, 17(5):938, 2007.

[118] Nick CJ Van der Valk, Willemine AM van der Marel, and Paul CM Planken. Terahertz polarization imaging. *Optics letters*, 30(20):2802–2804, 2005.

[119] Stefan Katletz, Michael Pfleger, Harald Pühringer, Martin Mikulics, Nico Vieweg, Ole Peters, Benedikt Scherger, Maik Scheller, Martin Koch, and Karin Wiesauer. Polarization sensitive terahertz imaging: detection of birefringence and optical axis. *Optics Express*, 20(21):23025–23035, 2012.

[120] Virginie Théry, Alexandre Boulle, Aurelian Crunteanu, Jean-Christophe Orlianges, Arnaud Beaumont, Richard Mayet, Amine Mennai, F Cosset, A Bessaudou, and Marc Fabert. Role of thermal strain in the metal-insulator and structural phase transition of epitaxial vo 2 films. *Physical Review B*, 93(18):184106, 2016.

[121] LAL De Almeida, GS Deep, AMN Lima, IA Khrebtov, VG Malyarov, and H Neff. Modeling and performance of vanadium–oxide transition edge microbolometers. *Applied Physics Letters*, 85(16):3605–3607, 2004.

[122] Sihai Chen, Hong Ma, Sihua Xiang, and Xinjian Yi. Fabrication and performance of microbolometer arrays based on nanostructured vanadium oxide thin films. *Smart materials and structures*, 16(3):696, 2007.

[123] Carl D Reintsema, Erich N Grossman, and Jonathan A Koch. Improved vo2 microbolometers for infrared imaging: operation on the semiconducting-metallic phase transition with negative electrothermal feedback. In *Infrared technology and applications XXV*, volume 3698, pages 190–200. SPIE, 1999.

[124] Luiz Alberto Luz de Almeida, Gurdip Singh Deep, Antonio Marcus Nogueira Lima, and Helmut Neff. Modeling of the hysteretic metal-insulator transition in a vanadium dioxide infrared detector. *Optical Engineering*, 41(10):2582–2588, 2002.

[125] M Romano, A Chulkov, A Sommier, D Balageas, V Vavilov, JC Batsale, and Christophe Pradere. Broadband sub-terahertz camera based on photothermal conversion and ir thermography. *Journal of Infrared, Millimeter, and Terahertz Waves*, 37:448–461, 2016.

[126] Naoki Oda, Seiji Kurashina, Masaru Miyoshi, Kohei Doi, Tsutomu Ishi, Takayuki Sudou, Takao Morimoto, Hideki Goto, and Tokuhito Sasaki. Microbolometer terahertz focal plane array and camera with improved sensitivity in the sub-terahertz region. *Journal of Infrared, Millimeter, and Terahertz Waves*, 36:947–960, 2015.

[127] Leonardo Vicarelli, Alessandro Tredicucci, and Alessandro Pitanti. Micromechanical bolometers for subterahertz detection at room temperature. *ACS photonics*, 9(2):360–367, 2022.

[128] Denis Dufour, Linda Marchese, Marc Terroux, Hassane Oulachgar, Francis Généreux, Michel Doucet, Luc Mercier, Bruno Tremblay, Christine Alain, Patrick Beaupré, et al. Review of terahertz technology development at ino. *Journal of Infrared, Millimeter, and Terahertz Waves*, 36:922–946, 2015.

[129] Dogeun Jang, Malik Kimbrue, Yung-Jun Yoo, and Ki-Yong Kim. Spectral characterization of a microbolometer focal plane array at terahertz frequencies. *IEEE Transactions on Terahertz Science and Technology*, 9(2):150–154, 2019.

[130] François Simoens and Jérôme Meilhan. Terahertz real-time imaging uncooled array based on antenna-and cavity-coupled bolometers. *Philosophical Transactions of the Royal Society A: Mathematical, Physical and Engineering Sciences*, 372(2012):20130111, 2014.

[131] Marcelo SB de Castro, Carlos L Ferreira, and Roberto R de Avillez. Vanadium oxide thin films produced by magnetron sputtering from a v2o5 target at room temperature. *Infrared Physics & Technology*, 60:103–107, 2013.

[132] EN Fuls, DH Hensler, and AR Ross. Reactively sputtered vanadium dioxide thin films. *Applied Physics Letters*, 10(7):199–201, 1967.

[133] RT Kivaisi and M Samiji. Optical and electrical properties of vanadium dioxide films prepared under optimized rf sputtering conditions. *Solar Energy Materials and Solar Cells*, 57(2):141–152, 1999.

[134] DH Kim and Hoi Sing Kwok. Pulsed laser deposition of vo2 thin films. *Applied physics letters*, 65(25):3188–3190, 1994.

[135] CV Ramana, RJ Smith, and OM Hussain. Grain size effects on the optical characteristics of pulsed-laser deposited vanadium oxide thin films. *Physica status solidi (a)*, 199(1):R4–R6, 2003.

[136] CV Ramana, RJ Smith, OM Hussain, and CM Julien. On the growth mechanism of pulsed-laser deposited vanadium oxide thin films. *Materials Science and Engineering: B*, 111(2-3):218–225, 2004.

[137] RT Rajendra Kumar, B Karunagaran, D Mangalaraj, Sa K Narayandass, P Manoravi, M Joseph, and Vishnu Gopal. Pulsed laser deposited vanadium oxide thin films for uncooled infrared detectors. *Sensors and Actuators A: Physical*, 107(1):62–67, 2003.

[138] Syed A Bukhari, Sooraj Kumar, Pawan Kumar, Sarang P Gumfekar, Hyun-Joong Chung, Thomas Thundat, and Ankur Goswami. The effect of oxygen flow rate on metal–insulator transition (mit) characteristics of vanadium dioxide (vo2) thin films by pulsed laser deposition (pld). *Applied Surface Science*, 529:146995, 2020.

[139] Beibei Guo, Dongyun Wan, Ahmad Ishaq, Hongjie Luo, and Yanfeng Gao. Direct synthesis of high-performance thermal sensitive vo2 (b) thin film by chemical vapor deposition for using in uncooled infrared detectors. *Journal of Alloys and Compounds*, 715:129–136, 2017.

[140] T Maruyama and Y Ikuta. Vanadium dioxide thin films prepared by chemical vapour deposition from vanadium (iii) acetylacetonate. *Journal of materials science*, 28:5073–5078, 1993.

[141] Kai Liu, Sangwook Lee, Shan Yang, Olivier Delaire, and Junqiao Wu. Recent progresses on physics and applications of vanadium dioxide. *Materials Today*, 21(8):875–896, 2018.

[142] Fabien Béteille, Léo Mazerolles, and Jacques Livage. Microstructure and metal-insulating transition of vo2 thin films. *Materials Research Bulletin*, 34(14-15):2177–2184, 1999.

[143] D Brassard, S Fourmaux, M Jean-Jacques, JC Kieffer, and MA El Khakani. Grain size effect on the semiconductor-metal phase transition characteristics of magnetron-sputtered vo 2 thin films. *Applied Physics Letters*, 87(5):051910, 2005.

[144] Jingzhong Cui, Daoan Da, and Wanshun Jiang. Structure characterization of vanadium oxide thin films prepared by magnetron sputtering methods. *Applied Surface Science*, 133(3):225–229, 1998.

[145] Kuang-Yue Tsai, Tsung-Shune Chin, and Han-Ping D Shieh. Properties of vo2 films sputter-deposited from v2o5 target. *Japanese journal of applied physics*, 42(7R):4480, 2003.

[146] Deyi Fu, Kai Liu, Tao Tao, Kelvin Lo, Chun Cheng, Bin Liu, Rong Zhang, Hans A Bechtel, and Junqiao Wu. Comprehensive study of the metal-insulator transition in pulsed laser deposited epitaxial vo2 thin films. *Journal of Applied Physics*, 113(4):043707, 2013.

[147] Ryan McGee, Ankur Goswami, Behnam Khorshidi, Kristi McGuire, Kalvin Schofield, and Thomas Thundat. Effect of process parameters on phase stability and metal-insulator transition of vanadium dioxide (vo2) thin films by pulsed laser deposition. *Acta Materialia*, 137:12–21, 2017.

[148] YX Guo, YF Liu, CW Zou, ZM Qi, YY Wang, YQ Xu, XL Wang, F Zhang, and R Zhou. Oxygen pressure induced structure, morphology and phase-transition for vo 2/c-sapphire films by pld. *Applied Physics A*, 115:1245–1250, 2014.

[149] Wei Li, Urcan Guler, Nathaniel Kinsey, Gururaj V Naik, Alexandra Boltasseva, Jianguo Guan, Vladimir M Shalaev, and Alexander V Kildishev. Refractory plasmonics with titanium nitride: broadband metamaterial absorber. *Advanced Materials*, 26(47):7959–7965, 2014.

[150] Harsha Reddy, Urcan Guler, Alexander V Kildishev, Alexandra Boltasseva, and Vladimir M Shalaev. Temperature-dependent optical properties of gold thin films. *Optical Materials Express*, 6(9):2776–2802, 2016.

[151] Ying Huang, Dongping Zhang, Yi Liu, Jingcheng Jin, Yu Yang, Tao Chen, Huan Guan, Ping Fan, and Weizhong Lv. Phase transition analysis of thermochromic vo2 thin films by temperature-dependent raman scattering and ellipsometry. *Applied Surface Science*, 456:545–551, 2018.

[152] Liu Hongwei, Lu Junpeng, Zheng Minrui, Tang Sing Hai, Sow Chorng Haur, Zhang Xinhai, and Ke Lin. Size effects on metal-insulator phase transition in individual vanadium dioxide nanowires. *Optics express*, 22(25):30748–30755, 2014.

[153] Bin Hu, Yan Zhang, Wen Chen, Chen Xu, and Zhong Lin Wang. Self-heating and external strain coupling induced phase transition of vo2 nanobeam as single domain switch. *Advanced Materials*, 23(31):3536–3541, 2011.

[154] Hyunwoo Kang, Minhwan Ko, Hyobin Choi, Wanggon Lee, Ranveer Singh, Mohit Kumar, and Hyungtak Seo. Surface hydrogeneration of vanadium dioxide nanobeam to manipulate insulator-to-metal transition using hydrogen plasma. *Journal of Asian Ceramic Societies*, 9(3):1310–1319, 2021.

[155] Shamashis Sengupta, Kevin Wang, Kai Liu, Ajay K Bhat, Sajal Dhara, Junqiao Wu, and Mandar M Deshmukh. Field-effect modulation of conductance in vo2 nanobeam transistors with hfo2 as the gate dielectric. *Applied Physics Letters*, 99(6):062114, 2011.